Brownian motion of partially wetted colloidal particles

Giuseppe Boniello

To cite this version:

Giuseppe Boniello. Brownian motion of partially wetted colloidal particles. Soft Condensed Matter [cond-mat.soft]. Université Montpellier II, 2015. English. NNT : . tel-01267698v1

HAL Id: tel-01267698

https://theses.hal.science/tel-01267698v1

Submitted on 4 Feb 2016 (v1), last revised 11 Oct 2017 (v2)

Collège Doctoral
du Languedoc-Roussillon

THÈSE

Pour obtenir le grade de
Docteur

Délivré par l'**Université Montpellier II**

Préparée au sein de l'école doctorale **I2S***
Et de l'unité de recherche **L2C - UMR 5221**

Spécialité: **Physique**

Présentée par **Giuseppe Boniello**
`giuseppe.boniello@univ-montp2.fr`

Mouvement brownien des particules colloïdales partiellement mouillées

Soutenue le 06/02/2015 devant le jury composé de :

Thomas Fischer	Professeur	Univ. Bayreuth	Rapporteur
Pawel Pieranski	DdR	CNRS Orsay	Rapporteur
Frédéric Restagno	CdR	CNRS Orsay	Examinateur
Luca Cipelletti	Professeur	Univ. Montpellier II	Président du jury
Maurizio Nobili	Professeur	Univ. Montpellier II	Directeur de thèse
Michel Gross	DdR	CNRS Montpellier	Co-directeur de thèse

UNIVERSITÉ MONTPELLIER 2
SCIENCES ET TECHNIQUES

* **I2S :** École doctorale Information Structures Systèmes

La professione del ricercatore deve tornare alla sua tradizione di ricerca per l'amore di scoprire nuove verità. Poiché in tutte le direzioni siamo circondati dall'ignoto e la vocazione dell'uomo di scienza è di spostare in avanti le frontiere della nostra conoscenza in tutte le direzioni, non solo in quelle che promettono più immediati compensi o applausi.

The work of the researcher has to come back to its tradition of research for the love of discovering new truths. Since we are surrounded by the unknown in all the directions, the vocation of the scientist is to advance the frontiers of our knowledge in all the directions, not only in those that promise more immediate rewards or approvals.

Enrico Fermi

Acknowledgement

In summer 2011, when someone asked me about my future plans, I was sure only of two things: I would not go abroad, and I would not start a PhD. Now, after three years spent in France, I'm going to defend my thesis. I can state that a lot of things changed during these last three years.

It was a great experience, in my work and in my life. For sure, not everything was perfect. Sometimes I felt lost, or something didn't go as I hoped. But good moments overcame bad ones and, if now I'm crossing the finish line, a big contribution came from people around me.

For the scientific and professional side, I had the fortune to have a strong and competent group behind me. They followed my works, gave me valuable suggestions and helped me to improve my scientific background. First of all, I thank Maurizio, who offered me the opportunity to come here in Montpellier and who directed my thesis. I thank also Michel, Christophe, Antonio and Martin for their useful contributions in several fields all along these last three years. In the same way, I want to express my gratitude to all the Soft Matter team at L2C, where I found a stimulating environment for my researches.

But there is also a personal side, as important as the previous one, without which I couldn't be able to fully carry on my work. I thank Elisa and Nathalie, whom first welcomed me in Montpellier when I just arrived. Thanks to the big (too big), and still growing, Italian community in the Soft Matter Lab: Domenico, Luca, Stefano, Dario and Dafne, in rigorous order of appearance in the lab. With them, I shared hundreds of pizzas, floods of coffee and silly chats. But, most important, they were a constant presence and they made me feel home. A special acknowledgment for Rym, who was also an excellent officemate and made our room much more joyful. Thanks also to all the people with whom I enjoyed my lab–life (and also, in some cases, lunch, evenings or spare time): Clara, Adrian, Srishti, Laure, Cyrille, Pugnitopo, Yassine, Valentin, Mohsen, Guilhem, JeanCharlie, Xiaolu and Octavio.

Thanks to my dearest friends Stefano and Edoardo: I could not share my spare time with them or meet them as before, but they are still a helpful reference for me.

Finally, this work was possible also because of the moral support from my family: my father Gerardo, my mother Luisa and my sister Cristina. Not only they always encourage me, but they were also able to be close to me even at 700 km of distance.

Even if you cannot see it and I will never admit elsewhere, all these people are present in each word and in each idea of the present manuscript.

Résumé

La dynamique de particules colloïdales à l'interface entre deux fluides joue un rôle central dans la micro-rhéologie, l'encapsulation, l'émulsification, la formation de biofilms et la décontamination de l'eau. En outre, ce sujet est également stimulant d'un point de vue théorique en raison de la complexité de l'hydrodynamique à l'interface et du rôle de la ligne de contact. Malgré ce grand intérêt, le comportement d'une particule à une interface fluide n'a jamais été caractérisé directement. Dans cette thèse, nous étudions le mouvement brownien de billes micrométriques de silice et de sphéroïdes de polystyrène à une interface eau–air. Nous contrôlons expérimentalement tous les paramètres d'intérêt. L'angle de contact des billes est finement ajusté dans la gamme $30° - 140°$ par des traitements chimiques de surface et mesuré in situ par interférométrie. Le rapport d'aspect de particules sphéroïdales varie dans la gamme 1 - 10 par étirage de billes sphériques commerciales. Les dynamiques de translation et de rotation sont suivies par particle tracking. Contre intuitivement et contre tous les modèles hydrodynamiques la diffusion est beaucoup plus lente que prèvu. Pour expliquer cette dissipation supplémentaire nous concevons un modèle tenant compte de la contribution des fluctuations thermiques de l'interface à la ligne de contact. Les fluctuations donnent origine à des forces aléatoires qui s'ajoutent à celles dues aux chocs de molécules. Le théorème de fluctuation–dissipation permet d'obtenir la friction supplémentaire associée à ces forces flottantes. La friction totale est discutée en termes d'hétérogénéités de la surface des particules et d'ondes capillaires à l'interface.

Mots clês: colloïdes, mouvement brownien, interface

Abstract

The dynamics of colloidal particles at the interface between two fluids plays a central role in micro-rheology, encapsulation, emulsification, biofilms formation and water remediation. Moreover, this subject is also challenging from a theoretical point of view because of the complexity of hydrodynamics at the interface and of the role of the contact line. Despite this great interest, the behavior of a single particle at a fluid interface was never directly characterized. In this thesis, we study the Brownian motion of micrometric spherical silica beads and anisotropic polystyrene spheroids at a flat air-water interface. We fully characterize and control all the experimentally relevant parameters. The bead contact angle is finely tuned in the range 30-140 by surface treatments and measured in situ by a home-made Vertical Scanning Interferometer. The spheroid aspect ratio varies in the range 1 10 by stretching of commercial beads. The translational and the rotational dynamics are followed by particle tracking. Counter-intuitively, and against all hydrodynamic models, the diffusion is much slower than expected. To explain this extra dissipation we devised a model considering the contribution of thermally activated fluctuations of the interface at the triple line. Such fluctuations couple with the lateral movement of the particle via random forces that add to the ones due to the shocks of surroundings molecules. Fluctuation-dissipation theorem allows obtaining the extra friction associated to this additional mechanism. The fitting values of the total friction are discussed in term of the typical scales of particle surface heterogeneities and of surface capillary waves.

Key words: colloid, Brownian motion, interface

Contents

Facesti come quei che va di notte,
che porta il lume dietro e sé non
giova, ma dopo sé fa le persone
dotte.

*Thou didst as he who walketh in
the night, who bears his light
behind, which helps him not, but
wary makes the persons after him.*

Dante Alighieri, Purgatorio XXII

Introduction

Looking at micrometric particles suspended in a fluid phase, a random and irregular motion is observed. This observation was firstly made in 1827, and the behavior was named Brownian motion after by the Scottish botanist Robert Brown that investigated it. The mechanism was understood by Einstein and explained in one of the four *Annus Mirabilis papers* in 1905 [1], where the thermal origin of the dynamics was pointed out. Its experimental confirmation took a long time and it is still in progress. In 1909 Perrin [2] provided the very first particle tracking experience to find the diffusion coefficient of spherical bead immersed in a fluid. One century after, such a measurement was extended to more natural anisotropic morphologies, as spheroidal particles. Such dynamics was quantified by digital video microscopy for spheroids in water confined in a two–dimensional geometry [3, 4] and by using holography and confocal microscopy in the volume [5]. A crucial characteristic predicted by Einstein as the very short time transition between the ballistic and the diffusive motion was recently investigated using optical tweezers in both air [6] and liquid [7]. The effect at small length scales, where Einstein relations are not totally fulfilled, was also explored in the past few years and the Brownian diffusion was studied in the case of nanoparticles [8, 9, 10, 11].

All these recent works show that Brownian motion is still a topical subject in soft matter and still a fruitful playground for new researches. One of such particularly important fields is the dynamics of particles at fluid interfaces. On one hand, from a practical point of view, it governs the behavior of kinetically arrested colloidal gels [12], the formation of bacteria based biofilm [13], and the cellular signaling via membrane proteins [14]. On the other hand, it is also challenging from a more fundamental point of view, as it allows to probe different interfacial hydrodynamics phenomena, as surface viscosity and eventually visco–elasticity, and the role of the contact line, where the three phases meet together [15].

The work performed during this PhD thesis could be seen as a first step to fill the gap in this direction. For spherical colloids, we propose a model for the friction acting at the interface taking into account the effect of thermal fluctuations at the contact line. Our model is able to capture the unexpected slowed–down diffusion of a particle at an air–water interface. The same theoretical approach is followed also for anisotropic spheroidal particles, where the presence of an additional drag is experimentally much more evident: our measurements show a rotational diffusion coefficient at the interface one order of magnitude slower than in the bulk, and a translational diffusion coefficients two times smaller, for the most elongated particle. Geometrical considerations about the distribution of thermal fluctuating torques and forces along an elliptic contact line are able to catch such a dynamics.

Plan of the thesis

The thesis starts with a theoretical overview on the main treated topics (**chapter 1**). Basic notions about fluid dynamics, interfacial properties and wetting phenomena are presented in order to define the background from which the present work has been developed. Moreover, the state of arts in the field is reported.

Chapter 2 is focused on the measurements of the diffusion of micrometric spherical particles at an air–water interface. The particle immersion depth in water is tuned by chemical treatments of the bead surface, and measured by gel trapping and interferometric techniques. The dynamics is followed by particle tracking and the corresponding translational diffusion coefficients are measured.

In a similar way, in **chapter 3** the Brownian motion of partially immersed spheroidal colloids is considered, as a function of their aspect ratio. The particles are prepared by stretching of commercial polystyrene beads in a homemade apparatus. Deformations of the interface induced by the particle are observed by interferometry. Particle tracking allows to recover both translational and rotational dynamics.

In both cases, a counter-intuitively, slow diffusion is observed and existing hydrodynamics theories are not able to catch this behavior.

The hydrodynamics features associated to the presence of a particle at the interface are taken into account as attempts to describe the slowed–down dynamics. All of them fail since the corresponding dissipations are too small than the ones measured. A new paradigm is so required, and a new model is conceived in **chapter 4** for the case of spherical particles. In the model, the contribution of thermal fluctuations of the interface translates in random forces that affect the dynamics. Fluctuation–dissipation theorem allows to obtain the friction associated to these additional random forces, as at thermal equilibrium the particle kinetic energy remains fixed by the equipartition theorem. The obtained friction is discussed in two regimes, for a moving or a pinned contact line. In any cases, fluctuations of the interface at the nanometric scales are able to catch the measured dynamics and provide an additional drag in the right order of magnitude.

In **chapter 5** the solution obtained for spheres is generalized for the more complex morphology of spheroidal particles. Assuming the same physical origin of the additional drag, we are able to fit both translational and rotational dynamics of the particle, leading again to the reasonable nanometric range for the fluctuations. Such results point out the central role played by thermally activated fluctuations at the contact line on the Brownian dynamics of micrometric particles at a fluid interface.

Quelli che s'innamoran di pratica sanza scienzia son come 'l nocchier ch'entra in navilio senza timone o bussola, che mai ha certezza dove si vada.

Those who fall in love with practice without knowledge are like the coxswain that sails without rudder or compass, and never has for sure where hes going.

Leonardo Da Vinci

Chapter 1

State of art and theoretical background

Introduction

An overview of the state of art in Brownian dynamics and of the theoretical background is here proposed as a starting point of this thesis.

First of all, the definition of Brownian motion and the mathematical derivation of the diffusion coefficient D are presented (par. 1.1). Such a coefficient is already known from Stokes–Einstein relation, and experimentally verified, for beads fully immersed in a fluid (par. 1.2). In the case of spherical particles straddled at an interface between two fluids their position, in terms of immersion depth and contact angle, are discussed in par. 1.3. Then, the particle lateral dynamics is analyzed considering the viscous drag at the interface, as computed by numerical predictions and measured in few experiments in literature (par. 1.4). In same way, anisotropic spheroidal particles are considered. We show their diffusion in the volume, from both a theoretical and an experimental point of view (par. 1.5). Finally, the basic features concerning spheroids at the interface, as the interface deformation and the coupling with interface curvature, are addressed (par. 1.6).

1.1 Definition of Brownian motion

A colloidal particle immersed in a fluid phase shows an irregular and random walk, due to the collision between the molecules of the surrounding fluid and the particle itself. Such an effect is known as Brownian motion, named after the Scottish botanist Robert Brown that firstly observed the erratic movement of pollen grains in water. Each molecular collision provides a random kick that boosts particle motion and that can be quantified by a random force $F_r(t)$. At the same time, a viscous force F_v which opposes to the particle motion, is acting on the particle:

$$F_v = -\zeta v \tag{1.1}$$

where v is the velocity of the particle and ζ is the friction coefficient.
The equations of motion of the Brownian particle, known as Langevin equations, describe the evolution in time of the particle position $x(t)$:

$$\begin{aligned} \frac{dx(t)}{dt} &= \dot{x}(t) = v(t) \\ m\frac{dv(t)}{dt} &= F_r(t) - \zeta v(t) \end{aligned} \tag{1.2}$$

An exact solution cannot be found, since the random force lacks of an analytical expression. However, an alternative approach can be followed. Let multiply both sides of eq. 1.2 by x, and consider the ensemble average of all the terms:

$$m\Big\langle x\frac{d\dot{x}}{dt}\Big\rangle = \langle xF_r\rangle - \zeta\langle x\dot{x}\rangle \tag{1.3}$$

The first term in the right hand side is always null, since F_r is defined as a random force. The term in the left hand side is instead developed as

$$x\frac{d\dot{x}}{dt} = \frac{d}{dt}(x\dot{x}) - \dot{x}^2 \tag{1.4}$$

Taking into account the equipartition theorem, i.e. $k_BT \sim \langle m\dot{x}^2\rangle$, eq. 1.3 becomes

$$m\frac{d}{dt}\langle x\dot{x}\rangle = k_BT - \zeta\langle x\dot{x}\rangle \tag{1.5}$$

and it can be solved with respect to the variable $\langle x\dot{x}\rangle$:

$$\langle x\dot{x}\rangle = Ce^{-t/\tau_p} + \frac{k_BT}{\zeta} \tag{1.6}$$

with $\tau_p = m/\zeta$ and C an arbitrary constant of integration. C is recovered imposing the initial condition $x = 0$ at $t = 0$: $C = -k_BT/\zeta$. Note also:

$$\langle x\dot{x}\rangle = \frac{1}{2}\frac{d}{dt}\langle x^2\rangle$$

After integration of eq. 1.6:

$$\langle x^2\rangle = \frac{2k_BT}{\zeta}\left[t - \tau_p\left(1 - e^{-t/\tau_p}\right)\right] \tag{1.7}$$

At short times, i.e. at $t \ll \tau_p$, the exponential function in eq. 1.7 is safely approached by its development in the Taylor series:

$$e^{-t/\tau_p} = 1 - \frac{t}{\tau_p} + \frac{1}{2}\frac{t^2}{\tau_p^2} \tag{1.8}$$

and eq. 1.7 is written:

$$\langle x^2 \rangle = \frac{k_B T}{m} t^2 \tag{1.9}$$

Thus, for short time scales with respect to τ_p, the particle shows a ballistic motion at constant velocity $v = \sqrt{k_B T/m}$, as expected from equipartition theorem. A direct verification of such a prediction has been recently provided by a measurement of the instantaneous velocity of silica beads trapped in optical tweezers (fig. 1.1) [6].

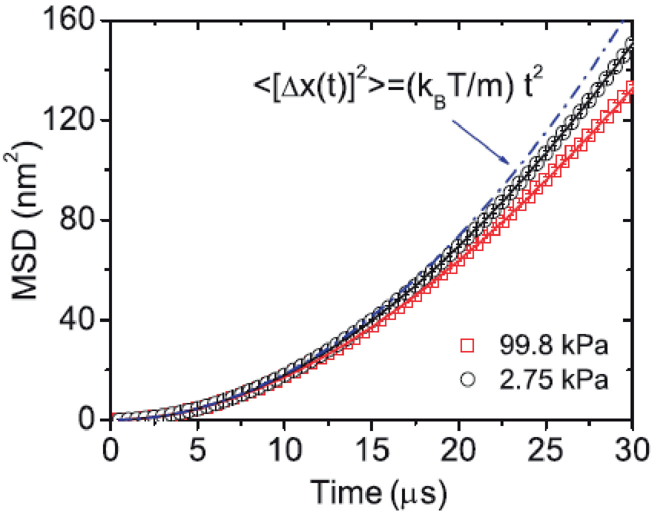

Figure 1.1: Mean Square Displacements (MSDs) of 3 μm silica beads, at short time scales ($t \ll \tau_p$). The particles are trapped in air at different pressures (99.8 kPa for red squares and 2.75 kPa for black circles). The motion is not dependent on the external pressure and shows, in both cases, a quadratic behavior (dash-dotted line) typical of a ballistic motion, as expected from the theory. The fit is in agreement with the predictions and leads to the thermal velocity $v = \sqrt{k_B T/m}$. Measurements and graph from Li et al., Science 328, 1673 (2010) [6].

In the opposite case, $t \gg \tau_p$, $e^{-t/\tau_p} \rightarrow 0$ and

$$\langle x^2 \rangle = 2\frac{k_B T}{\zeta} t = 2Dt \tag{1.10}$$

Here, the effect of several random molecular collisions translates in a diffusive regime, where the Mean Square Displacement (MSD) $\langle x^2 \rangle$ linearly increases in time. In eq. 1.10 D is the diffusion coefficient

$$D = \frac{k_B T}{\zeta} \tag{1.11}$$

The friction coefficient ζ is considered in the following paragraphs for different systems (spheres and spheroids, immersed in a fluid and trapped at the interface between two fluids) in order to predict the diffusive dynamics.

1.2 Spherical particles fully immersed in a fluid

1.2.1 Friction coefficient: the Stokes-Einstein equation

We consider the prediction of the diffusion coefficient of a spherical bead totally immersed in a fluid phase. For this purpose, we need to write the friction coefficient ζ, provided in this case by Stokes–Einstein equation. The complete derivation reported here follows the discussion of Landau and Lifshitz [16].
We start from the Navier–Stokes equation, written for incompressible fluids and at low Reynolds number ($\rho v l/\eta \ll 1$, where ρ is the density and η the viscosity of the fluid, $\mathbf{v}$ the velocity of flow and l a typical length scale):

$$\eta \nabla^2 \mathbf{v} - \mathbf{grad} p = 0 \tag{1.12}$$

The equation can be expressed using the operator

$$E^2 = \frac{\partial^2}{\partial r^2} + \frac{\sin\vartheta}{r^2}\frac{\partial}{\partial\vartheta}\left(\frac{1}{\sin^2\vartheta}\frac{\partial}{\partial\vartheta}\right) \tag{1.13}$$

and in terms of the Stokes stream function ψ; in polar coordinates (r, ϑ) (fig. 1.2), it is related to the flow velocity components in the following way:

$$v_r = \frac{1}{r^2 \sin\vartheta}\frac{\partial\psi}{\partial\vartheta} \qquad v_\vartheta = -\frac{1}{r\sin\vartheta}\frac{\partial\psi}{\partial r}. \tag{1.14}$$

Hence, eliminating the pressure between these two components, eq. 1.12 becomes

$$E^2\left(E^2\psi\right) = 0 \tag{1.15}$$

We impose the no-slip condition, i.e. null radial and angular velocities, at the sphere surface ($r = R$, with R radius of the sphere):

$$v_r = 0 \qquad v_\vartheta = 0 \tag{1.16}$$

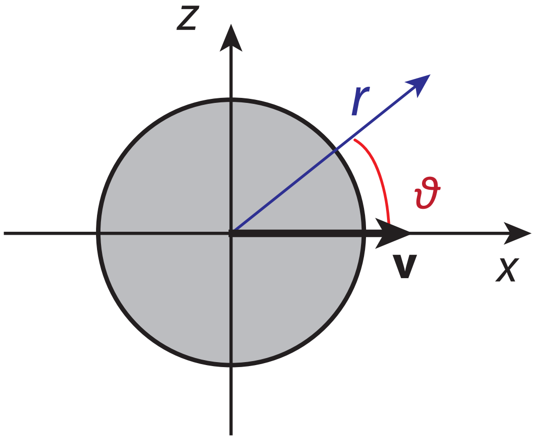

Figure 1.2: Polar coordinates system (r, ϑ), used in the solution of Stokes–Einstein equation. The particle is assumed moving at constant velocity $\mathbf{v}$ along the x–axis.

and a velocity v of the flow at great distance from the particle ($r \to \infty$); for the function ψ, this condition translates in

$$\psi \to \frac{v}{2} r^2 \sin^2 \vartheta \tag{1.17}$$

A solution in the form $\psi = f(r) \sin^2 \vartheta$ is so expected and, taking into account the boundary conditions shown above, a suitable solution for ψ is

$$\psi(r, \vartheta) = \left(\frac{vr^2}{2} - \frac{3vRr}{4} + \frac{vR^3}{4r} \right) \sin^2 \vartheta \tag{1.18}$$

From the definition of ψ (eq. 1.14), the velocity components are recovered

$$\begin{aligned} v_r &= v \left(1 - \frac{3R}{2r} + \frac{R^3}{2r^3} \right) \cos \vartheta \\ v_\vartheta &= -v \left(1 - \frac{3R}{4r} + \frac{R^3}{4r^3} \right) \sin \vartheta \end{aligned} \tag{1.19}$$

Since the shear strain rate $\gamma_{r\vartheta}$ is defined by

$$\gamma_{r\vartheta} = r \frac{\partial}{\partial r} \left(\frac{v_\vartheta}{r} \right) + \frac{1}{r} \frac{\partial v_r}{\partial \vartheta} \tag{1.20}$$

the shear stress on the surface ($r = R$) is

$$\tau_{r\vartheta} = \eta \gamma_{r\vartheta}(r = R) = -\eta \frac{3v}{2R} \sin \vartheta \tag{1.21}$$

To determine the pressure p on the particle, we use eq. 1.12; its solution leads to

$$p = p_0 - \eta \frac{3v}{2R} \cos\vartheta \tag{1.22}$$

where p_0 is the fluid pressure at infinity.

The friction drag F exerted by the fluid on the particle is thus given by

$$F = \oint (-p\cos\vartheta - \tau_{r\vartheta}\sin\vartheta)dS = 6\pi\eta R v \tag{1.23}$$

where both the pressure and the tangential stress, projected on the direction of the motion, are integrated over the whole spherical surface.

The drag coefficient for a sphere moving in fluid phase, defined by the ratio $\zeta = F/v$, is finally expressed as:

$$\zeta = 6\pi\eta R \tag{1.24}$$

Replacing ζ in eq. 1.11, a theoretical prediction of the diffusion coefficient, in the case of a spherical bead totally immersed in volume, is provided by

$$D_{sphere} = \frac{k_B T}{6\pi\eta R} \tag{1.25}$$

The same approach is followed to compute the rotational friction coefficient ζ_φ. We consider a sphere that slowly rotates with a constant angular velocity ω around an axis z.

In spherical coordinates system (fig. 1.3), the velocity $\mathbf{v}$ is in the form

$$\mathbf{v} = [v_r, v_\varphi, v_\vartheta] = [0, v_\varphi(r,\vartheta), 0] \tag{1.26}$$

and all the quantities are symmetric about the z–axis, i.e. there is no dependence on φ.

The Navier-Stokes equation (eq. 1.12) is thus reduced to

$$0 = \nabla^2 v_\varphi = \frac{1}{r^2}\frac{\partial}{\partial r}\left(r^2 \frac{\partial}{\partial r} v_\varphi\right) + \frac{1}{r^2}\frac{\partial}{\partial\vartheta}\left(\frac{1}{\sin\vartheta}\frac{\partial}{\partial\vartheta} v_\varphi \sin\vartheta\right) \tag{1.27}$$

Imposing the boundary conditions

$$\begin{gathered} v_\varphi = \omega R \sin\vartheta \qquad r = R \\ v_\varphi \to 0 \qquad r \to +\infty \end{gathered} \tag{1.28}$$

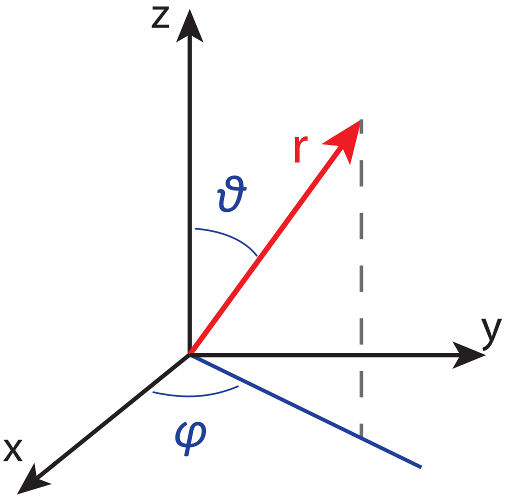

Figure 1.3: Spherical coordinates system (r, φ, ϑ), used in the computation of the rotational friction coefficient. The particle is assumed rotating around the axis z.

the solution for the velocity field is achieved

$$v_\varphi = \omega R \left(\frac{R}{r}\right)^2 \sin\vartheta \tag{1.29}$$

The shear stress

$$\tau_{r\varphi} = \eta r \frac{\partial}{\partial r}\left(\frac{v_\varphi}{r}\right) \tag{1.30}$$

is integrated on the particle surface $(r = R)$ and leads to the friction drag torque Γ:

$$\Gamma = \oint \tau_{r\varphi} R \sin\vartheta dS = 8\pi\eta R^3 \omega \tag{1.31}$$

The corresponding rotational friction coefficient is $\zeta_\varphi = \Gamma/\omega$, thus

$$\zeta_\varphi = \frac{\Gamma}{\omega} = 8\pi\eta R^3 \tag{1.32}$$

providing the corresponding theoretical prediction of the rotational diffusion coefficient of a spherical bead totally immersed in volume:

$$D_{\varphi,sphere} = \frac{k_B T}{8\pi\eta R^3} \tag{1.33}$$

1.2.2 Experimental measurements of diffusion in bulk

The first experimental observation of Brownian dynamics was done by Jean Perrin in 1909 [2]. In his experiment, microscopic latex particles were immersed in water at constant temperature. Using an optical microscope in a *camera lucida* set-up, a 2-D projection of particle trajectories on a paper sheet was obtained. The particle position was marked every 30 seconds for 24 minutes. An example of this first particle tracking is reported in fig. 1.4.

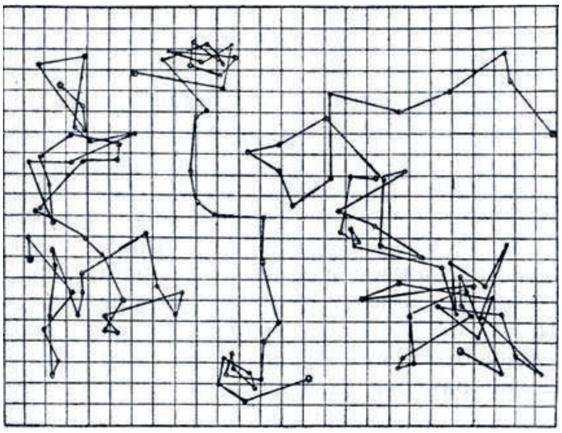

Figure 1.4: Hand-drawn particle trajectories obtained by J. Perrin. The sample was observed by optical microscopy, and the image was projected on a paper sheet. The position was marked with a time interval $\Delta t = 30$s.

From such trajectories, the mean square displacement in 2-D is computed as a function of the time lag. The resulting diffusion coefficient was found in agreement with Stokes-Einstein relation.

1.3 Spherical particles at a fluid interface: contact angles

1.3.1 Equilibrium position for ideal surfaces: Young's contact angle

The equilibrium position of a particle straddled at a fluid interface is firstly recovered in the ideal case of a flat and homogeneous particle surface, where the interface can slide on the particle without any constriction. The pinning of the contact line or the solid friction on the substrate are not considered here. We take into account all the contributions to the surface free energy and look for the configuration that minimizes it [17]. In fact, when a solid particle is at the air-water interface, three surfaces have to be considered (fig. 1.5):

1. the lower spherical cap, corresponding to the wetted part of the colloid (S_1);
2. the upper spherical cap, where the solid is in contact with the air (S_2);
3. the missing air-water interface, due to the presence of the bead (S_3).

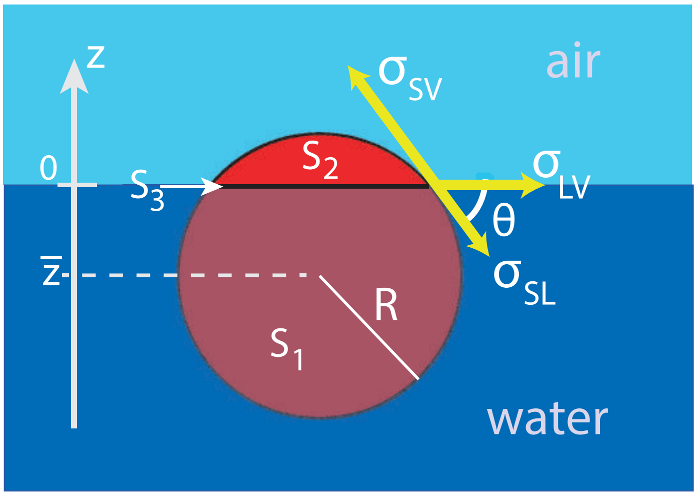

Figure 1.5: Spherical bead with radius R at the air-water interface. Three different surface are considered in the system: solid-water (S_1), solid-air (S_2), missing air-water (S_3) surfaces. Each one contributes to the total free surface energy, according to the corresponding surface tensions. The position of the center of the particle is defined with respect to the vertical axis z. $z = 0$ corresponds to the water level; the equilibrium position of the center of the particle is denoted with $\bar{z}$. In a similar approach, the equilibrium of the three interfacial forces at the contact line leads to the definition of the contact angle θ.

Let us denote with z the vertical position of the center of the particle with respect to the water level; R is the radius of the particle. The three surfaces, and the corresponding energy contributions, are recovered from simple geometric arguments:

1. $E_{SL} = \sigma_{SL} 2\pi R^2 \left(1 - z/R\right)$
2. $E_{SV} = \sigma_{SV} 2\pi R^2 \left(1 + z/R\right)$
3. $E_{LV} = -\sigma_{LV} \pi R^2 \left(1 - z^2/R^2\right)$

where σ denotes the surface tensions of the solid-liquid (SL), solid-vapor (SV) and liquid-vapor (LV) interfaces.

The total surface free energy is thus:

$$E = E_{SL} + E_{SV} + E_{LV}$$

$$E = \pi R^2 \sigma_{LV} \left[\frac{z^2}{R^2} + \frac{z}{R} \left(\frac{\sigma_{SV} - \sigma_{SL}}{\sigma_{LV}} \right) + \frac{2\sigma_{SL} + 2\sigma_{SV} - \sigma_{LV}}{\sigma_{LV}} \right] \tag{1.34}$$

With respect to the normalized vertical position z/R, the total surface free energy E has a parabolic profile; the particle is trapped in a potential well, whose equilibrium position $\bar{z}$ is obtain from the condition $\frac{\partial E}{\partial z} = 0$:

$$\frac{\bar{z}}{R} = -\frac{\sigma_{SV} - \sigma_{SL}}{\sigma_{LV}} \tag{1.35}$$

Since the contact angle θ can be defined, from trigonometry, as (see fig. 1.5)

$$\cos\theta = -\frac{\bar{z}}{R} \tag{1.36}$$

eq. 1.35 is re-written as a function of θ:

$$\sigma_{LV} \cos\theta = \sigma_{SV} - \sigma_{SL} \tag{1.37}$$

Eq. 1.37 represents the Young's law [18] and can be retrieved by considering the equilibrium of the three interfacial forces (per unit length) acting at the contact line, on the surface of the particle (fig. 1.5).

The contact angle is related to the surface tensions of the considered phases:

$$\theta = \arccos \frac{\sigma_{SV} - \sigma_{SL}}{\sigma_{LV}} \tag{1.38}$$

Different experimental techniques, as Gel Trapping and Vertical Scanning Interferometry (see chapter 2 for a detailed explanation of their working principles) are used to recover a direct measurement of θ.

1.3.2 Equilibrium position for heterogeneous surfaces

Young's equation (eq. 1.37) provides an equilibrium contact angle and a corresponding equilibrium immersion depth in the case of an ideal homogeneous surface. Nevertheless, in many practical applications, we have to handle more complex surfaces, as heterogeneous substrates. For these cases, Cassie and Baxter [19] developed a model for the contact angle θ.

Let us consider a spherical bead at the air-water interface, at an equilibrium contact angle θ that is hitherto unknown. The three areas pertinent in the problem can be written as a function of θ:

- $A_{SV} = 2\pi R^2(1-\cos\theta)$
- $A_{SL} = 2\pi R^2(1+\cos\theta)$
- $A_{LV} = \pi R^2(1-\cos^2\theta)$

where the indexes denote the solid-vapor (SV), solid-liquid (SL) and liquid-vapor (LV) interfaces, respectively. Here, we suppose that the solid surface consists of n different materials, uniformly distributed over the substrate. Each material has its own surface tensions $\sigma_{i,SV}$, $\sigma_{i,SL}$ and occupies a given fractional area f_i; such a value is the same at both solid-vapor and solid-liquid interfaces. For the sake of simplicity, we discuss the case $n = 2$. The total surface free energy is written (see eq. 1.34 for comparison):

$$E = 2\pi R^2 \Big[(1-\cos\theta)\left(f_1\sigma_{1,SV} + f_2\sigma_{2,SV}\right) + \\ + (1+\cos\theta)\left(f_1\sigma_{1,SL} + f_2\sigma_{2,SL}\right) - \frac{1}{2}\left(1-\cos^2\theta\right)\sigma_{LV}\Big] \tag{1.39}$$

We recover θ from the minimization of the free surface energy, i.e.

$$\frac{\partial E}{\partial\theta} = 2\pi R^2 \sin\theta\left[f_1\sigma_{1,SV} + f_2\sigma_{2,SV} - f_1\sigma_{1,SL} - f_2\sigma_{2,SL} + \cos\theta\sigma_{LV}\right] = 0 \tag{1.40}$$

that leads to

$$\cos\theta = f_1\frac{\sigma_{1,SV}-\sigma_{1,SL}}{\sigma_{LV}} + f_2\frac{\sigma_{2,SV}-\sigma_{2,SL}}{\sigma_{LV}} = f_1\cos\theta_1 + f_2\cos\theta_2 \tag{1.41}$$

where θ_i is the equilibrium contact angle of the ideal homogeneous surface composed only by the material i. In other words, in Cassie–Baxter model the macroscopic contact angle of an heterogeneous substrate is given by the average of the contact angles of the composing materials, weighted by the fractional area occupied by each one.

1.3.3 Microscopic contact angles

So far, the discussion on the energies involved and on the equilibrium contact angle was in the far field where the relevant parameters are simply the interfacial tensions. Thus, the equilibrium contact angle θ (eqs. 1.37, 1.41) is identical to the angle θ_{ap} that one measures by macroscopic techniques such the sessile drop method (fig. 1.6) or, as done in this thesis, interferometric techniques (par. 2.2.2). However when going down in length scales close to the triple line, local contact angles may differ from the far-field equilibrium contact angle. Two additional regimes have been discussed in the literature [20, 21]. At length scales 1 nm

$< \ell < 1$ μm, colloidal forces such as Van der Waals (VdW) and Electrostatic double layer (EDL) interactions will affect the contact angle profile. VdW includes intermolecular dipole–dipole, dipole–induced dipole, and induced dipole–induced dipole interactions. Electrostatic double layer depends on the surface potential and electrolyte concentration. The Debye screening length sets the length scale of this interaction, which for pure water is about 1μm [22]. A new microscopic angle θ_m, slightly different from θ_{ap} is present. The microscopic angle θ_m is related to the macroscopic angle θ by considering the dissipation at the local scale. At length scales $\ell < 1$ nm , θ_m will be affected by the thermal fluctuations and short range chemical forces. However, in most common cases, such as wetting theories [23], $\theta_m \simeq \theta$.

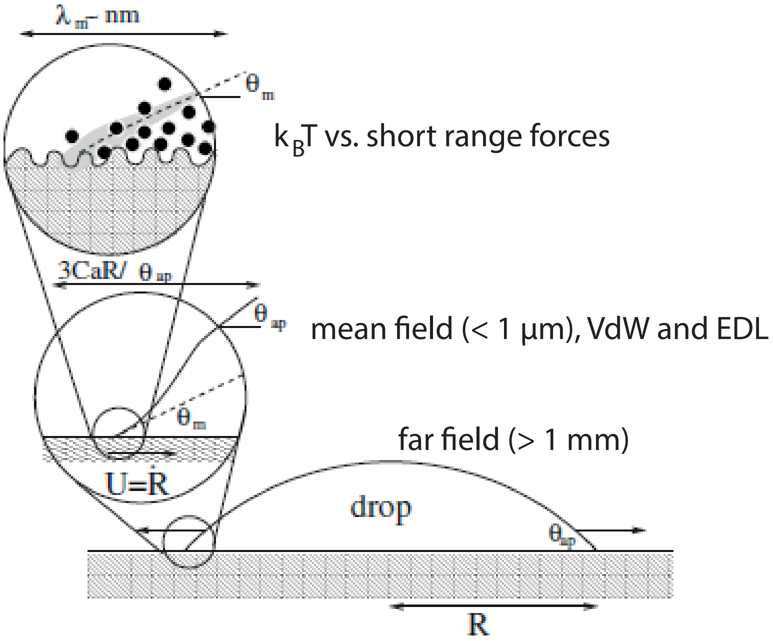

Figure 1.6: Schematic view of the different length scale at the contact line. In the far field the contact angle ($\theta_a p$ in this figure) is the same that one measures with macroscopic techniques, such as sessile drop method. In the mean field, Van der Waals and Electrostatic double layer interactions slightly modify the contact angle profile. At nanometric length scales, the local contact angle θ_m is affected by thermal fluctuations.

1.3.4 Triple line dynamics: advancing and receding contact angles

Let us consider a contact line pinned at a given position on the solid substrate. In the case of a relative motion of the fluid with respect to the particle surface, such a pinning translates in an increase of the contact angle when the fluid advances; similarly, the contact angle decreases when the fluid recedes in the opposite direction (fig. 1.7). Thus, a finite interval of contact angles, around the equilibrium value θ_e provided by Young's law, is allowed [24]:

$$\theta_r < \theta < \theta_a \tag{1.42}$$

where θ_a and θ_r are the advancing and the receding contact angles, respectively. This range is known as contact angle hysteresis.

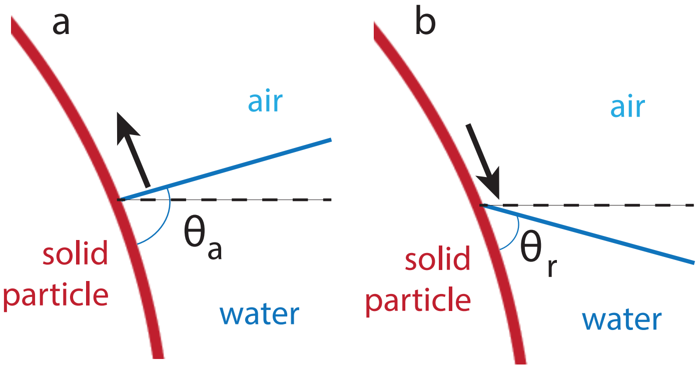

Figure 1.7: Advancing (**a**) and receding (**b**) fluid, with respect to the solid substrate. A pinned contact line induces an increasing (θ_a) or a decreasing (θ_r). The range of allowed contact angle $\theta_r < \theta < \theta_a$ is known as contact angle hysteresis.

Such a hysteresis is induced by surface effects, as roughness or chemical heterogeneities, which produce new local minima in the surface free energy, resulting in metastable equilibrium positions. The energy barriers to reach these minima in the surface free energy are large enough to allow the advancing and receding contact angles [25].

In the case of rough silica surface, the maximum achievable value of contact angle hysteresis is $\Delta\theta = \theta_a - \theta_r \simeq 14°$ [26].

1.3.5 Relaxation to the equilibrium position

Young's law (eq. 1.37) and its modified expression for heterogeneous surfaces (eq. 1.41) provide the equilibrium position of a bead at the interface, but little is known about how this equilibrium is reached. Recently Kaz et al. [15] observed the breaching dynamics of a micrometric particle at a decane–water interface and the successive relaxation toward the equilibrium position (fig. 1.8a). This relaxation shows a logarithmic behavior with characteristic times of months (fig. 1.8b).

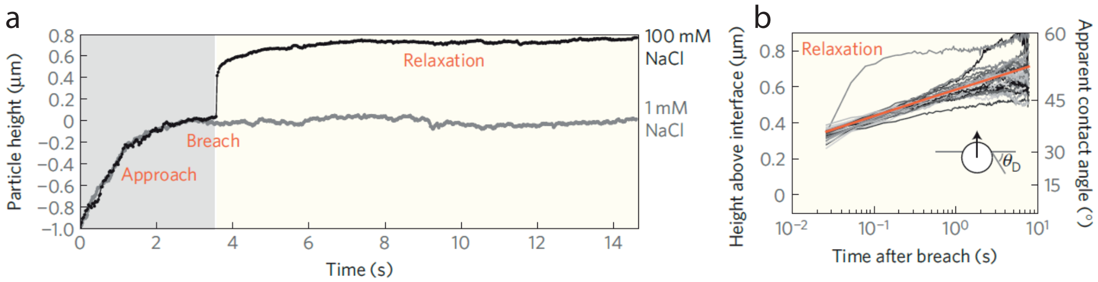

Figure 1.8: **a.** Typical immersion depth of a 1.9μm–diameter bead at an decane–water interface. Three different time phases are visible: approach, breach and relaxation. **b.** Semi–log plot of the position as a function of time, when the particle relaxes to the equilibrium position: the relaxation is approximately logarithmic. Data and graphs from Kaz et al., Nat. Mater. 11, 2 (2012) [15].

This dynamics was explained with a model that takes into account thermally activated jumps of the contact line over surface defects. Each defect is considered as a site where the contact line is pinned with an energy ϵ [23] (see also par. 4.4.1). The velocity of the contact line is expressed by an Arrhenius–like term, and depends on a Boltzmann factor representing the probability to hop the site: $\exp\left(-\epsilon/k_B T\right)$. The rate of hopping is biased by the force acting on the contact line $f = \sigma_{LV}\left(\theta(t) - \theta_e\right)$, where θ_e is the equilibrium contact angle, provided by Young's law, and $\theta(t)$ is the instantaneous contact angle. Such a driving force f is maximum at the breaching and decrease to zero at the equilibrium position, providing a justification to the logarithmic behavior. This experience shows that, in many practical applications, the bead is far from equilibrium and the observed contact angle can significantly differs from the Young's value.

1.4 Lateral motion of spherical particles at a fluid interface

1.4.1 Theoretical models

The viscous drag of spherical beads at a fluid interface has to be computed in order to obtain the interfacial diffusion coefficient. This approach is the same as previously proposed for particles fully immersed in the fluid phase. From a qualitative point of view, the drag ζ_H exerted on the bead must be reduced with respect to one obtained in the volume, due to the lower amount of surrounding water (eq. 1.24). Hydrodynamic theories, developed by Danov et al. [27], Pozrikidis [28] and Fischer et al. [29], provide quantitative expressions for ζ_H (fig. 1.9). All these models agree with the expected behavior described above, i.e. the viscous drag is reduced when the particle is at the interface, and it is decreasing when it is more in air.

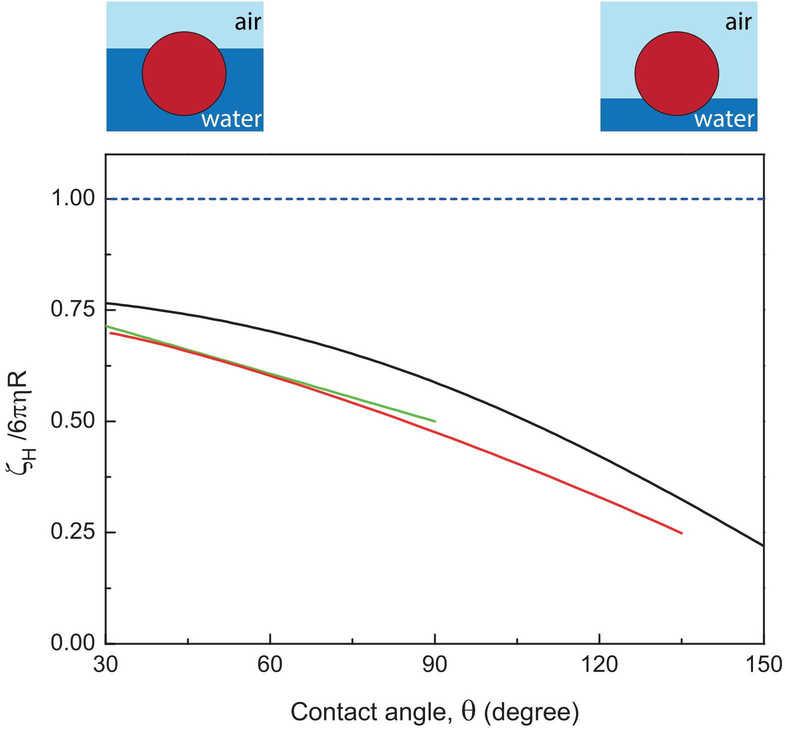

Figure 1.9: Viscous drag ζ_H at the interface, normalized by the friction coefficient in the volume ($\zeta_V = 6\pi\eta R$, dashed line) versus contact angle θ. Higher contact angles correspond to less immersed particle. ζ_H is computed using hydrodynamic theories of Danov et al. [27] (green line), Pozrikidis [28] (red line) and Fischer et al. [29] (black line). The different hypotheses lead to slight differences in the quantitative values, but they all qualitatively decrease, in a similar way, with the contact angle.

In more detail, Pozrikidis [28] took into account the asymmetric deformation of the interface due to the motion of the particle. The drag force was written in the form $F = \beta 6\pi\eta R v$, where β is the dimensionless drag coefficient at the interface. β was numerically computed at 5 values of θ, covering all the range of possible contact angles, in the case $\eta_{air}/\eta_{water} \simeq 0$. In fig. 1.9 (red line), a fit for the surface viscous drag normalized by the bulk value, according to the 5 values in table 1.1, is plotted.

$\theta[°]$	9	45	90	135	171
β	0.72	0.67	0.50	0.25	0.05

Table 1.1: Dimensionless drag coefficient β in the expression of the drag force ($F = \beta 6\pi\eta R v$), as computed by Pozrikidis [28] at 5 values of θ, covering all the range of contact angle.

Danov et al. [27] computed the pressure field and the local velocities at low Reynolds and low capillary numbers ($\eta v/\sigma_{LV} \ll 1$) for a Newtonian viscous interface. The obtained numerical results in the range $30° - 90°$ of θ are reported in fig. 1.9 (green line).
Fischer et al. [29] considered a flat and incompressible interface; an analytical expression for β was obtained from the fit of the numerical solution of the Navier-Stokes equation at the interface (black line in fig. 1.9):

$$\beta = \sqrt{\tanh\left[32\left(1+\cos\theta\right)/\left(9\pi^2\right)\right]} \tag{1.43}$$

Here we report some additional information about the derivation of the model proposed by Fischer et al. [29], that will be used in the following chapters to predict the Brownian dynamics at the interface.

Fischer et al. [29] numerically calculated the drag of a sphere at a flat and incompressible interface. The case of a flat interface leads also to the suppression of the rotation of the sphere, in order to avoid any diverging tangential stress at the contact line. The hypothesis of an incompressible interface is justified since surface compression waves, due to the motion of surface phonons, are faster that the colloidal particle. The complete discussion includes also the role of Marangoni stress, tangential to the surface and generated by gradients in surface surfactant/pollutant density. Since we are here considering a free and clean air-water interface, such a contribution can be reasonably neglected. The flow in the bulk phase is still described by Stokes equation, as in eq. 1.12. In this case, an inverse approach, with respect to the one proposed in par. 1.2.1, has been followed: an external force (per unit volume) **f** is supposed to act on the fluid, and the resulting velocity field **v** is found. Eq. 1.12 is thus slightly modified:

$$\mathbf{f} + \eta(z)\nabla^2\mathbf{v} - \mathbf{grad}p = 0 \tag{1.44}$$

Moreover, the viscosity $\eta(z)$ is now a function of the vertical position, because of the presence of two different fluid:

$$\eta(z) = \eta_{water}\Theta(-z) + \eta_{air}\Theta(z) \tag{1.45}$$

where the symbol $\Theta(z)$ denotes the Heaviside function and the position $z = 0$ correspond to the interface. The boundary conditions include the no-slip at the particle surface and an incompressible two-dimensional Stokes flow at the air-water interface:

$$div\mathbf{v}_s = 0$$

$$v_z(z = 0) = 0$$

$$\mathbf{f}_s - \mathbf{grad}\pi_s + \eta_s \nabla^2 \mathbf{v}_s + \left|\left| \eta \frac{\partial \mathbf{v}}{\partial z} \right|\right|_s = 0 \tag{1.46}$$

$\mathbf{f}_s$ is the component of the external force f, introduced above, tangential to the surface, π_s is the surface pressure and $\mathbf{v}_s$ is the velocity of the fluid at the surface plane. The symbol $||\cdot||_s$ denotes the jump of the considered quantity across the interface.

A solution of eq. 1.44, taking into account boundary conditions in eq. 1.46, can be expressed in the form

$$\mathbf{v}(\mathbf{x}) = \Theta(z \cdot z') \int d^3\mathbf{x}' \mathbf{O}_0(\mathbf{x} - \mathbf{x}') \cdot \mathbf{f}(\mathbf{x}') + \int d^2\mathbf{x}'_s \mathbf{O}_s(\mathbf{x} - \mathbf{x}'_s) \cdot \mathbf{f}_s(\mathbf{x}'_s) \tag{1.47}$$

where $\mathbf{O}_0$ and $\mathbf{O}_s$ are the Oseen tensors in the bulk and at the interface, respectively. Every component of the tensors can be determined, via a mathematical derivation that is not reported here for the sake of simplicity. For our purpose, it is sufficient to point out that the integral in 1.47 can be simplified in the hypothesis $\eta_s = 0$ (in agreement with a free air-water surface) and solved numerically. The results of the viscous drag $\zeta = F/v$, as a function of the contact angle θ, were fitted with an accuracy of 3% by the formula

$$\zeta = 6\pi \sqrt{\tanh\left[32\left(1 + \cos\theta\right) / \left(9\pi^2\right)\right]} \eta R \tag{1.48}$$

1.4.2 Experimental measurements

Petkov et al. [30] determined the drag coefficient of millimetric glass beads (0.4 mm in diameter) at a pure air–water interface, cleaned by suction before the experiment. A lateral capillary force F was applied to the beads by a deformation of the water surface, controlled by a vertical Teflon barrier. The resulting motion of the particle was observed by a vertical long–focus microscope and recorded by a CCD camera. The velocity v was measured, and the relation $F = \beta 6\pi\eta R v$ provided the drag coefficient (β is the dimensionless drag coefficient at the interface). A second, horizontal long–focus microscope was used to measure the size of the particles and their immersion depths in water. At the three considered contact angles ($\theta = 48.7°, 53°, 82°$) the drag coefficient at the interface is lower than the one predicted by Stokes–Einstein relation in volume (table 1.2). The values are compared with the results of the theory by Fischer et al. [29], as the one that predicted the maximum viscous drag.

Radoev et al. [31] considered the case of micrometric spheres at an air–water interface, but without any information about the immersion depth. Polymer beads (melamin, diameter 1 - 1.8 μm) were deposited by a glass fiber on a slightly concave meniscus. The surface was preliminary cleaned since otherwise the particle motion would be practically immobilized. The light of a laser beam, scattered by the particle, was observed by microscopy and allowed to trace the particle trajectory. From the Mean Square Displacement analysis, the diffusion coefficient at the interface was measured $D_S = 0.4\mu\text{m}^2/\text{s}$. The corresponding value in the bulk is not clear: in the considered range of particle size the Stokes–Einstein bulk diffusion is $D_V \sim 0.42 - 0.24\mu\text{m}^2/\text{s}$ (viscosity $\eta \sim 1$ mPa·s and $T = 300$ K). The direct measurements in bulk were instead $D_{V,exp} = 0.6\mu\text{m}^2/\text{s}$. The uncertainty on particle radius and the absence of values for the immersion depth do not allow a quantitative analysis of such results.

Sickert et al. [32, 33] studied the Brownian motion of micrometric polystyrene beads (0.4μm in diameter) in a Langmuir monolayer at different surface viscosities. Such values are compared with the one at a pure air–water interface. The contact angle in clean water was not measured on 0.4 μm beads, but on larger beads made of the same material (diameter 6 - 10 μm) by optically observing their immersion depth at the meniscus of a sessile drop. On those large beads, they found $\theta = 50° \pm 5°$. The motion of 0.4 μm beads was detected by optical microscopy. In order to discard drift effect, the particles were grouped in pairs and their mean square relative separation $\langle \Delta x^2 \rangle$ was measured as a function of time. The averaged diffusion coefficient was measured $D_S = 1.26 \pm 0.19\mu\text{m}^2/\text{s}$, when the diffusion in volume is calculated $D_V = 1.06\mu\text{m}^2/\text{s}$ by Stokes–Einstein relation. The diffusion is faster at the interface than in volume, but not as much as predicted by theoretical models [27, 28, 29] (par. 1.4.1).

Chen and Tong [34] focused on the interface diffusion on multiple particles systems, where the diffusion coefficient is written as a function of the area fraction n occupied by the particles. In order to recover the case of single particle treated in this thesis, we extrapolate the results at $n \to 0$. Three silica bead samples were used (diameter 0.73 μm, 0.97 μm, 1.57 μm). The experimental procedures were the same as described in the previous cases. Great care was taken to clean the particles and the air–water interface, the beads were observed by optical microscopy and the MSD was measured as the function of the time lag. The experimental dimensionless drag coefficients β are reported in table 1.2. A contact angle of $\theta = 64°$ was found comparing the result on the set of beads at diameter 0.97 μm ($\beta = 0.69$) with theoretical prediction [29]. For the other two sets of beads, the obtained values are larger than the expected one. Possible causes were investigated, but without achieving a solution. Surface contamination was ruled out, since its effect is expected to be random, whilst the measurement shows consistent results for all the samples. A suggestion provided by the authors was to consider complications near the contact line, not considered in all the developed hydrodynamics theories.

In the last example provided in this short overview on micrometric beads, Peng et al. [35] considered two sets of polymethylmethacrylate (PMMA) micrometric spheres (diameter 1.19μm and 0.66μm) at a decalin-water interface. In both cases, the contact angle was not measured, but the beads were expected to have their larger part in decalin. The 2-D dynamics of the particle trapped at the interface was followed by using optical microscopy. Multi-particle tracking allowed to recover the trajectories and to measure the diffusion coefficient D_S at the interface, as a function of the area fraction n occupied by the particles. As above, we look at $n \rightarrow 0$ for single particle diffusion. The measured drag force at the water–decalin interface is $F = \beta 6\pi\eta_d Rv$, where $\eta_d = 2.5$ mPa·s is the viscosity of decalin. Despite the partial immersion in water, the diffusion at the interface is very close to the one in decalin, suggesting that the drag on the particle is much larger than the one expected at the interface. In terms of dimensionless drag coefficients, $\beta = 0.95$ for 0.66μm bead and $\beta = 1.02$ for 1.19μm bead.

All these measurements on millimetric and micrometric beads show two important features about the state of art in such a field. First, the contact angle was marginally considered and not well defined in literature. It was directly measured only with millimetric particles, when it is macroscopically visible, and generally estimated with different methods (using larger particles or by comparison with models). The dependence of the dynamics in a large range of contact angles was also not investigated. Secondly, the results are not univocally understood, and this makes the problem still open. In several cases, we read that the measured drag coefficients at the interface are underestimated by existing theoretical models [27, 28, 29]. This aspects are considered instead in this thesis, in which we attempt to fill the gap in these directions.

Several recent works extend the range of particle sizes and probed also the Brownian dynamics of nanoparticles at fluid interfaces. Wang et al. [8] studied the mobility of four types of quantum dots, different for size (in the range $5 \div 11$ nm) and surface functionality, at a water-alkane interface by fluorescence-correlation spectroscopy.

Surface diffusion coefficient D_S was measured for different alkane viscosity and compared with the volume diffusion D_V of nanoparticle totally immersed in alkane (fig. 1.10). The diffusion coefficient at the interface D_S is 1.5 - 2 times slower than the corresponding value in the bulk, against the theoretical prediction reported

ref.	θ [°]	β_{exp}	β_{th}
Petkov et al. [30]	48.7	0.68	0.73
Petkov et al. [30]	53	0.66	0.72
Petkov et al. [30]	82	0.54	0.62
Radoev et al. [31]	-	0.6-1.5	< 0.79
Sickert et al. [32]	50	0.84	0.73
Chen and Tong [34]	64	0.69	0.69
Chen and Tong [34]	64	0.84	0.69
Chen and Tong [34]	64	0.85	0.69

Table 1.2: Overview of the results on diffusion of beads, as found in literature. For each measurement, we report the author, the contact angle θ, the experimental dimensionless drag coefficient β_{exp} and its theoretical prediction β_{th}, as expected by Fischer et al. [29].

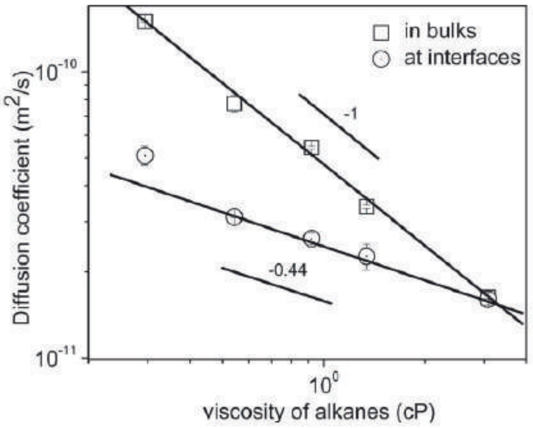

Figure 1.10: Diffusion coefficients at the water-alkane interfaces (circle) as a function of the viscosity of the alkane phase. Such values are compared with the corresponding diffusion coefficient for the same particle, but totally immersed in the alkane. The diffusion is slower at the interface, against any theoretical prediction. Measurements and graph from Wang et al., Small 7, 24 (2011) [8]

above.

The anomalous behavior of nanoparticles at the interface was confirmed also by other works. Zheng et al. [10] measured the diffusion coefficient of gold NP (diameter in the range 5 – 15 nm) at the interface of a water–glycerol mixture. They found that the diffusion coefficient increases with particle size, violating the Stokes–Einstein equation that predicts the opposite behavior (fig. 1.11a). A similar behavior was found also by Du et al. [11] for particles at an oil–water interface (fig. 1.11b), in a wide range of particle diameters (24 – 2000 nm). Larger par-

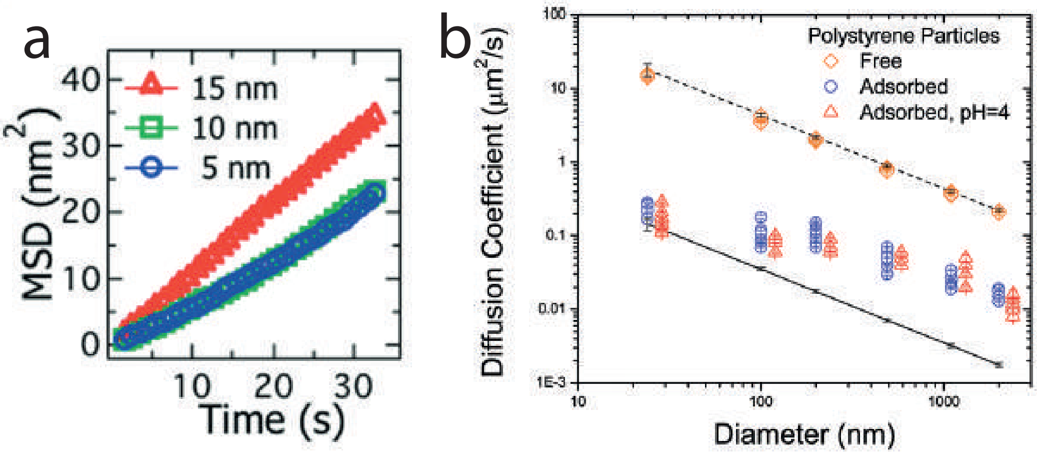

Figure 1.11: **a.** Mean Square Displacements of 3 gold nanoparticles (diameter: 5 - 10 -15 nm) as a function of the time lag. The particles are straddled at the interface of a water–glycerol mixture. The slope of the MSDs increases with the NP diameter, when a decreasing is instead expected by Stokes–Einstein equation. Measurements and graph from Zheng et al., Nanoletters 9, 6 (2009) [10]. **b.** Experimental diffusion coefficient for polystyrene particles, in a wide range of diameter (24 – 2000 nm). The predictions of Stokes–Einstein equation for a particle fully immersed in water (dashed line) and in oil (solid line) are reported. In the first case, a direct measurement (yellow diamonds) confirms the prediction. For particles straddled at an oil–water interface (blue circles) the diffusion coefficient does not follow the Stokes–Einstein behavior. The same result is observed when the charge on the particles is neutralized by changing the pH value to 4 (red triangles). Measurements and graph from Du et al., Langmuir 28, 25 (2012) [11].

ticles exhibit an intermediate diffusion coefficient, between the values of diffusion in water and in oil. A typical scaling as R^{-1}, in agreement with Stokes–Einstein equation, was also found. For smaller particles Stokes–Einstein equation is not followed and an unexpected increase in drag force at the interface occurs.

All these recent works, at both nanometric and micrometric scales and in different systems, point out a slowing–down of the diffusion at a fluid interface, suggesting that additional dissipation mechanisms enter into play at the interface.

1.5 Spheroidal particles fully immersed in a fluid

1.5.1 Theoretical model of friction coefficient

The calculation described in previous section for spherical beads can be extended to more complex morphologies. In the present work (see chapter 3) we are interested to the case of prolate spheroids with semiaxes (a, b, b). We discuss first the translational motion along the two main directions, that we denote with the indexes a (along the long axis) and b (along the short axis). In each case, the par-

ticle is moving at a given velocity v. The corresponding shear stress and pressure at the particle surface can be computed, in a similar way as done for a sphere. The integration in the spheroidal geometry provides the friction drags F_a and F_b, as computed for the first time by F. Perrin [36, 37].
For the sake of simplicity, the detailed derivation is not reported in this thesis, but it is sufficient to point out that the role of anisotropic shapes is taken into account by geometric factors. In fact, the friction drags in the two cases are written

$$F_{a,b} = 6\pi\eta b G_{a,b}(\phi) v \tag{1.49}$$

where the geometric factors $G_{a,b}(\phi)$ are functions of the aspect ratio $\phi = a/b$. They were analytically derived from Perrin' s equations [38] and plotted in fig. 1.12:

$$G_a = \frac{8}{3} \frac{1}{\left[\frac{2\phi}{1-\phi^2} + \frac{2\phi^2-1}{(\phi^2-1)^{3/2}} \ln\left(\frac{\phi+\sqrt{\phi^2-1}}{\phi-\sqrt{\phi^2-1}}\right)\right]} \tag{1.50}$$

$$G_b = \frac{8}{3} \frac{1}{\left[\frac{\phi}{\phi^2-1} + \frac{2\phi^2-3}{(\phi^2-1)^{3/2}} \ln\left(\phi + \sqrt{\phi^2-1}\right)\right]} \tag{1.51}$$

For a sphere ($\phi = 1$, $a = b = R$), we have $G_a = G_b = 1$: from eq. 1.49, it is evident that the usual Stokes–Einstein expression is recovered. At $\phi > 1$, the drag forces increase with the aspect ratio, more rapidly along the short axis.

The rotational dynamics is also considered: for a spheroid, rotating at an angular velocity ω around the short axis b (fig. 1.13), the friction drag torque is given by the same approach [36]:

$$\Gamma = 6\eta V G_\varphi(\phi)\omega \tag{1.52}$$

where V denotes the volume of the particle and the geometric factor $G_\varphi(\phi)$ (fig. 1.14) is [39]

$$G_\varphi = \frac{2}{3} \frac{\phi^4 - 1}{\phi\left[\frac{2\phi^2-1}{\sqrt{\phi^2-1}} \ln\left(\phi + \sqrt{\phi^2-1}\right) - \phi\right]} \tag{1.53}$$

The theoretical expressions for the viscous drag for spheroidal particles immersed in a fluid phase allow to write the corresponding diffusion coefficients, according to eq. 1.11. The diffusion coefficients D_a, D_b, along the long and short axis respectively, are

$$D_a = \frac{k_B T}{6\pi\eta b G_a}, \qquad D_b = \frac{k_B T}{6\pi\eta b G_b} \tag{1.54}$$

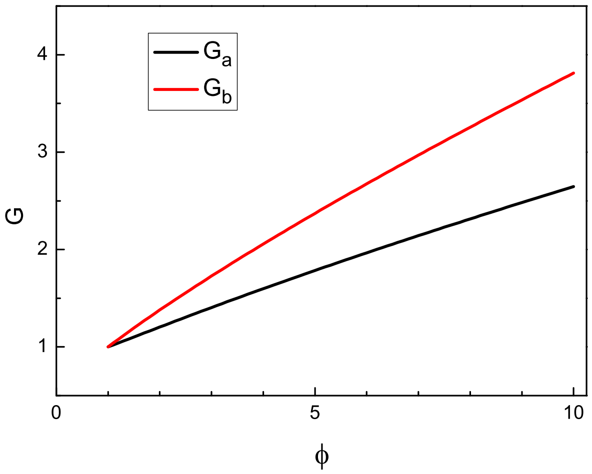

Figure 1.12: Geometric factors G_a (black line) and G_b (red line), as computed by Perrin in [36, 37] and reported in eqs. 1.50, 1.51, as a function of the aspect ratio $\phi = a/b$. Their role is to take into account the anisotropic shape of spheroids on friction drag. At $\phi = 1$, both the geometric factors are equal to 1, and we recover the expression for the sphere. For elongated particle, an increasing of the drag is expected.

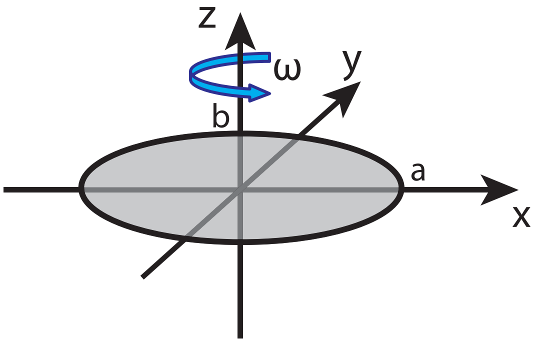

Figure 1.13: Prolate spheroid of axes (a, b, b) rotating at an angular velocity ω around a short axis b.

Similarly, the rotational diffusion coefficient D_φ around one short axis is

$$D_\varphi = \frac{k_B T}{6\eta V G_\varphi} \tag{1.55}$$

1.5.2 Experimental measurements of friction coefficient

Even if the theoretical predictions are well-known and generally accepted since longtime, the experimental confirmation of the Brownian dynamics for anisotropic

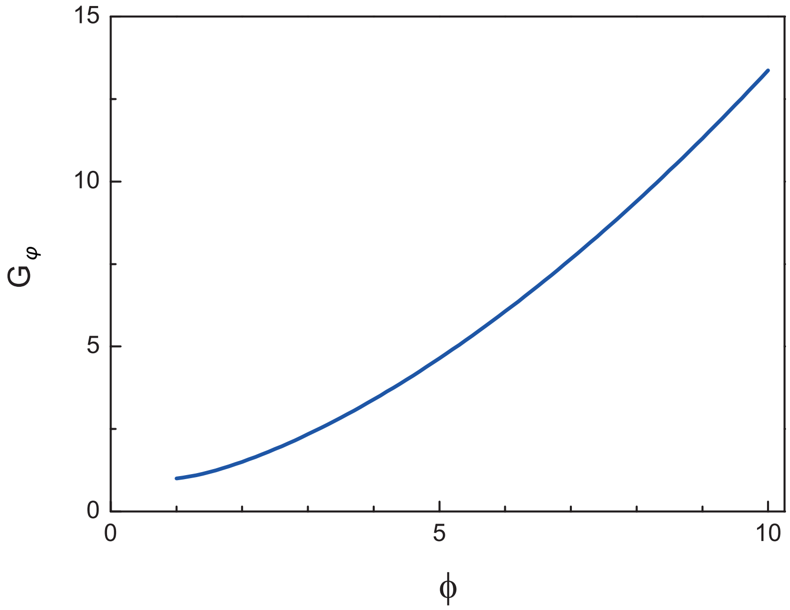

Figure 1.14: Geometric factor G_φ, as computed in [39] and reported in eq. 1.53, as a function of the aspect ratio $\phi = a/b$. Also in this case, the drag is an increasing function of the aspect ratio ϕ.

particles is a really recent achievement. In 2007, Mukhija and Solomon [5] proposed a method for a fully three-dimensional characterization of colloidal spheroids dynamics by using confocal microscopy.

Prolate spheroids were obtained from uniaxially stretched beads, in the same way as described in chapter 3 in our experiments, and dispersed in a solution of polydimethylsiloxane and CXB/decaline, with a viscosity of 2.0 ± 0.03 Pa s (2000 times larger than the water viscosity). Such a viscous medium allowed slowing down the Brownian dynamics to time scales compatible to confocal laser scanning microscopy. The Mean Square Displacements, as a function of the time lag, gave the diffusion coefficients along the long axis D_a and along the short one D_b. Such measurements were performed for two sets of prolate spheroids, with aspect ratio $\phi = 3.1 \pm 0.2$ and $\phi = 7.0 \pm 0.6$, respectively. The MSDs are plotted for the translational dynamics along the long (fig. 1.15a) and the short (fig. 1.15b) axis respectively for both the aspect ratios (red points for $\phi = 3.1$, blue points for $\phi = 7.0$). The data are then compared with the theoretical predictions (solid lines), according to the model proposed above. Their strong agreement confirms the reliability of the theory.

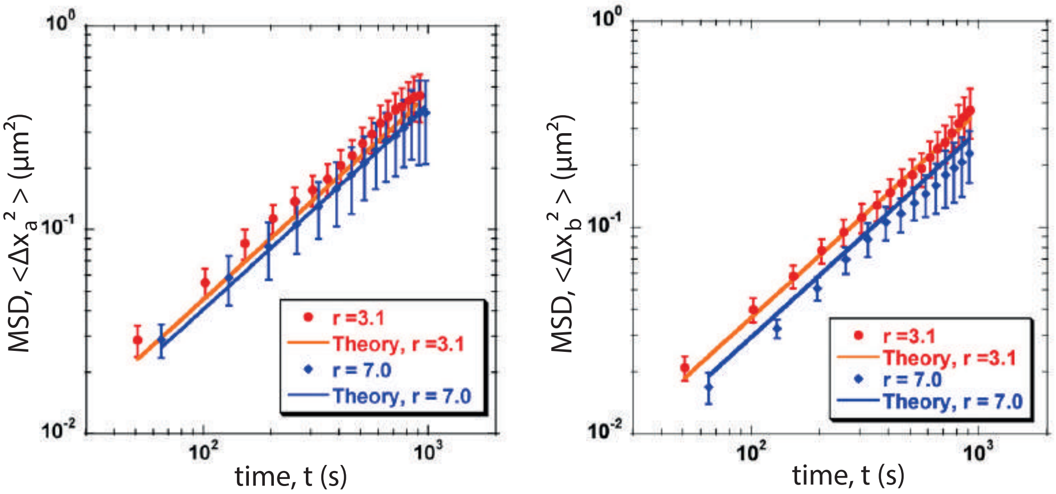

Figure 1.15: MSD vs. time lag for spheroidal particles totally immersed in a fluid, viscous phase. The displacements are here directly measured, by confocal microscopy, along the long (**a**) and the short (**b**) axes of the particle. Two aspect ratios are considered in this experience: $\phi = 3.1$ (red points) and $\phi = 7.0$ (blue points). The experimental data are compared with the theoretical predictions (solid lines), showing a strong agreement. Measurements and graphs from Mukhija et al., J Colloid Interface Sci, 314, 98106 (2007) [5].

1.6 Spheroidal particles at a fluid interface

1.6.1 Equilibrium position and deformation of the interface

The equilibrium position of a particle at an interface between two fluids comes from the equilibrium of the interfacial forces, as found in par. 1.3.1. The interface needs to fulfill the condition $\theta = const.$, where θ is the equilibrium contact angle. For the sake of simplicity, the hysteresis of the contact angle is here neglected. For a spheroidal particle, where different radii of curvature are present, a planar cut of the particle body yields an ellipse, which does not generally meet the condition of a constant contact angle. A saddle–like distortion of the contact line is thus necessary to fulfill the Young's condition. A profile of the deformed contact line, with special regard to the difference Δh between the highest and the lowest points, was derived by Loudet et al. [40]. They recovered the numerical solution of the Laplace equation for the interface height using a boundary element method. A solution of the deformation of the contact line, as a function of both the aspect ratio and the contact line, was finally achieved: $L(\phi, \theta)$ (line in fig. 1.16c).

Loudet et al. [40] provided also a direct measurement of the topography of the air-water interface around floating spheroids. Uniaxially stretched polystyrene beads were deposited at the interface and an optical trap was used to grab a single particle, at a fixed position and angular orientation. The interface profile was acquired by Phase Shifting Interferometry, whose general working principles will be detailed in chapter 2. Experimental data clearly show a deformation of the air-water interface, which is pushed down at the tips and pulled up near the middle of the particle (false color map in fig. 1.16a). A characteristic quadrupolar symmetry is also observed, suggesting that such an effect is the result of the particle shape, and not of surface roughness. This trend is not observed for spherical beads, where the interface remains flat to within the experimental resolution of 1 nm (fig. 1.16b). The analysis was performed in a full range of different aspect ratios, measuring the difference Δh between the highest and the lowest level of the interface (points in fig. 1.16c). These data confirm the presence of circular, flat contact line for spheres ($\phi = 1$) and a saddle–shape contact line for spheroids ($\phi > 1$). Moreover, the distortion of the interface increases with ϕ. Such experimental measurements are compared with the theoretical prediction of the distortion (solid line in fig. 1.16), showing the same increasing behavior predicted by the numerical simulation.

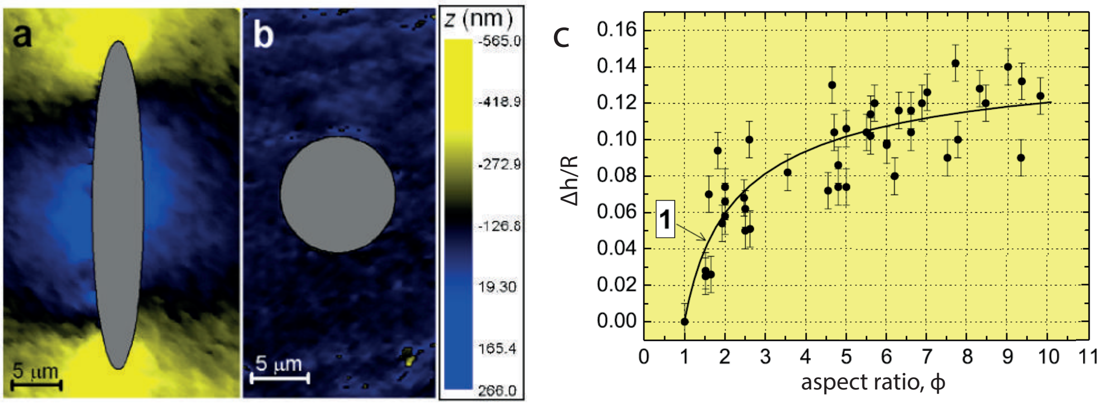

Figure 1.16: **a.-b.** False color maps of a spheroid (**a**) and a sphere (**b**) at the air-water interface, measured by J.-C. Loudet et al. via PSI technique. In the first case, a deformation of the interface is observed: the contact line is pushed down at the tips and pulled up near the middle of the particle, according to Young's law. The interface around the sphere stays instead flat. **c.** Points: experimental deformation Δh, normalized by the radius R of the initial spherical bead, as a function of the aspect ratio ϕ. Solid line: predicted deformation of the contact line, computed using the numerical method described in the text. Both theory and experiments show a flat interface for spherical bead, and an increasing distortion for prolate spheroids. Images from Loudet et al., PRL 97, 018304 (2006) [40].

The measurement of such a deformation is also used for an estimation of the contact angle of the particle [40, 41]. It is known, from the numerical solution of the Young equation around the elliptical contact line, that the maximal interface distortion Δh is a function of both the aspect ratio ϕ and the contact angle θ.

By using such a dependence, it should be possible to derive the contact angle θ from experimental measurement of Δh via PSI technique for a known aspect ratio. The contact angle obtained by this method, as a function of the aspect ratio, is reported in fig. 1.17. Since the distortion is a non–monotonous function, two different solutions for θ, at a given Δh and ϕ, could be possible (two branches in fig. 1.17). The upper branch weakly depends on the aspect ratio. In the lower branch, a slightly decreasing contact angles is observed, from $\theta = 55°$ for spheres, to $\theta = 35°$ at the maximum considered ϕ.

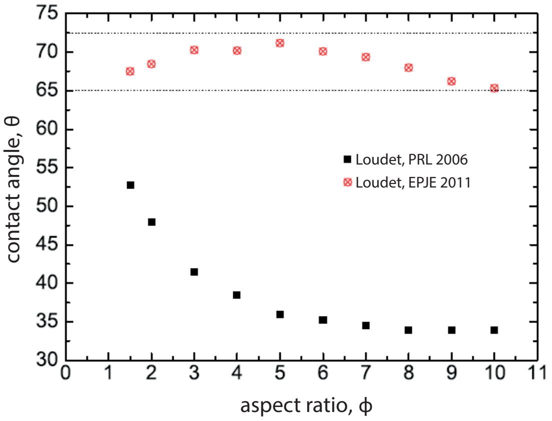

Figure 1.17: Contact angle θ as a function of the aspect ratio ϕ, obtained via PSI measurements of the distortion Δh and numerical solution of the interfacial profile. Since Δh is a non–monotonous function, two possible branches for θ are derived. Image from Loudet and Pouligny, EPJE 34, 76 (2011) [41].

1.6.2 Coupling with interface curvatures: lateral interaction

The deformation due to the spheroidal morphologies leads to an increase of the air-water interface area, with respect to the ideal (and most energetically favorable) case of a flat surface. The system tends to minimize the extension of this extra area. An example is provided by the capillary attraction of neighboring spheroids. In this case, if two spheroids are close enough, they tend to overlap their interfacial distortions and reduce the extra area, as described by Loudet et al. [42].

Another case is the coupling of the particle dynamics with the curvature of the interface, as described by Cavallaro et al. [43]. They designed an air-water interface with a radial gradient in Gaussian curvature, by pinning the surface at a vertical cylindrical micropost (fig. 1.18). A cylindrical microparticle was deposited at such a curved interface. The coupling between the quadrupolar deformation induced by the particle, and the curved interface led to a lateral force and a vertical torque. The particle rapidly rotated in order to orient its axis along the principal axes of curvature (circle of a constant radius); thereafter, it moved along the radial line toward to the center of the sample.

A curved interface adds undesirable effects to a pure diffusive motion, as angular confinement of the diffusion and/or drift. These observations justify the great attention paid to minimize the curvature of the air-water interface in the measurement performed in this thesis.

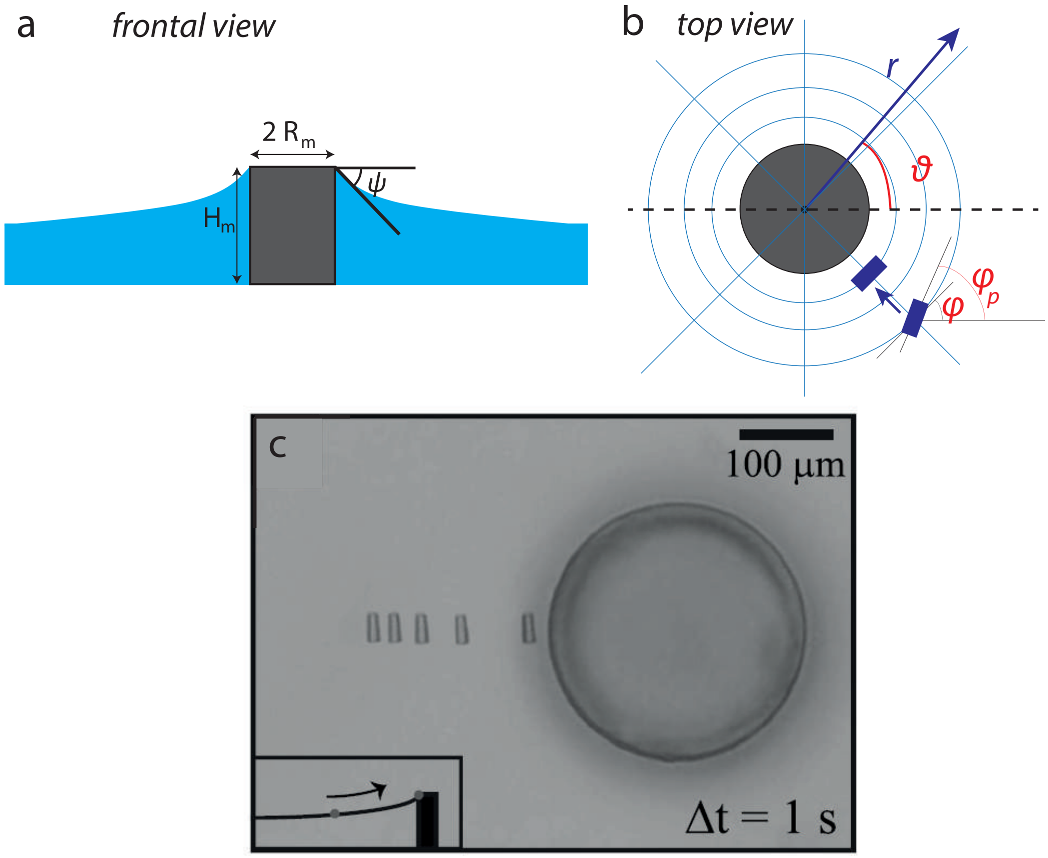

Figure 1.18: **a.** Frontal view: a cylindrical micropost is used to pin the air-water interface and induce a curvature. The slope of the interface at the micropost is given by $\tan\psi$. **b.** Top view: in a polar coordinates system (r, ϑ), the principal directions of curvature are circle of constant radius r and radial lines of constant ϑ (blue lines). φ denotes the orientation of the principal axes of curvature, and φ_p the orientation of the particle (cylindrical microrod in this experiment). **c.** Time–lapsed images of the microparticle position every 1 s. Image from Cavallaro et al., PNAS 108, 52 (2011) [43].

Non basta guardare, occorre guardare con occhi che vogliono vedere, che credono in quello che vedono.

It is not sufficient to look, you must look with eyes that want to see, that believe in what they see.

Galileo Galilei

Chapter 2

Measurement of the diffusion of spherical beads at an air–water interface

Introduction

It is well known that the motion of particles in a fluid phase is strongly affected by the viscosity of the surrounding medium. In fact, everyone is familiar with the fact that gas bubbles rise faster in champagne than in honey. A more rigorous example is provided by the Brownian motion of a colloidal particle, where the diffusion coefficient D is inversely proportional to the viscosity η of the fluid. For this same reason, in the case of a colloid straddled at the interface between two immiscible fluids, we can expect that its motion depends on the viscosity of both the phases. At the interface between air and water, where the viscosity of the air is much smaller than the viscosity of water, the effect of the former is negligible. The viscous drag is expected to be lower than the one observed for a particle fully immersed in water. Current hydrodynamic theories predict this behavior [27, 28, 29], but an experimental test of the prediction was provided just for a few set of hydrophilic particles (see par. 1.4.2).

In the present chapter, a complete study of the particle diffusion in a wide range of contact angle is addressed. Silica spherical beads with different contact angles in water are prepared and deposited at a flat air-water interface (par. 2.1). The equilibrium position of the particle at the interface and a possible particle induced deformation are measured by using interferometric techniques (par. 2.2). The diffusion coefficients D as a function of the contact angle θ is then measured (par. 2.3). The preparation of the beads and the measurements of their dynamics at the interface in the full range of contact angles have been carried out by D. Fedorenko, a former post-doc in the team. They are reported in this chapter as they guide the development of a new theoretical model, proposed in chapter 4. The measurements are repeated during this thesis at few contact angles in order to confirm the results.

2.1 Preparation of the sample

2.1.1 Particle surface treatment

The immersion depth of silica particles in water is controlled by chemically treating the silica surface. The validity of the methods is checked by Gel Trapping method [44] and the contact angle is measured for all the beads by a homemade interferometric set-up developed by C. Blanc. [45].

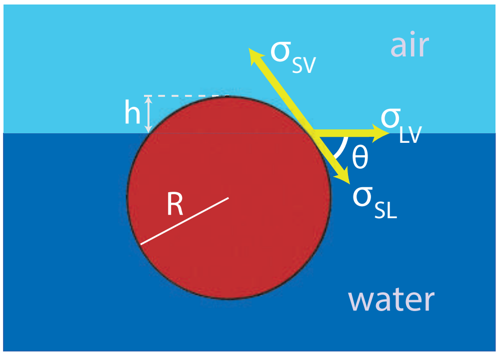

Figure 2.1: Spherical bead of radius R at the air-water interface. Its immersion depth h is a consequence of the equilibrium between the three surface forces per unit length at the contact line: σ_{SV}, σ_{SL} and σ_{LV}. Such a condition leads to the contact angle θ.

The wettability of silica particles can be changed tuning the grafting density of hydrophobic silane agents on their substrate. For this purpose, commercial silica beads with diameter of about 2μm and 4μm and purchased from Bangs Laboratories, Inc. (product code SS04N, SS05N, respectively) are used. They are sold in water solution, with concentration of 9.8% solids. Beads are first washed in a sulfochromic acid solution and then thoroughly cleaned with 5 centrifugation/cleaning cycles. After a centrifugation (4000rpm for 5 minutes) the supernatant is replaced by Millipore water and the beads redispersed in ultrasonic bath. The deionized water is produced by a Millipore Milli-Q filtration system, and has a resistivity of 18 MΩ·cm. A solution of DMOAP (N,N-Dimethyl-N-octadecyl-3-aminopropyltrimethoxysilyl chloride), $0.1 - 5\%$ wt in demineralized water and methyl alcohol (10% − 90%) is used. The beads are added into the silane solution (approximately 0.5 ml of beads in water per 1 ml of silane solution). The solution is then mixed with a vortex mixer during a variable time interval, according to the wettability we want to achieve. Particles left for 1 minute in silane solution give a contact angle $\theta = 68°$; particles left from 30 to 120 minutes give $\theta = 95° \div 120°$. Solvents and exceeding silane molecules are removed by 10 centrifugation/cleaning cycles. The resulting contact angle ranges from $\theta = 30°$ (pure silica particle, only washed with sulfochromic acid) to $\theta = 120°$. Higher contact angles (up to $\theta = 140°$) are achieved by using the same procedure as for obtaining $\theta = 120°$ contact angles but a different deposition process: beads are first dried in an oven at 120°C for 2 hours and deposited dried at the interface.

2.1.2 Interface preparation

Sets of particles with different surface wettability are deposited at the air-water interface in order to analyze their dynamics. We use a small cylindrical container of 10 mm in diameter, fixed on a microscope glass slide. During particle tracking experiments (par. 2.3), the container is covered by a thin flat piece of borosilicate glass, in order to avoid contamination of the interface or evaporation of the water. Such a coverture is not used during interferometric measurements (par. 2.2.2), when a direct contact between the light beam and the sample is needed. Deionized water partially fills up to 0.8 mm in height the container. Smaller quantities do not allow to fill homogeneously the container and obtain a flat interface. Larger quantities of water cannot be used in order to minimize convective flow in the sample. Beads dispersed in water are sprayed on the interface with an airbrush or directly dried to avoid any possible surface contaminants. Most of the beads stay trapped at the interface, and just a little portion sinks down into the bulk. Very dilute bead surface concentrations (less than 0.01% s/s) are used to get rid of possible interactions between them. The air-water surface tension is directly measured by Wilhelmy plate method at a free interface, with and without silanized beads. Both the measurements are in agreement with the literature value of the air-water surface tension ($\sigma_{LV} = 0.072$ N/m).

2.2 Techniques for contact angle measurement

2.2.1 Gel Trapping technique

The efficiency of the surface treatment to tune the contact angle is verified by the Gel Trapping technique. In this method, the bead is trapped at the interface between air and gelled water. The surface tension of gelled water is the same as

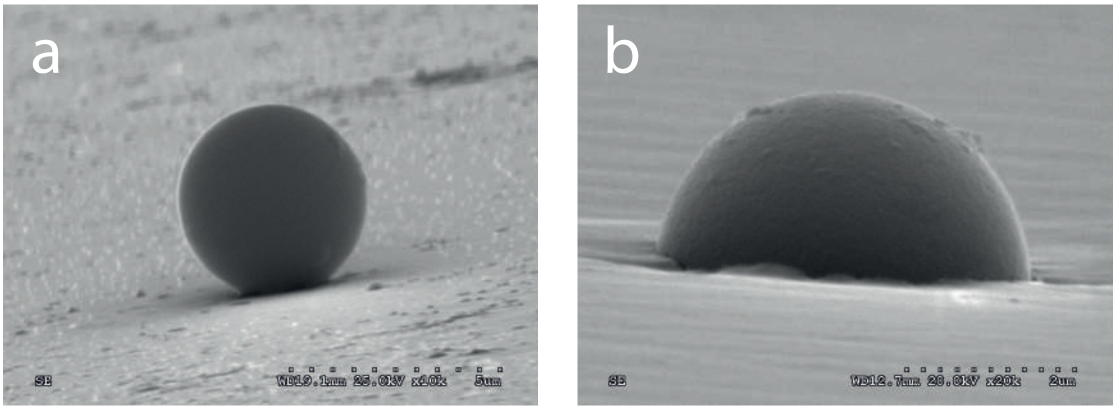

Figure 2.2: SEM images of beads trapped in polymerized NOA81. Their contact angles at air-water interface are $\theta = 30°$ (**a**) and $\theta = 90°$ (**b**). The visible part of the beads is the one previously immersed in water. The contact angles can be recovered from their immersion in the polymer, with respect to their size. Such images show the validity of chemical surface treatment in tuning the contact angle. Courtesy M. Medfai and C. Blanc.

pure water ($\sigma_{LV} = 0.072$ N/m), so we expect that the immersion depth is not changed. The gelling agent used here is Phytagel, purchased from Sigma-Aldrich (product code P8169). A Phytagel solution at 2% wt in Millipore water is prepared by heating at 90°C and mixing by magnetic stirrer. The solution is cooled to room temperature to allow the gel to set. Spherical beads are spread on the gel surface and then the system is heated again at 90°C in order to trap the particles at the interface. Norland Optical Adhesive 81 (NOA81) is poured over the gelled water with the particles trapped at its interface and photopolymerized by ultraviolet light in 2 minutes. The polymerized NOA81 is peeled off the gel surface, leaving the beads at a complementary position with respect to the air-water interface. The sample is finally prepared to be observed by Scanning Electron Microscopy (SEM) (fig. 2.2). From these images, the microspheres immersion in water (corresponding to the visible part of the bead) can be easily measured. Since this quantity is $2R - h$ (R and h have been shown in fig. 2.1), the contact angle is recovered by the expression:

$$\cos\theta = 1 - \frac{h}{R} \tag{2.1}$$

2.2.2 In situ interferometric techniques

Interferometric techniques allow to reconstruct a 3-D profile of the interface. The measurements are performed by an optical microscope (LEICA DM 2500P), equipped with a digital camera and a Mirau interferometry objective.

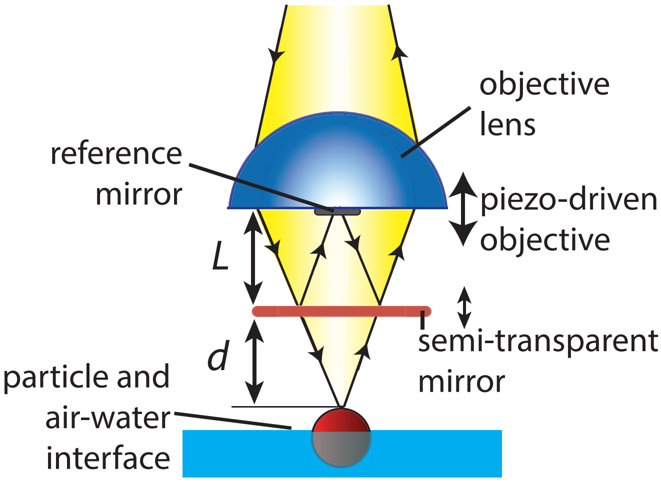

Figure 2.3: Scheme of the Mirau interferometry objective. A semi-transparent mirror splits the white light into two arms. L is the fixed distance between the beamsplitter and a reference mirror, inside the objective. d is the distance between the beamspitter and the surface of the sample. The objective is shifted vertically by a piezo-electric device. See the main text for the details of its operating condition.

The Mirau interferometry objective is produced by Nikon and it has a 20X magnification. A scheme is shown in fig. 2.3.

A light beam passes through a semi-transparent mirror and it is split into two arms: a sample arm directed to the particle and to the interface and a reference arm directed to a built-in reference mirror. The two beams, reflected by the respective surfaces, recombine on a charge-coupled device (CCD) camera creating a fringe interference pattern. This pattern depends on the difference of the optical paths between the two arms, i.e. on the topography of the surface of the sample. The objective is then displaced along the optical axis by a piezoelectric nanopositioner (Nano-Drive from MCL) and a new pattern is taken. The acquisition of the images and the displacement of the objective are both driven by a Labview software. The analysis of the evolution of the pattern as a function of the position of the reference mirror allows us to visualize the topography of the sample surface. The interferometer can be used in two different operating modes: Vertical Scanning Interferometry (VSI) and Phase Shifting Interferometry (PSI). VSI is here used to measure the contact angle at a fluid interface, whilst PSI allows to detect interface deformation.

Working principle of Vertical Scanning Interferometry (VSI)

In Vertical Scanning Interferometry (VSI), white light from a microscope bulb is used. An external power supply provides a constant 12V tension during the measurement to ensure constant light intensity. For each wavelength λ, the intensity $I_\lambda(x, y, d)$ detected at the pixel (x, y) of the CCD camera, when d is the distance between the beamsplitter and the sample, is written:

$$I_\lambda(x, y, d) = I_0(\lambda)[1 + \gamma_0 \cos \Delta\phi(x, y, d)] \tag{2.2}$$

$I_0(\lambda)$ denotes the intensity of the incident beam, γ_0 is a coherence function and $\Delta\phi(x, y, d)$ is the phase shift due to the difference of the optical paths:

$$\Delta\phi(x, y, d) = 4\pi[L - d(x, y)]/\lambda \tag{2.3}$$

where L is the fixed distance between the beamsplitter and the reference mirror (see fig. 2.3).

The overall intensity is given by summing on all the wavelengths in the whole spectrum $[\lambda_1, \lambda_2]$:

$$I(x, y, d) = \int_{\lambda_1}^{\lambda_2} I_0(\lambda)[1 + \gamma_0 \cos \Delta\phi(x, y, d)]d\lambda \tag{2.4}$$

The intensity in each pixel (x, y) is analyzed separately. A vertical scanning of the reference mirror, controlled by the piezo-electric positioner, provides the behavior of $I(x, y, d)$ as a function of the distance d. For each pixel (x, y), the curve I vs. d has a Gaussian envelope with a periodical modulation (fig. 2.4), due to the superposition of the interference of several wavelengths. The maximum intensity is obtained when a constructive interference is achieved at all the wavelengths, i.e. when there is no difference between the two optical paths: $d = L$.

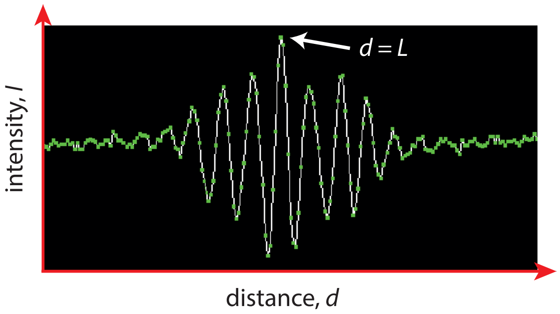

Figure 2.4: Typical measured evolution of the overall intensity I detected at a generic pixel of the CCD camera, as a function of the distance d between the beamsplitter and the sample, during a vertical displacement of the Mirau objective. The recorded intensity has a Gaussian envelope with a periodical modulation, due to the superposition the wavelengths in the whole spectrum. The maximum intensity is achieved when the optical paths of the two arms are equal, i.e. when $d = L$.

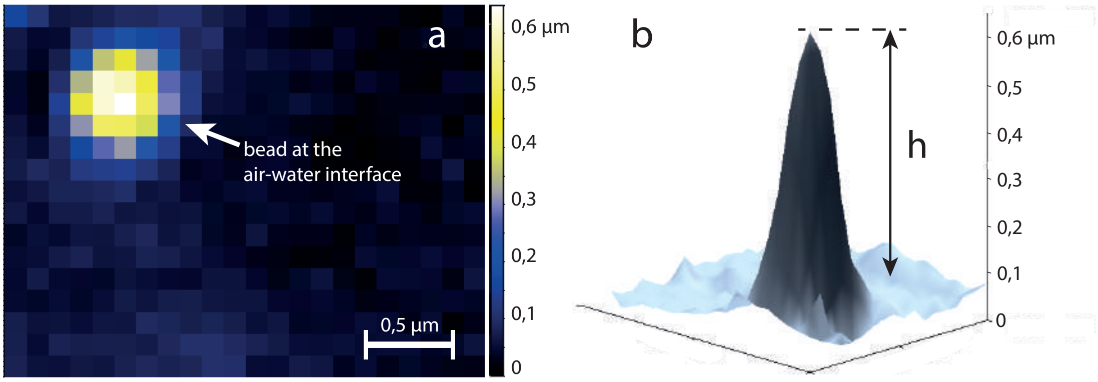

Figure 2.5: **a.** False color maps of the height profile of the sample. Each pixel has a color corresponding to the detected height, with respect to the flat interface, ranging from dark blue (interface, $h = 0$) to yellow (top of the bead, $h = 0.6\mu$m). **b.** 3-D reconstruction (not in scale) of the interface profile. The distance h between the top of the bead and the flat interface is recovered.

An IDL software finds the peak of intensity for the position (x, y), i.e. the corresponding value of the distance d. Since the position of the objective is controlled by the piezo-electric device, a 3-D profile $h(x, y)$ of the interface is reconstructed.

Experimental results from VSI technique

For a VSI measurement, the objective is displaced over 2μm, in order to get the whole profile of the emerging particle and the surrounding interface. For each position of the objective, 15 images are taken (acquisition rate of the CCD camera: 30 frame/s) and they are averaged to rule out the effect of electronic noise. The vertical scanning is effectuated for 100 different positions d of the reference mirror. It follows that the time required for a complete measurement is about 50 s. The resulting length of a single step of the objective, and the vertical resolution of the measurement, is so fixed to 20 nm. Note that this value is not the best achievable resolution (minimum displacement of the piezo-electric positioner: 1 nm), but it is sufficient for our purpose, as explained in the following, and it allows to explore the suitable spatial range in a relatively short time. The lateral resolution is limited by the optical resolution of the objective (size of a pixel: 0.228μm). The set of 100 averaged images is analyzed via IDL and the 3-D profile of the particle at the interface is then reconstructed (fig. 2.5).

Such a profile is used to determine the contact angle θ. The height h of the top of the bead, with respect to the flat interface, is computed. If we denote with R the radius of the sphere, we obtain, via trigonometry:

$$\cos\theta = 1 - \frac{h}{R} \tag{2.5}$$

The uncertainty on the contact angle estimation is due to both the vertical resolution of VSI $\Delta h = 20$ nm, as reported above, and from the uncertainty on the beads radius: $\Delta R \approx 0.1R$ for the typical beads used. The error is then

$$\Delta\theta = \frac{1}{\sin\theta}\left[\frac{\Delta h}{R} + \frac{h\Delta R}{R^2}\right] \tag{2.6}$$

The main contribution to the error is given by ΔR. This circumstance justifies the large step value $\Delta h = 20$ nm of the vertical piezo–scan chosen in VSI experiments.

Such errors strongly increase with the contact angle. The error is $\Delta\theta = \pm 2.7°$ at $\theta = 30°$ and $\Delta\theta = \pm 19.3°$ for $\theta = 145°$.

Working principle of Phase Shifting Interferometry (PSI)

In Phase Shifting Interferometry (PSI), the experimental set-up is the same as for VSI, except for the light beam that is involved [40]. Here, the light passes through an interference filter (spectral band: 5 nm) centered at the wavelength of 633 nm. The light is so considered monochromatic. The intensity detected by the CCD camera is the one shown in eq. 2.2:

$$I_\lambda(x, y, d) = I_0(\lambda)\left[1 + \gamma_0 \cos\frac{4\pi[L - d(x, y)]}{\lambda}\right] \tag{2.7}$$

where $\lambda = 633$ nm.

The intensity is a sinusoidal function of the vertical displacement d with period $\lambda/2$ (fig. 2.6). Contrary to the VSI, the periodicity of the signal is conserved due to the light coherence. For each pixel (x, y) the signal is shifted, with respect to a reference curve ($h = 0$), by a phase

$$\Delta\phi = \frac{4\pi h(x, y)}{\lambda} \tag{2.8}$$

related to the profile of the reflective surface of the sample. Since a phase shift is defined in the range $[0, 2\pi]$, the profile $h(x, y)$ can be recovered just over a vertical displacement $\lambda/2$. This limitation does not allow to detect the absolute position of the surface of the bead, but it is sufficient for characterizing the deformations of the air-water interface. Note that the characteristic of this technique enhances the vertical resolution up to 1 nm. Lateral resolution is, as in the case of VSI, given by the optical resolution of the objective.

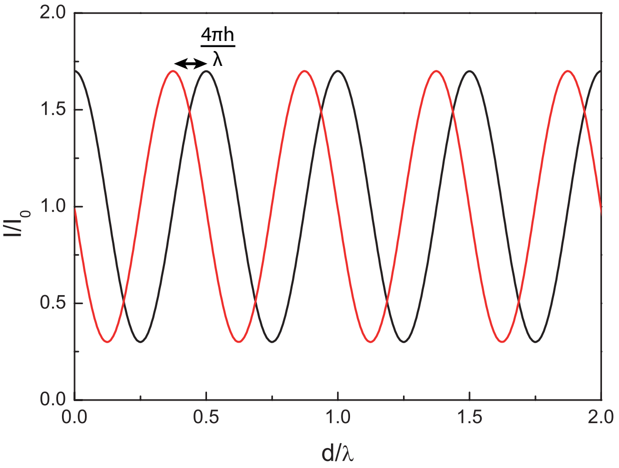

Figure 2.6: Typical theoretical behavior of the normalized intensity I/I_0 as a function of the displacement d, expressed in unit of wavelength λ. The intensity has a sinusoidal behavior, according to eq. 2.2, when a single wavelength is used. The intensities reflected by two points with different heights are considered: $h = 0$ (black curve, reference position) and $h = 80$ nm (red curve). The differences in the values of h translate in the phase shift of the signal $\Delta\phi = 4\pi h(x, y)/\lambda$.

Experimental results from PSI technique

For a PSI measurement, the reference mirror is displaced over a distance equal to the wavelength of light beam, i.e. $\lambda = 633$ nm, corresponding to 2 periods of the intensity signal. The interference intensity on each pixel is sampled in 20 points and the phase shift between pixels is calculated. As in VSI, for each point (position of the reference mirror), 15 images are taken (acquisition rate of the CCD camera: 30 frame/s) and averaged to rule out the effect of electronic noise. A measurement of the interface deformation is achieved in less than 10 s due to the small number of acquisition points that is required.

A typical PSI measurement for a spherical particle shows that the interface is flat and no deformations are detected to within the experimental resolution ($\Delta h \simeq 1$ nm). This result is expected by a constant macroscopic contact angle condition at the contact line [40]. Only the air-water interface profile is visible and analyzed. The zone occupied by the bead is out of scale and it is not accounted by the PSI measurement.

2.3 Dynamics of the particle

2.3.1 Particle tracking

The motion of individual beads at the air-water interface is followed by bright field microscopy. The optical microscope (LEICA DM 2500 P) is mounted on an anti-vibration table. The focal plane is at the same height of the air-water interface. Since the particles are trapped at the interface, they stay in the focal plane during the whole measurement. The dynamics is observed for 10 minutes approximately in each measurement and a digital video is recorded by a firewire charge-coupled device (CCD) camera at 30 frame/s. In each video, a region of $120 \times 90 \mu\text{m}^2$ (1024×768 px^2) is explored. We apply standard particle tracking methods [46] to get the position (x, y) of the intensity center of mass of the bead in each frame. Repeating the procedure for all the frames of the recorded video, the evolution in time of the particle trajectory is obtained. These operations are performed by using an IDL software (see appendix A.1), whose operating principles are here briefly resumed.

A frame recorded by the used CCD camera is an 8-Bit grayscale image. This means that image pixels are stored in binary, quantized form and 256 (2^8) intensity values are allowed, ranging between 0 (black) and 255 (white). The precision provided by this format is barely sufficient to avoid visible banding artifacts, but very convenient for programming due to the fact that a single pixel then occupies a single byte. In this kind of recorded images, a particle looks like a dark circle over a gray-white background. First of all, the negative image is created ($I_1(x, y) = 255 - I_0(x, y)$), where $I_0(x, y)$ is the field of intensity in the recorded image. A value corresponding to the actual average background intensity I_{bg} is subtracted: $I_2(x, y) = I_1(x, y) - I_{bg}$, with $I_{bg} \sim 20 - 30$. In this way, we obtain a new image where the intensities $I_2(x, y)$ are non-null at the particle and 0 elsewhere, if I_{bg} has been chosen properly. The $(\overline{x}, \overline{y})$ position of each particle is then calculated by the intensity center of mass expression (eq. 2.9):

$$\overline{x} = \frac{\sum x I_2(x, y)}{\sum I_2(x, y)} \qquad \overline{y} = \frac{\sum y I_2(x, y)}{\sum I_2(x, y)} \tag{2.9}$$

This position is expressed in pixel units in the lab frame and refers to the time $t_n = n(1/30)$ s, where n is number of the considered frame.

With the proposed method, a spatial resolution of 4 nm in the detection of the particle position is achieved. This value has been checked applying particle tracking to beads stuck on a microscope glass slide. Their position, taken at different times, has a normal distribution with a 4 nm-width.

The displacements $\Delta x = x - \langle x \rangle$ and $\Delta y = y - \langle y \rangle$, where $\langle x \rangle$ and $\langle y \rangle$ are the mean positions averaged in time, are considered after a numerical treatment of the trajectories, in order to discard the contribution of drift motion (see par. 2.3.2). Two typical Δx-Δy trajectories for hydrophilic (fig. 2.7a) and hydrophobic (fig.2.7b) particles, during the same time interval of $\Delta t = 100$s, are reported.

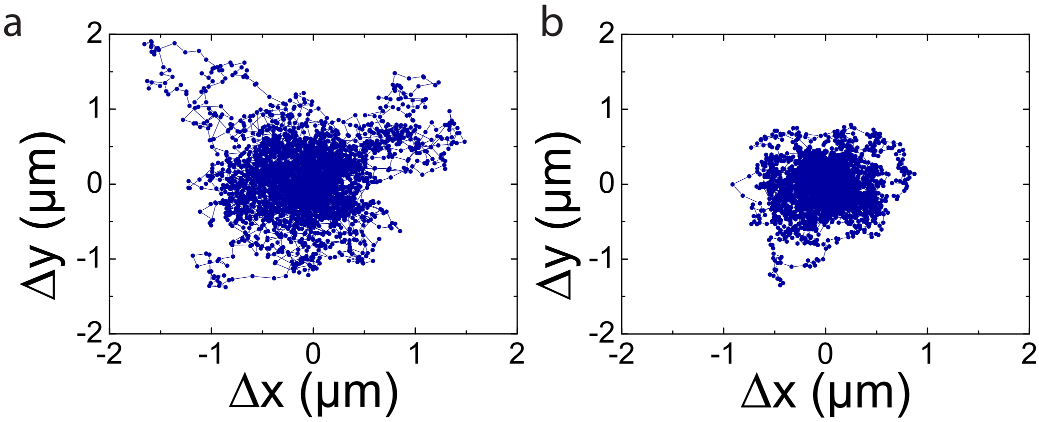

Figure 2.7: Δx-Δy trajectories recorded with the proposed techniques during the same time interval $\Delta t = 100$ s of a hydrophilic ($\theta = 30°$) (**a**) and of a hydrophobic particle ($\theta = 138°$) (**b**). The hydrophilic bead, having its larger part in water, explores a larger area than the hydrophobic one, against the reasonably expected behavior.

Surprisingly, the more hydrophilic bead (fig. 2.7a), having its larger part in the high viscosity medium (water), explores a larger area than the hydrophobic one (fig. 2.7b).

2.3.2 Drift removal statistical technique

The motion of colloidal particle at an air–water interface is often affected by convective flows, which add to the Brownian motion described above. The reasons of such a motion are still unclear, but possible sources can be found in radial gradient of curvature [43] (see par. 1.6.2) or local thermal gradient induced by microscope lightening. The resulting dynamics recorded during particle tracking experiments is thus the sum of two different contributions: diffusive motion, at which we are interested, and drift motion. In order to rule out the latter, an algorithm has been conceived and implemented by an IDL software. The purpose is to find the best approximation for drift trajectories and subtract them from the recorded ones. This operation is possible and justified since the two mechanisms take place at different time scales.

Let us consider the position of the particle as a function of time (black line in 2.8). In a first stage, a constant drift is considered. It appears as a straight line in the position–time plot, connecting the first and the last points. If we assume that the drift velocity changes in time, such a motion is represented by a polygonal chain (blue lines in fig. 2.8).

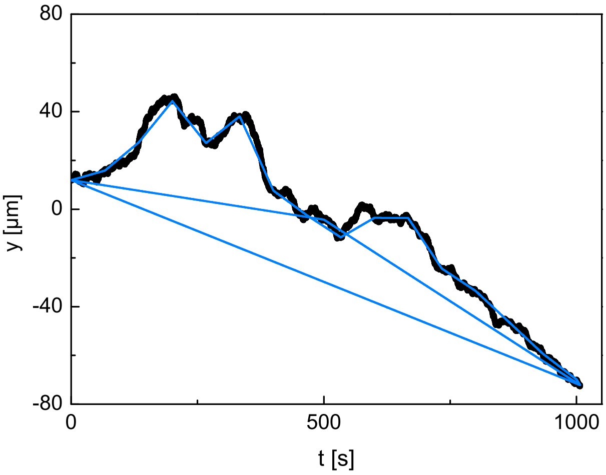

Figure 2.8: Black line: y–position of a particle, as a function of the time t, recorded in particle tracking experiment. Blue lines: drift approximations $y_d(t; t_d)$ assuming three different time interval t_d ($t_d = 60$ s, 500 s, 1000 s).

To be more quantitative, the drift velocity in the interfacial plane is denoted as $\mathbf{u} = [u_x, u_y]$. We assume that the drift velocity changes every time t_d. For the time interval j the velocity is written as:

$$u_{x,j} = \frac{x[jt_d] - x[(j-1)t_d]}{t_d} \qquad u_{y,j} = \frac{y[jt_d] - y[(j-1)t_d]}{t_d} \tag{2.10}$$

where $x(t)$ and $y(t)$ denote the position of the particle at the time t. The drift curves $x_d(t; t_d)$ and $y_d(t; t_d)$, as a function of time t and at a given t_d, write:

$$x_d(t; t_d) = x[(j-1)t_d] + u_{x,j}\,[t - (j-1)t_d] \tag{2.11}$$

$$y_d(t; t_d) = y[(j-1)t_d] + u_{y,j}\,[t - (j-1)t_d] \tag{2.12}$$

Different estimations for t_d are considered. For each one, a corrected trajectory, corresponding in principle to a diffusive dynamics, is recovered:

$$(\bar{x}(t; t_d), \bar{y}(t; t_d)) = (x(t) - x_d(t; t_d), y(t) - y_d(t; t_d))$$

The Mean Square Displacement $\langle \Delta \bar{x}^2 \rangle$ is computed as a function of the time lag τ, following the techniques described in par. 2.3 (fig. 2.9).

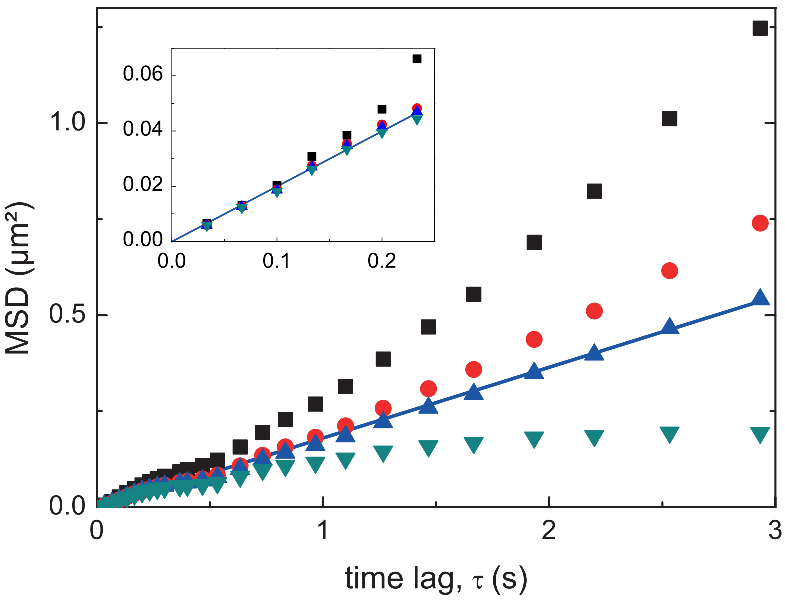

Figure 2.9: MSD as function of the time lag τ for the same particle trajectory, corrected using different t_d: $t_d = 5$ s (green points), 60 s (blue points), 500 s (red points), and 1000 s (black points). *Inset*: detail of MSD at very short time lags, where the slope is not affected by the drift correction.

All of them show the same slope at very short time lags (inset in fig. 2.9) since, at these scales, the dynamics is not affected by the drift. At larger time lags, the MSD behavior depends on the chosen drift correction. The best drift correction is the one that provides a linear dependence MSD vs. τ, as expected in a Brownian regime: $\langle \Delta x^2 \rangle_{th} = A\tau$, where A is the fitting parameter. A linear fit is proposed for all the corrected trajectories, and the χ^2 function is calculated:

$$\chi^2 = \sum \left(\langle \Delta x^2 \rangle - A\tau \right)^2 \tag{2.13}$$

The value of t_d that minimizes χ^2 is chosen to write the best approximation of the drift trajectory and to recover the Brownian trajectories analyzed.

Typical drift velocities, found with the described method, are around 0.1μm/s and do not depend on the bead contact angle.

2.3.3 Statistical analysis of the particle dynamics

The $\Delta x - \Delta y$ trajectories of the particles are used to extract information about the dynamics of the beads. The analysis of the distribution of the displacements and of the behavior of the Mean Square Displacements (MSDs) as a function of the time lag allows to achieve this purpose. The input for this analysis is a set of N couples $(x(t_n), y(t_n))$, i.e. the position of the center of the bead in the n-th frame, where n goes from 0 to $N-1$. The time t_n is simply related to the index of each frame n: $t_n = n(1/30)$. Let us now consider a given time lag τ_i; the minimum achievable value is fixed by the time resolution 1/30 s. All the possible displacements that occur during such a time τ_i are calculated:

$$[\Delta x_i(t_n), \Delta y_i(t_n)] = [x(t_n+\tau_i) - x(t_n), y(t_n+\tau_i) - y(t_n)] \tag{2.14}$$

where $0 < t_n < N(1/30)s - \tau_i$ and the index i denotes the dependence on the chosen time lag.

The displacements $[\Delta x_i(t_n), \Delta y_i(t_n)]$ are normally distributed around the mean position $\langle \Delta x_i \rangle_n = \langle \Delta y_i \rangle_n = 0$ (fig. 2.10). The symbol $\langle \cdot \rangle_n$ stands for the average over all the displacements at different time t_n. Such a Gaussian distribution suggests a randomized origin of the motion and the presence of a diffusive regime. Moreover, due to the isotropy of the system, the distributions for Δx and Δy at the same contact angle have similar behavior (see fig. 2.10a,c and 2.10b,d). For the sake of clarity, the distribution of Δx and of Δy are reported here for two characteristic contact angle, $\theta = 30°$ and $\theta = 138°$.

Since a diffusive regime is observed, the translational diffusion coefficient D is considered. The width of each distribution is related to such a coefficient and to the considered time lag τ_i. In this case, the standard deviation σ_i can be written as:

$$\sigma_i = \sqrt{2D\tau_i} \tag{2.15}$$

where $D = D_x = D_y$ is the measured translational diffusion coefficient.

The same value can be computed as the Mean Square Displacements (MSDs):

$$\sigma_i = \langle \Delta x_i^2 \rangle_n = 2D\tau_i \tag{2.16}$$

$\langle \Delta x_i^2 \rangle_n$ and $\langle \Delta y_i^2 \rangle_n$ are estimated for different values of τ_i; the results are plotted in 2.11 for 4 sample beads with different contact angles.

We recover the linear behavior predicted in 2.16, typical of a diffusive regime, and we use the slope of each curve to get the corresponding diffusion coefficient D at a given contact angle (table 2.1).

As seen for the trajectories, the results are counter-intuitive: the slopes, i.e. the diffusion coefficients, decrease when the particle is less immersed in water.

2.3.4 Diffusion coefficient vs. particle contact angle

These unexpected results motivate a complete study of the diffusion at the interface in the full range of accessible contact angles.

In fig. 2.12 the ratio between the diffusion coefficients at the surface and in the bulk $r = D_S/D_B$ is reported versus the contact angle θ. Each point on the

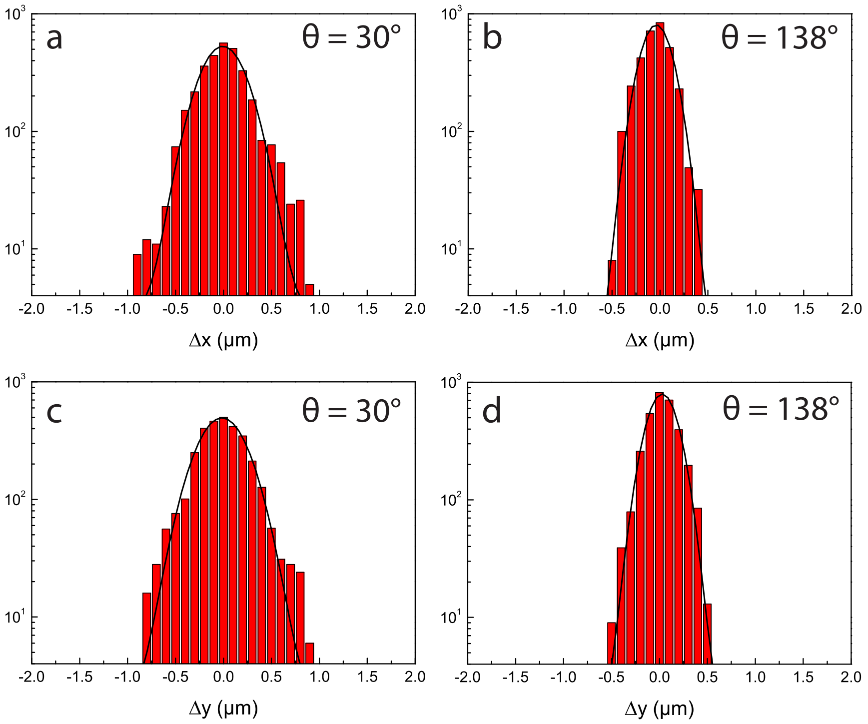

Figure 2.10: Distribution of the displacements Δx, Δy at time lag $\tau = 2(1/30)$ s, in a semi-log scale. The shapes of all the four graphs confirm the Gaussian distribution of the displacements. Such displacements are recovered from the two trajectories previously shown in fig. 2.7, considering the same time interval $\Delta t = 100$ s. **a**. Δx for the hydrophilic bead ($\theta = 30°$); **b**. Δx for the hydrophobic bead ($\theta = 138°$); **c**. Δy for the hydrophilic bead ($\theta = 30°$); **d**. Δy for the hydrophobic bead ($\theta = 138°$). The distributions Δx and Δy at the same contact angle show the same width. Hydrophilic beads have a wider distribution than the hydrophobic ones.

θ [°]	D [$\mu m^2/s$]
30 ± 2.6	0.272 ± 0.007
68 ± 4.4	0.266 ± 0.009
110 ± 8.2	0.234 ± 0.010
138 ± 15.0	0.148 ± 0.012

Table 2.1: Diffusion coefficients at the air–water interface for particles with different contact angles ($\theta = 30°, 68°, 110°, 138°$). The data are recovered from the MSD curves in fig. 2.11.

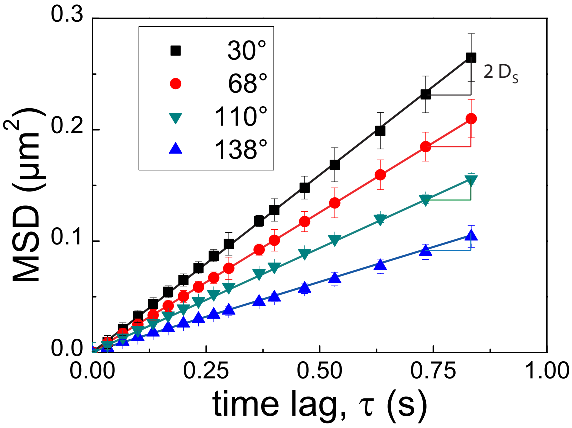

Figure 2.11: MSD as function of the time lag τ for particles with different contact angles ($\theta = 30°, 68°, 110°, 138°$). The linear behavior denotes the diffusive regime. The slope of each curve corresponds to $2D$, where D is the diffusion coefficient at a given contact angle. A decreasing of the slope, i.e. a slower dynamics, is observed for less immersed particles (higher contact angles), against common intuition.

fig. 2.12 corresponds to average values on 5 to 10 different beads with the same surface treatment. The contact angle θ is measured via VSI technique. D_S is achieved by particle tracking and statistical analysis of the trajectories, as shown above. Diffusion coefficients in the volume D_V are known from Stokes-Einstein theory (par. 1.2.1) and they are calculated for each particle using the expression:

$$D_V = \frac{k_B T}{6\pi\eta_W R} \tag{2.17}$$

where $\eta_W = 1.001 \cdot 10^{-3}$ Pa·s is the viscosity of the water at $T = 25°\mathrm{C}$ and R is the radius of the beads. To give robustness to the measurements, such a theoretical prediction is experimentally verified for few sample particles, treated to give different contact angles when at the interface. Two beads with diameter $2R = 4\mu\mathrm{m}$ and $\theta = 60°, 110°$ at room temperature ($T = 25°\mathrm{C}$) show an experimental bulk diffusion coefficient of $D_{V,exp} = 0.108 \pm 0.006\mu\mathrm{m}^2/\mathrm{s}$ and $D_{V,exp} = 0.111 \pm 0.007\mu\mathrm{m}^2/\mathrm{s}$, respectively. These measurements provide the same value for D_V: as expected, different surface treatments have no role in the diffusion in the volume. This means that surface treatments play a role just in the immersion depth of the particle, and not in its dynamics. Moreover, such experimental values are in fairly agreement with Stokes-Einstein prediction: $D_{V,th} = 0.106\mu\mathrm{m}^2/\mathrm{s}$.

The diffusion is measured for beads of 2μm, 4μm and 8μm in diameter (circle, square and triangle points respectively in fig. 2.12). At a given contact angle θ, the same values for the ratio D_S/D_V (in the limit of the error bars) is achieved for all the sizes. A strong variation of almost two orders of magnitude of the particle mass makes no difference in dynamics, ruling out any gravitational effect (e.g., formation of a particle induced meniscus). The diffusion of silica beads at an air–hexanol interface ($\theta = 83°$) is also measured (red point in fig. 2.12). The normalized diffusion coefficient, when the role of bulk viscosity is discarded, agrees with the data at the air–water interface, indicating that the measured effect is not water–dependent. To exclude possible artifacts, as interface contaminations by silane agent, the diffusion coefficients of the two sets of beads, respectively at $\theta = 28°$ and $\theta = 90°$, sharing exactly the same interface are measured (open points in fig. 2.12). The values of the diffusion coefficient at $\theta = 28°$ in presence of silanized particles is the same as the one when the beads at $\theta = 28°$ are alone at the interface, indicating that the interface is not contaminated by the release of silane from hydrophobic beads. Moreover, such a value agrees with the theoretical predictions (solid lines in fig. 2.12), in which a clean interface is considered. The slowed–down diffusion of the bead at $\theta = 90°$, deposited at the same interface, cannot be attributed to surface contaminations.

The ratio $r = D_S/D_V$ is analyzed as a function of the contact angle θ. For this purpose, we keep in mind our initial considerations, i.e. that an increasing diffusion is suggested by common intuition when the particle is less immersed in water. Hydrodynamics theories (solid lines in fig. 2.12), that will be discussed later, qualitatively confirm this prediction. For a bare silica particle ($\theta = 30°$), we have $r \simeq 1.25$: thus, the beads diffuse more at the interface than in the bulk. In a small range of contact angle ($\theta \sim 30° - 60°$), r slightly agrees with the theoretical predictions. This is the only region in which experimental measurements on micrometric beads [32, 34] were available before the present work. For larger contact angles ($60° < \theta < 120°$) r remains roughly constant around $r \sim 1.1 - 1.2$, but lower than the previous one: this trend disagrees with the expected theoretical values, that are instead rapidly increasing with the contact angle. Finally, for the most hydrophobic particles ($\theta > 120°$) the ratio r decreases below the unity. The diffusion of a bead that is 3/4 in air is slower than the diffusion in water. Compared with the expected theoretical values, the measured value is 400% lower.

Available models [27, 28, 29] (see par. 1.4.1) predict instead that the movement at the interface is less viscous than in water, in agreement with common intuition. They all fail in catching the Brownian dynamics at the interface. For the sake of comparison, the few data available in literature (see par. 1.4.2) are also plotted (cross points in fig. 2.12). Except for the millimetric beads, the other two points [32, 34] agree with our measurements and the corresponding diffusion coefficients are overestimated by theories. A new theoretical paradigm will be necessary to explain our experiment and it will be treated in next chapters.

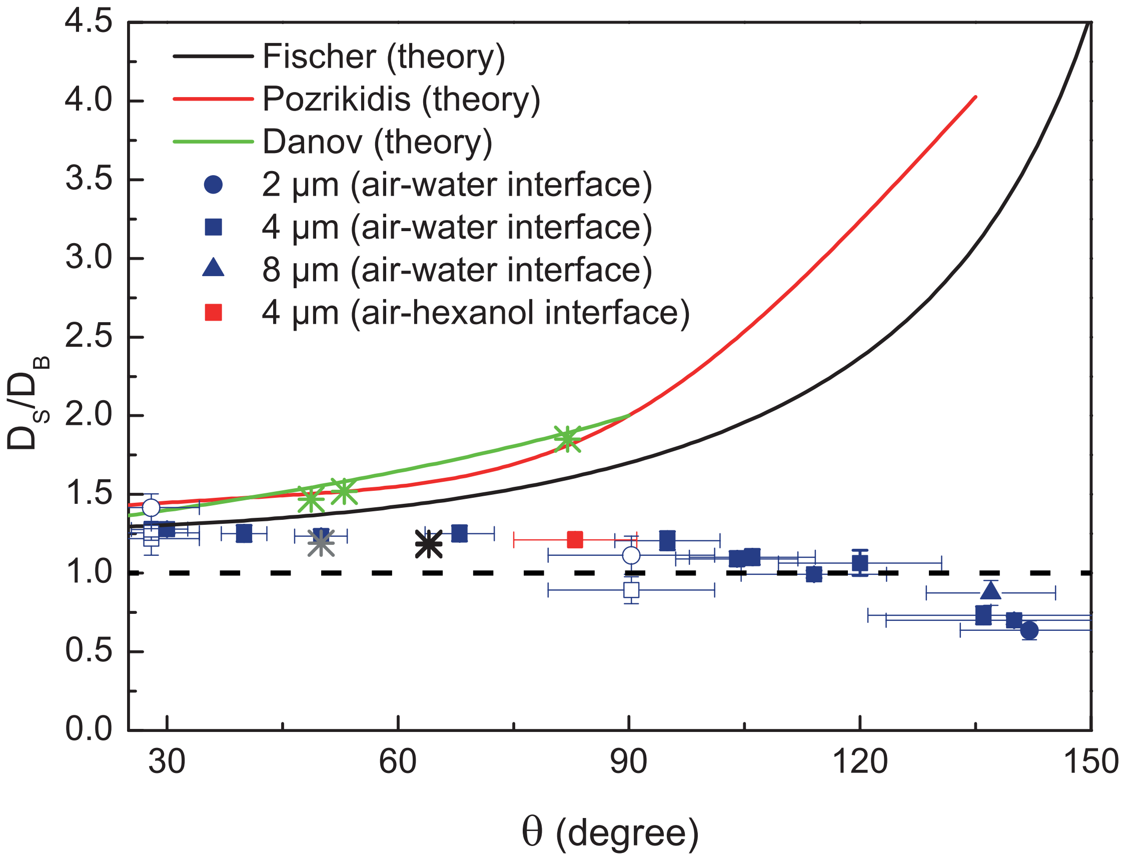

Figure 2.12: D_S/D_V versus contact angle θ for particles with diameter 2μm (circle), 4μm (square) and 8μm (square). Open points corresponds to couples of beads sharing the same interface. Red point is the averaged values for silica beads at an air–hexanol interface. Also reported predictions from existing hydrodynamics theories: Danov et al. [27] (green line), Pozrikidis [28] (red line), Fischer et al. [29] (black line). Cross points are measurements from previous works: Petkov et al. [30], millimetric beads (green), Sickert et al. [32] (gray), Chen and Tong [34] (black).

2.4 Conclusions

In this chapter we report a full characterization of the diffusion of micrometric spherical particles straddled at an air–water interface as a function of their contact angle. The latter is related to the immersion depth in water and it was tuned by chemical treatment of the silica surface of the bead, using hydrophobic silane agents. The effect of the surface treatment was checked by the gel trapping technique [44] on few sample particles, and the contact angle was measured by in situ interferometry for all beads. The diffusion coefficients at the interface were measured in a wide range of contact angles (30° − 150°) by using particle tracking methods [46]. Counter-intuitively, and against hydrodynamics predictions [27, 28, 29], particles diffuse more rapidly when they are more immersed in water. The diffusion coefficient slightly decreases with the contact angle, whilst a strong increase is instead attended. Hydrophobic particles, with their larger part in air, exhibit a diffusion coefficient even lower than the one predicted for fully immersed particles. To explain this intriguing behavior, a new theoretical approach to the problem will be discussed in the following chapters.

Solo dopo aver conosciuto la superficie delle cose, ci si può spingere a cercare quel che c'è sotto. Ma la superficie delle cose è inesauribile.

Only after knowing the surface of things, one can go to seek what is underneath. But the surface of things is inexhaustible.

Italo Calvino

Chapter 3

Measurement of the diffusion of spheroidal colloids at an air–water interface

Introduction

Most of the studies performed until now on colloidal dynamics, both in volume and at the interface, mainly focused on spherical beads because of their ideal shape. However, the real colloidal morphologies that we can find in nature and in common industrial or biological applications have more complex morphologies. A first step toward this direction is provided by considering the simplest case of anisotropy, given by prolate spheroidal particle. The dynamics of such colloids trapped at a fluid interface is studied in this chapter. The particles are obtained from commercial polystyrene spheres, stretched with different elongations to obtain a wide range of aspect ratio (par. 3.1). The particles are then sprayed on the air-water interface (par. 3.2). The induced deformation of the contact line (par. 3.3) and the immersion depth in water (par. 3.4) are measured via interferometric techniques. Finally, the translational and the rotational diffusion coefficients are measured as a function of the aspect ratio by particle tracking (par. 3.5).

3.1 Preparation of the particles

A prolate spheroid is a geometrical object in the three-dimensional space, whose equation in a Cartesian coordinates system is

$$\frac{x^2}{a^2} + \frac{y^2}{b^2} + \frac{z^2}{b^2} = 1 \tag{3.1}$$

where a and b are the long and the short principal axis respectively. In order to achieve the spheroidal shape, commercial spherical beads are stretched by a homemade apparatus [47]. We use amidine and sulfate latex spheres, purchased from Invitrogen (product code A37325 and S37500 respectively), with a radius $r_0 = 0.975\mu$m. They are sold in water solution at a concentration of 4%w/v. Few drops (15-20) are initially dispersed in 40 ml of Poly(vinyl alcohol) (PVA) in deionized water ($10\% - 90\%$). The PVA is purchased from Sigma Aldrich (product code 363081) and deionized water is produced by a Millipore Milli-Q filtration system, with a resistivity of 18 MΩ·cm. PVA and DI water are mixed by several cycles of shaking at 300 rpm and heating at $90 - 100$°C (1/2 - 1h for each operation), until a homogenous phase is obtained. The solution is finally filtrated by using a hydrophobic filter PTFE (pores dimension: 5μm) to remove impurities before adding the beads. The 40 ml PVA-water solution, including the beads, is slowly poured in a Petri dish (diameter: 100 mm) which, before the use, has been carefully cleaned with sulfochromic acid and distilled water. Great attention is paid to avoid the formation of air bubbles that can affect the stretching procedure in an uncontrolled way. By evaporation in 1-2 days on a flat surface, we get a thin film of PVA (thickness ~ 0.2 mm) containing the spherical particles. Strips are cut from the dried film, with special regard to the central region that must be extremely regular; otherwise, a non-homogeneous stretching can distort the final shape of the colloids. The strips are clamped into a metal frame, heated in oven above the temperature of glass transition of polystyrene ($T_g = 100°C$) and then stretched. The stretching of both the strip and the particles included inside is achieved by displacing the upper part of the metal frame by a tension-controlled screw, with a displacing rate of 12 mm/min. In this way, the spherical beads undergo an affine transformation and a spheroidal shape is achieved (fig. 3.1a). The strips are finally soaked in deionized water and PVA is removed by at least 5 cycles of centrifugation (4000 rpm for 10-15 min), replacing the supernatant with Millipore water at the end of each cycle. At the end, the spheroids are re-dispersed in deionized water with the aid of an ultrasonic bath. A SEM picture of typical particles obtained after such a procedure is shown in fig. 3.1b.

We can denote with Λ the elongation imposed at both the strip and the particles. It is defined as the ratio between the final and the initial length of the strip (fig. 3.1a): $\Lambda = l/l_0$. It follows that, along the stretching direction, a long axis is obtained: $a = \Lambda r_0$. Since the total volume of the particle remains constant, i.e. $ab^2 = r_0^3$, the two short axes, in the perpendicular plane, are $b = r_0/\sqrt{\Lambda}$. We can quantify the degree of anisotropy of each particle using the aspect ratio $\phi = a/b$. Sets of particle with the same initial size, and so the same volume, but different elongation are prepared and used in our experiences. The range for ϕ can vary from 1 (unstretched spherical beads) to about 10, that is the upper limit imposed

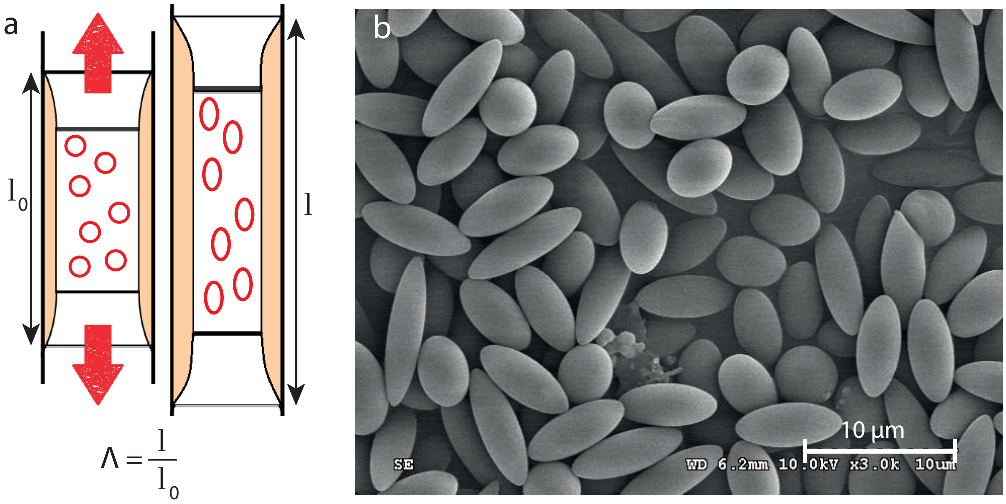

Figure 3.1: **a.** Sketch of a PVA strip, containing spherical beads. The initial length of the strip is l_0. A stretching of the strip along the vertical axis is imposed; the new length is then l. We define an elongation parameter $\Lambda = l/l_0$. The same elongation is imposed also to the particles, which now show a spheroidal shape. **b.** SEM (Scanning Electron Microscopy) image of the spheroidal particles obtained by the technique described in par. 3.1 (Courtesy C. Blanc).

by the stretching method.

3.2 Experimental set-up

A wide container is used to work in a flat interface, at the center of of the sample and avoid the coupling with the curved interface (see appendix A.2). The cuvette is shown in fig. 3.2.

We use a 60 mm diameter Petri dish. Since the sample will be covered during the particle tracking experiences, the air-water interface has to be as close as possible to the glass coverture at the top of the sample. Otherwise, due to limited working distance of the optical objective (7 mm), the focal plane cannot reach the interface and the particle will be out of focus. However small quantities of liquid are required, in order to reduce any convective flows in the sample. Thus, a thick piece of glass is added in the Petri dish to fulfill these two conditions. A piano-convex spherical lens is used for this purpose; it measures 58 mm in diameter and 8.2 mm in height at its center. Note that the lens has just a geometrical role to achieve the optimum working distance and water depth. No optical effects are needed here and deformations or aberrations of the image due to the presence of the lens are negligible. A metal ring with a sharp profile is also added in the gap between the lens and the wall of the Petri dish. In fact, where an air-water-glass

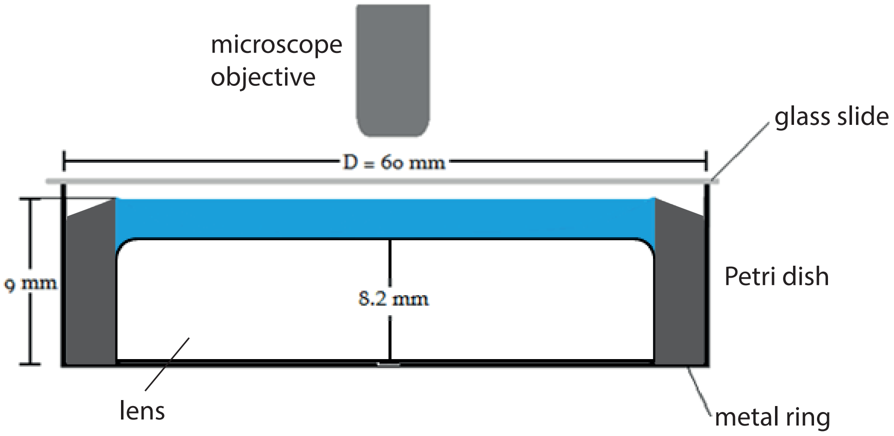

Figure 3.2: Sketch of the cuvette used for the study of spheroidal particles. The container is a Petri dish, 60 mm in diameter, covered by a glass slide to avoid surface contaminations. A thick glass piece (as a lens) is added to minimize the quantity of water involved in the experiment. Such a lens measures 58 mm in diameter and 8.2 mm in height. A metal ring encloses the lens; it has a sharp profile that pins the air-water interface. The deionized water is poured into the sample up to the internal edge of the ring (height: 9 mm). These features assure a 0.8 mm water layer, as close as possible to the microscope objective.

contact line is present on the container walls, non-controlled fluctuations of the surface occur, due to random detachment of the line. The metal ring prevents such detachments and pins the interface at its edge. Moreover, the pinning at such a sharp profile allows an exceptionally large contact angle hysteresis. A 90° contact angle is so permitted, drastically reducing the interface deformation. Deionized water is poured into the sample up to the internal edge of the ring until a flat surface is achieved. A 0.8 mm water layer is thus obtained as close as possible to the microscope objective.

The particles, dispersed in water, are sprayed on the interface by an airbrush, to avoid any possible surface contaminations. Very dilute surface concentrations (less than 0.01% s/s) are used to rule out any possible interaction between colloids. The air-water surface tension is directly measured by Wilhelmy plate method at a free interface, with and without particles. Both the measurements are in agreement with the literature value of the air-water surface tension ($\sigma_{LV} = 0.072$ N/m).

3.3 Interface deformation induced by spheroidal particles

The interface deformation induced by the non–spherical particle (see par. 1.3.1) is measured by using PSI. In particular, an estimation of the amplitude A_2 (see eq. 3.5 in the following) of such a deformation is required to understand its role in particle dynamics. A measurement for a spheroidal particle with aspect ratio $\phi = 2.7$ is here reported.

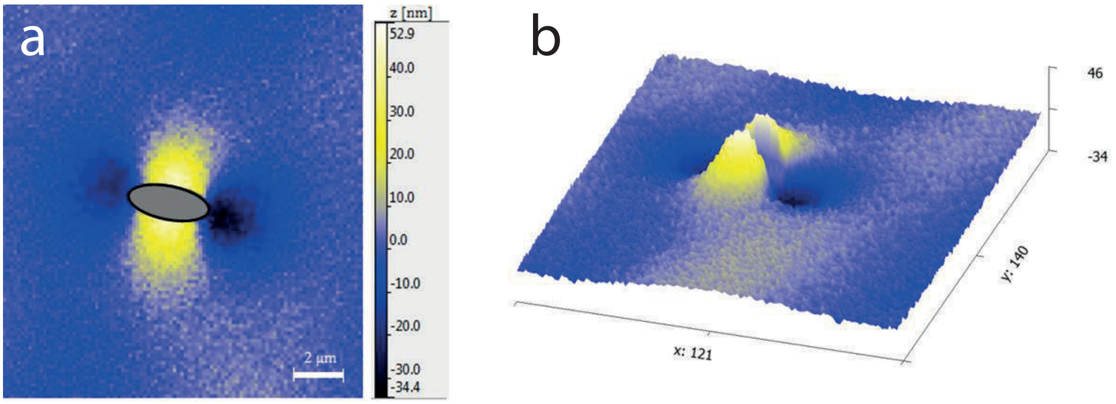

Figure 3.3: **a.** False color image of the interface around a spheroidal particle with aspect ratio $\phi = 2.7$. To achieve a constant macroscopic contact angle around a particle with a non–constant curvature radius, the interface needs to be higher at the center of the spheroid (yellow zone) and lower at the tips (dark blue zone). The difference between the heights of these two zones is around 80 nm. **b.** 3-D reconstruction (vertical scale does not correspond to the one in the horizontal plane) of the interface for the same sample, recovered from the data in **a**.

The parameters of the measurement are the same as the one reported in par. 2.2.2. The Mirau interferometry objective is vertically displaced over 633 nm (wavelength of the involved light beam) in 20 steps. For each step, 15 images are taken (acquisition rate of the CCD camera: 30 frame/s) and their average image is used. At a given pixel, the sinusoidal behavior of the detected intensity is recovered. The phase shift $\Delta\phi$ provides the vertical position h of the corresponding point at the interface:

$$\Delta\phi = \frac{4\pi h}{\lambda} \tag{3.2}$$

The results are shown in a false color image (fig. 3.3a) and in a 3-D reconstruction of the interface (the colloid is removed because it is out of scale) (fig. 3.3b). The maximum deviation from the flat interface (at the tips and in the middle of the particle) is of the order of 40 nm, when the vertical extension of the particle is $2b = 1.3\mu$m.

This relatively weak deformation will be an essential ingredient to guide the model developed in chapters 4 and 5.

3.4 In situ measurement of the contact angle

Vertical Scanning Interferometry is used to provide an estimation of the immersion depth of the particles.

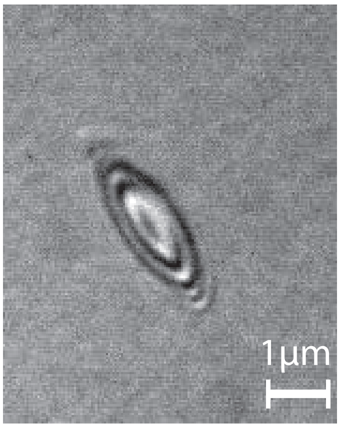

Figure 3.4: Interferometric image of a spheroidal particle at the air-water interface, obtained via VSI technique. Elliptical interference fringes, due to the curvature at the top of the particle, are visible. A series of such images, taken at different objective positions, provides the profile of the particle at the air-water interface.

Interferometric images of the particle at the interface are taken (see an example in fig. 3.4) via VSI and the topography is reconstructed. We can notice an elliptic interference pattern in correspondence of the particle, due to its three-dimensional profile.

As a consequence of the geometry of a spheroidal particle and of the deformed interface [40] (par. 1.6), the computation of the exact value of θ is more complicated. Here we report a method to achieve a good approximation of the contact angle. First of all, let us consider a 2-D elliptic coordinates system (s, t) (fig. 3.5) for the horizontal plane of the interface. The coordinate s has the same role as a radial coordinate in a polar system and t is the elliptic angular coordinate. They are related to a Cartesian coordinate system (x, y) by the relations:

$$x = c \cosh s \cos t \qquad y = c \sinh s \sin t \tag{3.3}$$

where $\pm c$ is the position of the two foci.

Oettel [48] provided an expansion for the vertical displacement of the interface u in the variables (s, t):

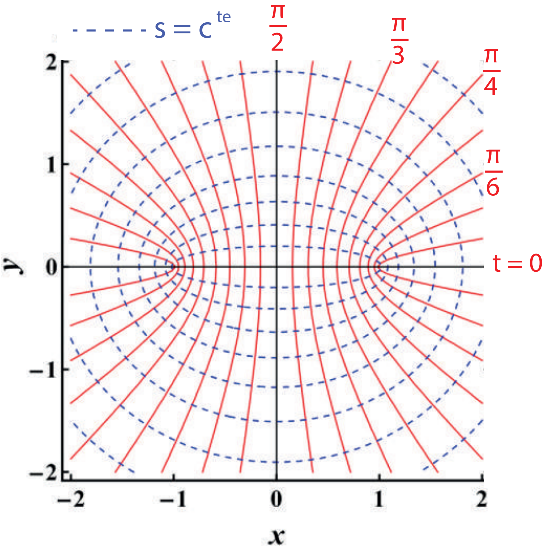

Figure 3.5: Elliptic coordinates system (s,t), as defined in eq. 3.3. The coordinate s has the same role played by a radial distance in polar coordinates system. Each confocal ellipse in dashed blue line is obtained for a constant value of s. Hyperbolas in solid red line are obtained for a given value of the elliptic angular coordinate t.

$$u(s,t) = A_0 \frac{s}{s_0} + \sum_{m>0} e^{-m(s-s_0)} \left[A_m \cos(mt) + B_m \sin(mt)\right] \tag{3.4}$$

where A_m and B_m are elliptic multipole moments of order m and $s = s_0$ is the ellipse on the surface of the particle.

Some conditions are known or imposed to the solution:

1. far from the particle, the interface is unperturbed and stays at a reference height: for $s \to \infty$, $u(s,t) \to 0$;

2. from Loudet [40] and direct PSI measurements (par. 3.3), we know that $u(s,t)$ has minima at the tips of the particle ($t = 0, \pi$) and maxima at its middle ($t = \pi/2, 3\pi/2$);

3. as reported in [48], the quadrupole ($m = 2$) is the leading multipole.

These conditions allow to rewrite eq. 3.4, leading to a simpler approximation for the interface profile:

$$u(s,t) = -A_2 \cos(2t) e^{-2(s-s_0)} \tag{3.5}$$

with $A_2 > 0$.

The derivative of eq. 3.5 in $s = s_0$ gives the slope of the interface at each point of the contact line. For our calculation, we are interested in regions of the contact line where the interface is flat, i.e.:

$$\left.\frac{\partial u}{\partial s}\right|_{s=s_0} = 0 \tag{3.6}$$

This condition is obtained at the angular positions $t = \frac{\pi}{4}, \frac{3\pi}{4}, \frac{5\pi}{4}, \frac{7\pi}{4}$ (red hyperbolas in fig. 3.6a).
A $\tilde{x}$-axis, that intersects the ellipse in two of these points ($t = \frac{\pi}{4}$, $t = \frac{5\pi}{4}$), is introduced (solid green line in fig. 3.6a). The plane $(\tilde{x}, z)$ is now considered (fig. 3.6b).

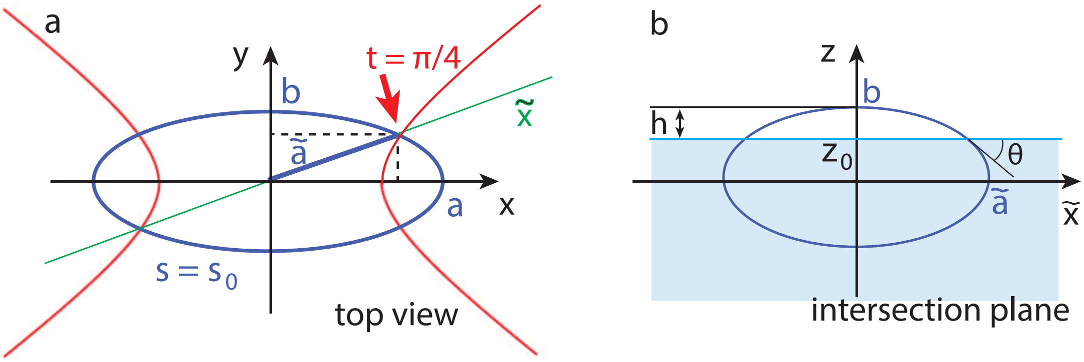

Figure 3.6: **a.** Top view of a spheroid (a, b, b) at the air-water interface. The contact line results in an ellipse of axis (a, b) in a Cartesian coordinates system, or in $s = s_0$ in an elliptic coordinates system. For our purpose, we are interested in the angular coordinate $t = \pi/4$ (red hyperbola). A $\tilde{x}$-axis, passing for $(0, 0)$ and $(s_0, \pi/4)$, is defined (green line). We denote with $\tilde{a}$ the distance between such points. **b.** Intersection of the spheroid with the plane $(\tilde{x}, z)$: the result is an ellipse of axes $(\tilde{a}, b)$. Because of eq. 3.6, the air-water interface is flat in this intersection; the contact angle θ is thus recovered from the tangent at the ellipse. We also denote with z_0 the height of the interface with respect to the center of the particle and with $h = b - z_0$.

The frontal view in such an intersection plane provides the ellipse with axes $(\widetilde{a}, b)$, where $\widetilde{a} = \sqrt{(a^2 + b^2)/2}$ (fig. 3.6b). The contact line passes in the points $(\pm\widetilde{x_0}, z_0)$ of the ellipse, where $z_0 = b - h$ and h is measured via VSI. The condition of a flat interface at these points (solutions of eq. 3.6) allows to recover θ from the slope of the tangent at the ellipse. From trigonometric arguments, θ is the supplementary angle of such a slope, i.e. $\theta = \pi - \arctan m$, where m denotes the angular coefficient of the tangent. It follows that $\tan\theta = -m$. In our case, with the $(\widetilde{x}, z)$ variables and at the point z_0, we have:

$$\tan\theta = \frac{b^2 \widetilde{x}_0}{\widetilde{a}^2 z_0} \tag{3.7}$$

ϕ	$\theta[^\circ]$
1	52.4 ± 3.4
2.7 ± 0.3	48.4 ± 10.6
7.9 ± 0.7	37.7 ± 5.1

Table 3.1: Contact angle θ, measured via VSI technique, at three characteristic aspect ratios, ranging from sphere to elongated particle. In agreement with previous measurements in literature [40, 41], a slight decrease of θ, around 15°, is observed.

Substituting the expressions of z_0, $\widetilde{x_0}$ and $\tilde{a}$ as a function of the initial parameters in eq. 3.7, we finally have

$$\tan\theta = \sqrt{\frac{2}{\phi^2+1}}\frac{\sqrt{2bh-h^2}}{b-h} \tag{3.8}$$

The error on the determination of the contact angle is given by:

$$\Delta\theta = \left|\frac{\partial\theta}{\partial b}\right|\Delta b + \left|\frac{\partial\theta}{\partial\phi}\right|\Delta\phi + \left|\frac{\partial\theta}{\partial h}\right|\Delta h \tag{3.9}$$

The leading term in eq. 3.9 is given by the error on the particle size, $\Delta b = 60$ nm. An enhanced resolution of the VSI measurement, reducing Δh, will not significantly affect the uncertainty of θ. For this reason, the chosen resolution $\Delta h \sim 20$ nm is sufficient.

As shown in par. 1.6, the contact angle slightly depends on the aspect ratio [40, 41]. In table 3.1 we measure by VSI the contact angle for the spheroids in our system as a function of the aspect ratio. In the range from 1 to 8 of aspect ratio, the contact angle variation is moderated in the range $37^\circ - 52^\circ$. Differently from the methods of Loudet [41], our technique univocally determines the contact angle, since the relative position of the top of the particle, with respect to the interface, is detected. Our measurements are in agreement with one set of values proposed in [41]: we recover the lower branch of data (fig. 1.17 in chapter 1), with a decreasing θ in almost the same range.

3.5 Dynamics of the particle

3.5.1 Particle tracking

Particle tracking for ellipsoidal particles is similar to the one presented for spherical beads in par. 2.3 (see appendix A.1). Digital videos are recorded by a firewire charge-coupled device (CCD) camera at 30 frame/s over a region of $120 \times 90\mu\text{m}^2$

(1024×768 px^2). The images are processed by an IDL software in order to have a non-null intensity at the particle and $I = 0$ in the background. The coordinates of the center-of-mass positions in the lab frame at a given times are recovered as the average $(\overline{x}, \overline{y})$ of the position coordinates of every pixels, weighted by their corresponding intensities:

$$\overline{x} = \frac{\sum xI(x,y)}{\sum I(x,y)} \qquad \overline{y} = \frac{\sum yI(x,y)}{\sum I(x,y)} \tag{3.10}$$

as done in par 2.3 for spherical beads. The trajectories are numerically corrected in order to remove the drift contribution, using the same technique described in par. 2.3.2 for spheres. Drift velocities are around 0.1μm/s and are not related to the aspect ratio ϕ of the spheroid. The displacements $\Delta x = x - \langle x \rangle$ and $\Delta y = y - \langle y \rangle$, where $\langle x \rangle$ and $\langle y \rangle$ are the mean positions averaged in time, are considered. Two typical Δx-Δy trajectories for spheroids with different aspect ratio ϕ are reported in fig. 3.7a, 3.7b, measured during the same time interval $\Delta t = 55$s. Different spheroidal shapes are able to affect the interfacial particle dynamics: the most elongated particles diffuse less than the ones with a lower aspect ratio.

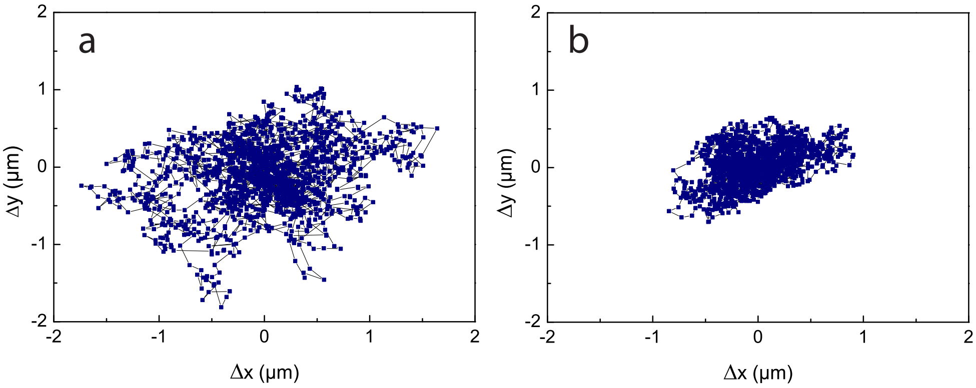

Figure 3.7: Δx-Δy trajectories recorded during the same time interval $\Delta t = 55$ s of two spheroids with different aspect ratios: $\phi = 1.4$ (**a**) and $\phi = 8.7$ (**b**).

In addition, in the case of anisotropic particle, we are also interested in information about the orientation of the colloid and the rotational dynamics. For this purpose the angle φ between the main axis of the ellipsoids and the x-axis of the lab frame (fig. 3.8) needs to be measured.

The technique used is the bisection method (fig. 3.9).

Let us shift the lab frame so that the origin corresponds to the center of mass of the particle, whose coordinates were obtained in the previous step. This new frame is called $(\tilde{x}, \tilde{y})$. First of all, the IDL software counts the number of non-null

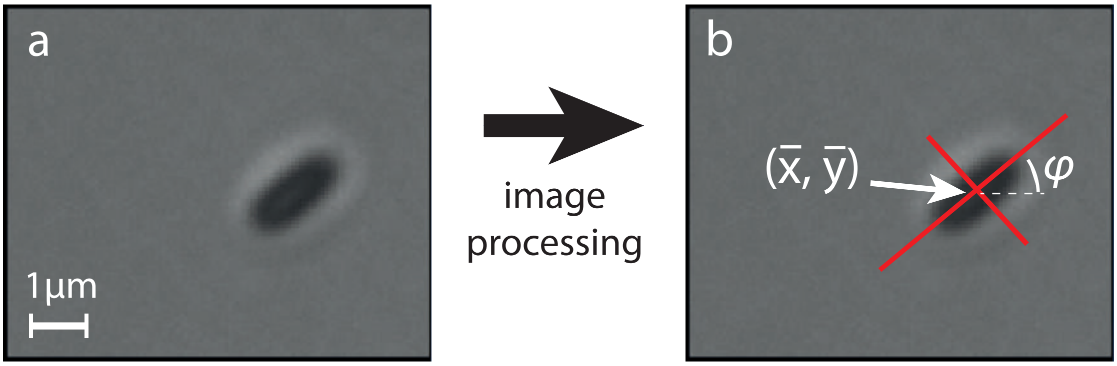

Figure 3.8: **a.** Typical image for a frame of a spheroidal particle at the air–water interface, recorded by a CCD camera. The particle looks like a black spot over a grey background. **b.** After image processing, the intensity center of mass is found: (x̄, ȳ). This coordinate corresponds to the position of the center of the particle. The main axes are also recovered, in order to get rotational dynamics. We denote with φ the angle between the long main axis and the horizontal one.

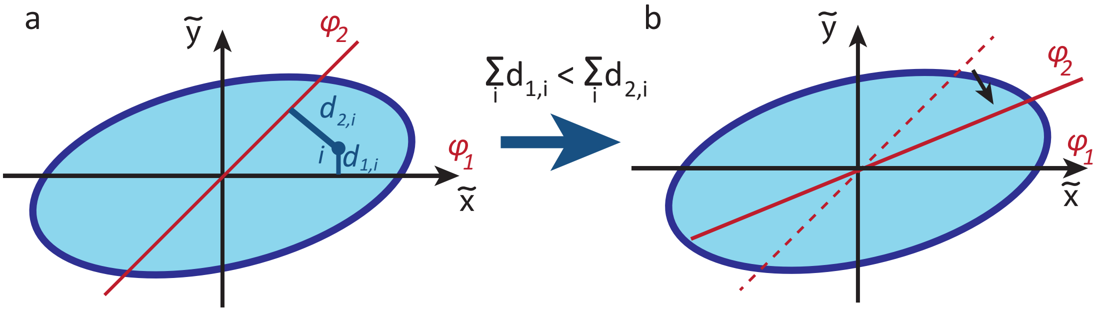

Figure 3.9: Scheme of bisection method. **a.** The orientation φ of the long main axis is in the range $[\varphi_1, \varphi_2]$. In the reported case, $\varphi_1 = 0$ (horizontal axis) and $\varphi_2 = \pi/4$ (red line axis). For a generic point i in the ellipse, the distances $d_{1,i}$ from axis φ_1, and $d_{2,i}$ from axis φ_2 are calculated (solid blue segments). The summation over all the points i of the ellipse are compared: $d_1 = \sum_i d_{1,i} < d_2 = \sum_i d_{2,i}$. **b.** Since the ellipse is *closer* to the axis φ_1, the upper limit φ_2 is replaced by the midpoint value $(\varphi_1 + \varphi_2)/2$.

intensity points, corresponding to the image of the projected ellipse, in the first ($\tilde{x} > 0, \tilde{y} > 0$) and in the second quadrant ($\tilde{x} < 0, \tilde{y} > 0$). The result gives a preliminary information about the range in which the angle φ is: $[0, \pi/2]$ if most of the points are in the first quadrant, $[\pi/2, \pi]$ if most of the points are in the second one. In any case, such a range can be written in the form $[\varphi_1, \varphi_2]$. For each point i of the projected ellipse in the image, the distance $d_{1,i}$ ($d_{2,i}$) from the axis φ_1 (φ_2) is calculated. We consider now the sum of all the calculated distances, with respect to the axis φ_1: $d_1 = \sum_i d_{1,i}$; and to the axis φ_2: $d_2 = \sum_i d_{2,i}$. In this way we can get an average distance of the ellipse from each axis. If $d_1 < d_2$, we can state that the ellipse is *closer* to the axis φ_1. From a more rigorous point of view, this means that the angle φ is in the lower half of the proposed range $[\varphi_1, \varphi_2]$. Otherwise, if $d_1 > d_2$, φ is in the upper half of $[\varphi_1, \varphi_2]$. This statement allows to repeat the same procedure in a smaller, halved range, where the farthest extreme is replaced by the midpoint value $(\varphi_1 + \varphi_2)/2$. The iteration continues until the width of the range is of the order of 2 degrees, that is considered an acceptable resolution for φ.

3.5.2 Statistical analysis of the translational dynamics

The trajectory of the center of mass is used to study the translational dynamics of the particle. Contrary to isotropic systems, the motion of spheroidal colloids in 3-D depends also on the chosen direction: the diffusion along the long axis is different from the diffusion along the short one, as predicted by modified Stokes-Einstein equation [36] and experimentally verified in the volume [5]. We expect the same behavior also for particles straddled at the interface. For this reason, both the positions and the displacements are here referred to a local coordinates system (x_a, x_b) where x_a denotes the direction of the long axis and x_b the one of the short axis (fig. 3.10). The local frame is re-defined at each time $t_n = n(1/30)$ s according to the new orientation $\varphi(t_n)$ of the particle. Note that the frame $(x_{a,n}, x_{b,n})$ is simply obtained by rotating (x_n, y_n) of an angle $\varphi(t_n)$.

We can calculate the displacement over a time lag τ_i:

$$[\Delta x_{a,i}(t_n), \Delta x_{b,i}(t_n)] = [x_a(t_n + \tau_i) - x_a(t_n), x_b(t_n + \tau_i) - x_b(t_n)] \tag{3.11}$$

$\Delta x_{a,i}(t_n)$ and $\Delta x_{b,i}(t_n)$ are normally distributed and their average over all the possible displacements $\langle \Delta x_{a,i} \rangle_n = \langle \Delta x_{b,i} \rangle_n = 0$, as expected from a random walk (fig. 3.11).

The width of the Gaussian curve is related to the diffusion coefficient in the corresponding direction and to the considered time lag τ_i. In this case, the standard deviations $\sigma_{a,i}$ and $\sigma_{b,i}$ write as:

$$\sigma_{a,i} = \sqrt{2 D_a \tau_i} \qquad \sigma_{b,i} = \sqrt{2 D_b \tau_i} \tag{3.12}$$

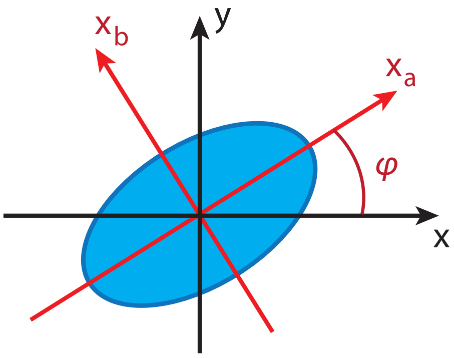

Figure 3.10: Local coordinates system (x_a, x_b), where the axes have the same orientation as the main axes of the ellipsoid. The indexes a, b denote the long and the short axis, respectively. The (x_a, x_b) system is obtained by rotating the lab frame (x, y) by the angle φ, around the center of the particle. A new local coordinates system is defined at each frame, since the position of the particle center and its orientation change in time.

D_a and D_b are translational diffusion coefficients along the long and short axes respectively. For a small aspect ratio ($\phi = 1.4$, fig. 3.11a, 3.11c) the displacements in the two directions a and b have almost the same distribution, due to the weak anisotropy. For more elongated particles ($\phi = 8.7$, fig. 3.11b, 3.11d) distributions differ in width, with a wider distribution for the movement along the long axis, pointing out a faster diffusion along such an axis.

The terms $\sigma_{a,i}$ and $\sigma_{b,i}$, and the corresponding diffusion coefficients D_a and D_b, can be also computed via the analysis of the Mean Square Displacements (MSDs):

$$\begin{aligned}\sigma_{a,i} &= \langle \Delta x_{a,i}^2 \rangle_n = 2D_a\tau_i \\ \sigma_{b,i} &= \langle \Delta x_{b,i}^2 \rangle_n = 2D_b\tau_i \end{aligned} \tag{3.13}$$

Such quantities are calculated for different time lag τ_i in order to plot the curves $\langle \Delta x_a^2 \rangle$ vs. τ, $\langle \Delta x_b^2 \rangle$ vs. τ. Both of them are reported in fig. 3.12 for 4 particles covering all the accessible aspect ratios.

The linear behavior for all the curves denotes a diffusive regime. The analysis of the slopes at different aspect ratios confirms our previous observations: a slower diffusion for more elongated particle, in particular along the short axis b (fig. 3.13).

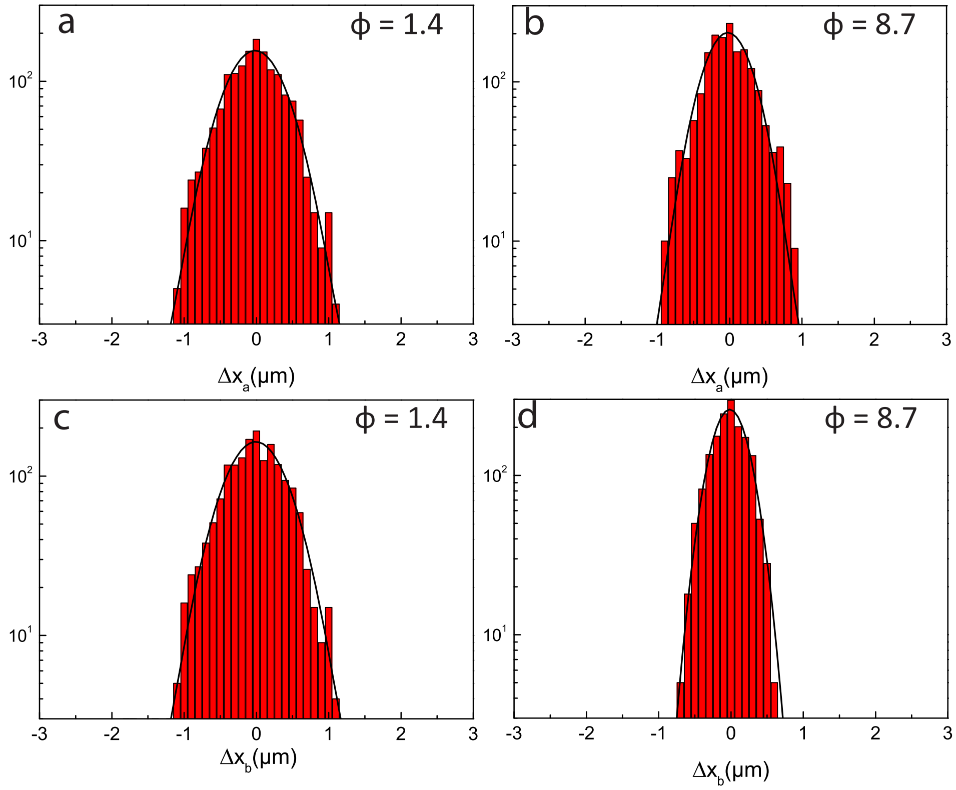

Figure 3.11: Distribution of the displacement Δx_a, Δx_b at time lag $\tau = 1/30$ s, in a semi-log scale, for spheroidal particles. The shapes of all the four graphs confirm the Gaussian distribution of the displacements. Such displacements are recovered from the two trajectories previously shown in fig. 3.7, considering the same time interval $\Delta t = 55$ s. The spheroids have aspect ratio $\phi = 1.4$ (**a.** Δx_a, **c.** Δx_b) and $\phi = 8.7$ (**b.** Δx_a, **d.** Δx_b). The widths of the distributions in the two directions a and b are really close for the small aspect ratio (**a** and **c**). At large aspect ratio (**b** and **d**), the distributions clearly differ in width, with a wider distribution for the movement along the long axis, and the anisotropy of the motion is evident. The distribution widths are smaller at high ϕ than at low ϕ.

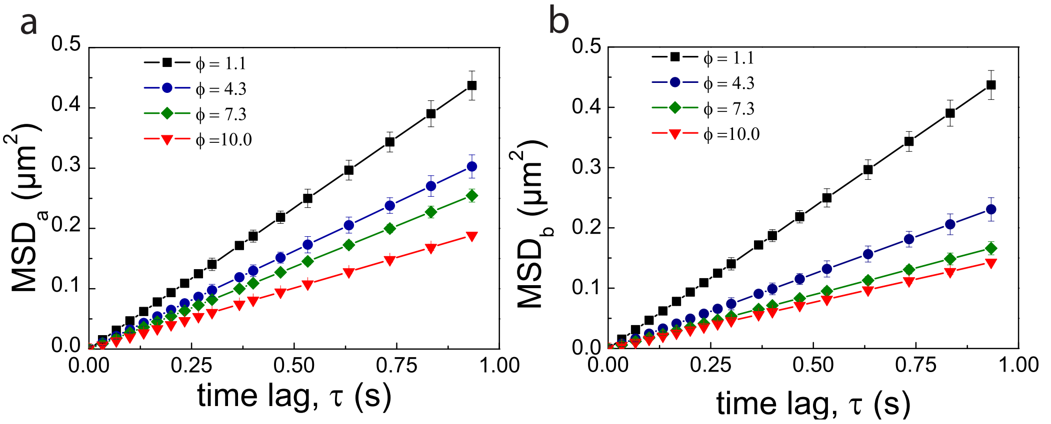

Figure 3.12: MSD as a function of the time lag τ for spheroids at different aspect ratios ($\phi = 1.1, 4.3, 7.3, 10.0$). The translational dynamics in both the main directions is considered: $\langle \Delta x_a^2 \rangle$ (**a**) and $\langle \Delta x_b^2 \rangle$ (**b**). The linear behavior denotes the diffusive regime. The slope of each curve corresponds to $2D$, where D is the translational diffusion coefficient in the corresponding direction and at a given aspect ratio. A decreasing of the slope, i.e. a slower dynamics, is observed for more elongated particles.

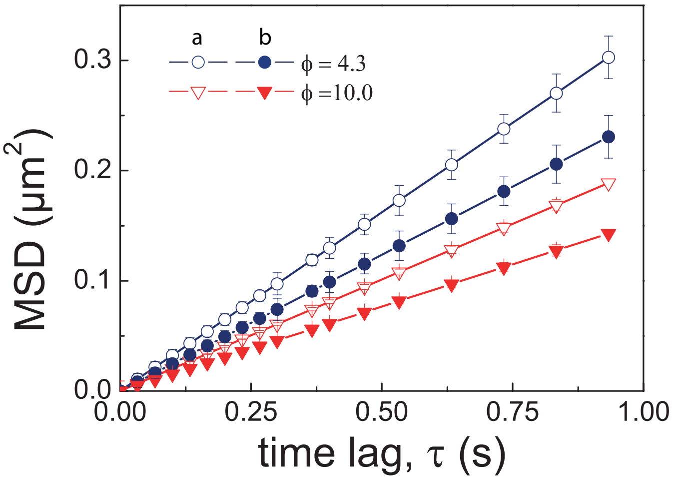

Figure 3.13: MSD as a function of the time lag τ, along long axis (open points) and short axis (full points), for spheroids at $\phi = 4.3$ and $\phi = 10.0$. A slower diffusion is always measured with respect to the short axis.

3.5.3 Statistical analysis of the rotational dynamics

The same theoretical background can be applied also to a statistical analysis of the evolution of φ in time. The angular displacement during τ_i is defined:

$$\Delta\varphi_i(t_n) = \varphi(t_n + \tau_i) - \varphi(t_n) \tag{3.14}$$

Also in this case, the random origin of the dynamics translate in a Gaussian distribution of the angular variation $\Delta\varphi$, centered in $\langle \Delta\varphi \rangle = 0$, and with a width related the rotational diffusion coefficient D_φ (fig. 3.14):

$$\sigma_{\varphi,i} = \sqrt{2D_\varphi \tau_i} \tag{3.15}$$

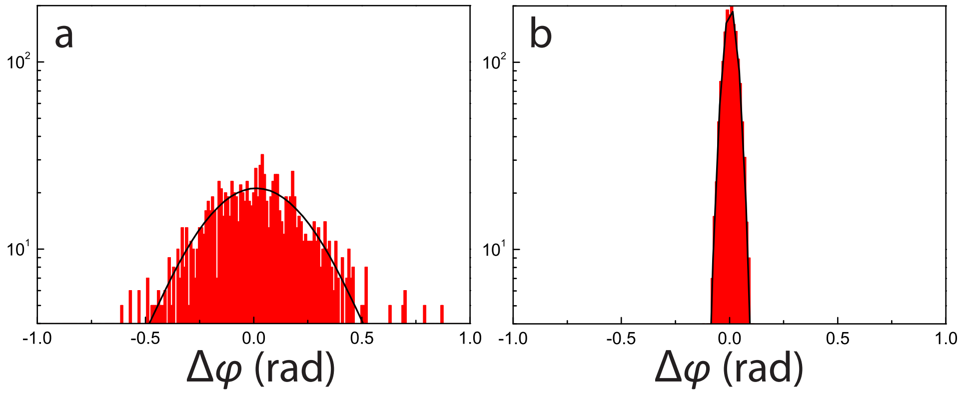

Figure 3.14: Distribution of the angular variation $\Delta\varphi$ over a time interval $\Delta t = 55$ s, at time lag $\tau = 2/30$ s, in a semi-log scale. We consider two spheroidal particles with aspect ratio $\phi = 1.4$ (**a**) and $\phi = 8.7$ (**b**). Both distributions are Gaussian and the one at lower aspect ratio shows a larger width with respect to more elongated colloids, revealing a huge difference in the rotational diffusion coefficients.

The rotational MSDs, calculated at 4 different aspect ratios, are plotted in fig. 3.15.

The rotational diffusion coefficient is calculated by the typical expression:

$$\langle \Delta\varphi^2 \rangle = 2D_\varphi \tau \tag{3.16}$$

Since a strong variation of the rotational dynamics as a function of the aspect ratio is observed, a log-log plot of the MSD is proposed. In this case, we have

$$\log\langle \Delta\varphi^2 \rangle = \log 2D_\varphi + \log \tau \tag{3.17}$$

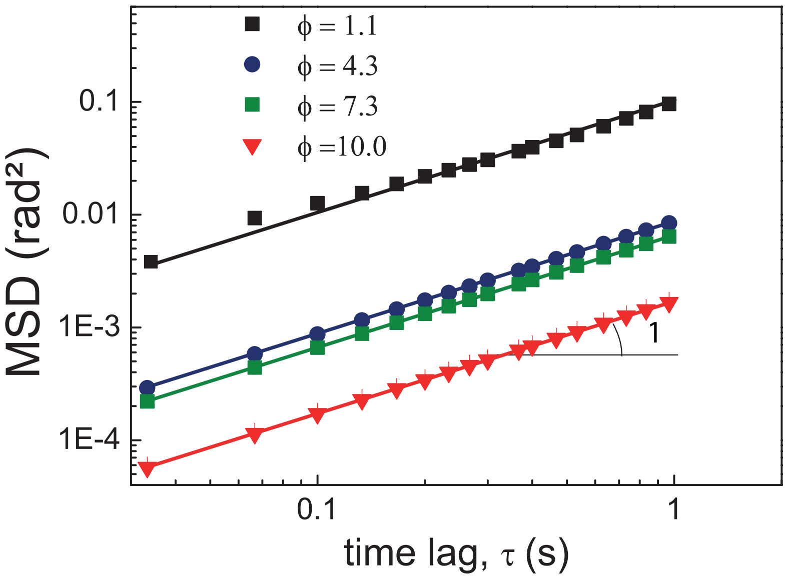

Figure 3.15: Angular MSDs vs. the time lag τ in a log-log scale. Spheroids with different aspect ratios ($\phi = 1.1, 4.3, 7.3, 10.0$) are considered. All the curves show a constant slope, equal to 1: this characteristic denotes a linear behavior of the MSD, corresponding to a diffusive regime. The intercepts at $\tau = 1$ is proportional to $\log D_\varphi$. We observe that the rotational diffusion coefficient strongly decreases, over few orders of magnitude, with the aspect ratio ϕ.

A slope equal to 1 corresponds to the linear behavior, due to the diffusive regime. No variation of the slope is recovered in this system, excluding here the presence of an angular confinement. At $\tau = 1$, $\log\langle\Delta\varphi^2\rangle = \log 2D_\varphi$. From fig. 3.15, we observe a strong decrease, over few orders of magnitude, of the rotational diffusion, with the aspect ratio ϕ.

3.5.4 Translational diffusion coefficients vs. aspect ratio

The dynamics for spheroidal particles are observed in a wide range of aspect ratio, $1 < \phi < 10$. The value $\phi = 1$ corresponds to spherical beads, and $\phi = 10$ is the maximum aspect ratio achievable with our stretching method. Other parameters, such as the material, the volume or the immersion depth, remain constants and they are equal to the ones for an unstretched commercial bead. Translational diffusion coefficients along the local axes are shown in fig. 3.16 (long axis) and in fig. 3.17 (short axis).

Each point in the curves corresponds to the average values on 3 to 6 different particles with the same elongation. For the sake of comparison, the theoretical estimation for the same colloid, but totally immersed in the volume (water), is also reported (continuous lines in figs. 3.16, 3.17). These curves are calculated from Stokes-Einstein equation, modified by the geometric factors G_a and G_b, to

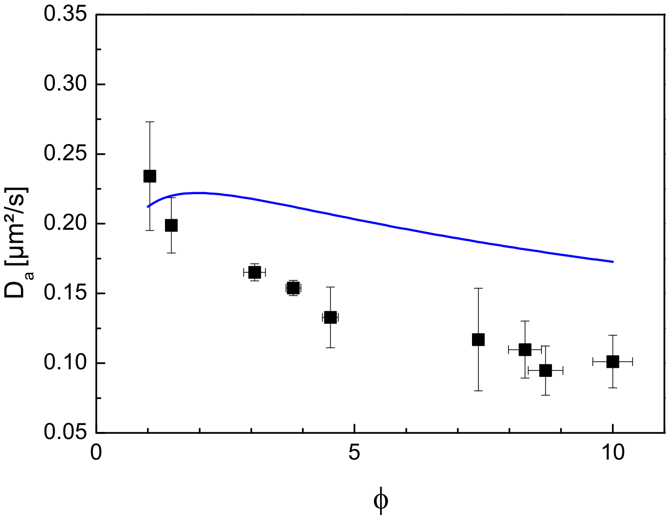

Figure 3.16: Translational diffusion coefficient D_a vs. aspect ratio ϕ. Points for each ϕ are direct measurements of the diffusion coefficients along the long axis, averaged on the values on 3 to 6 particles. Error bars correspond to the standard deviation on the average. At $\phi \sim 1$ we recover the same translational diffusion coefficient measured for a partially immersed bead (see chapter 2). Then, the diffusion coefficient decreases; the most elongated spheroid ($\phi = 10$) diffuses almost 2 times slower than the spherical-like particle. For the sake of clarity, the experimental data are compared with the theoretical estimation for same particles, but totally immersed in water (solid line). The diffusion at the interface is slower than in the bulk, when common intuition suggests the opposite behavior.

take into account the effect of the anisotropic shape [36] (see par. 1.5.1 for a detailed discussion):

$$\begin{aligned} D_{a,V} &= \frac{k_B T}{6\pi\eta_W G_a(\phi) b} \\ D_{b,V} &= \frac{k_B T}{6\pi\eta_W G_b(\phi) b} \end{aligned} \tag{3.18}$$

with η_W viscosity of the water. At $\phi = 1$, $D_{a,V} = D_{b,V}$ and we recover the same expression as for spherical beads. When the aspect ratio increases, a slight decreasing of both the translational diffusion coefficients is predicted, except for $D_{a,V}$ in a small region around $\phi = 1.3$, where a maximum appears. The reason of the presence of the maximum is that the range of ϕ is explored at constant initial volume. In this case, both the geometric factor G_a and the spheroid short axis b which enter in the definition of the diffusion coefficient depend on ϕ. Predictions about the dynamics of spheroids at the interface are not available, but common intuition suggests a faster diffusion than in the bulk. As in the case of spheres,

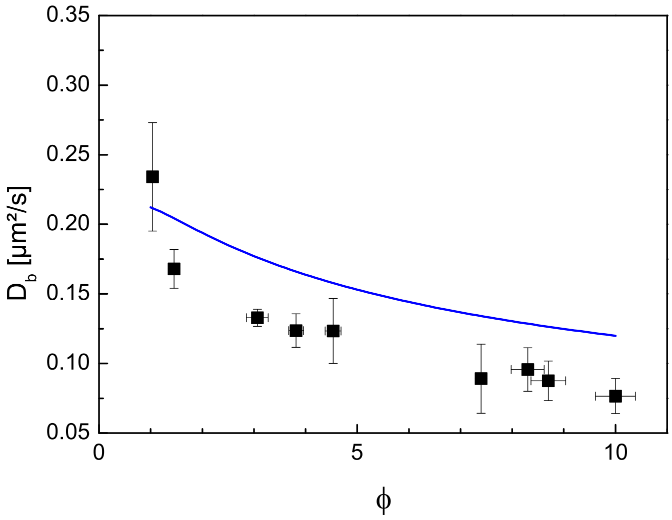

Figure 3.17: Translational diffusion coefficient D_b vs. aspect ratio ϕ. Points for each ϕ are direct measurements of the diffusion coefficients along the short axis, averaged on the values on 3 to 6 particles. Error bars correspond to the standard deviation on the average. The data are compared with the theoretical estimation for the particles totally immersed in water (solid line). The diffusion coefficient D_b shows the same behavior reported for D_a (see fig. 3.16).

experimental data are in disagreement with this picture. In fact, for small aspect ratio ($\phi \simeq 1$), i.e. for spherical-like particles, we recover the same behavior measured for spheres (see chapter 2) at similar contact angle $\theta \simeq 50°$: the diffusion coefficient at the interface is slightly larger than in the bulk. Moreover, $D_a = D_b$ since long and short axes cannot be distinguished (fig. 3.18). For increasing aspect ratios, both the translational diffusion coefficients decrease more rapidly than in the bulk: at $\phi \simeq 10$ the interfacial diffusion is 2 times slower than the corresponding one in the bulk. In any case, $D_a/D_b > 1$, i.e. the dynamics is always faster along the long axis a, and the anisotropy of the motion increases with the anisotropy of the particle (fig. 3.18). However, such a ratio varies more slowly when the colloid is straddled at the interface.

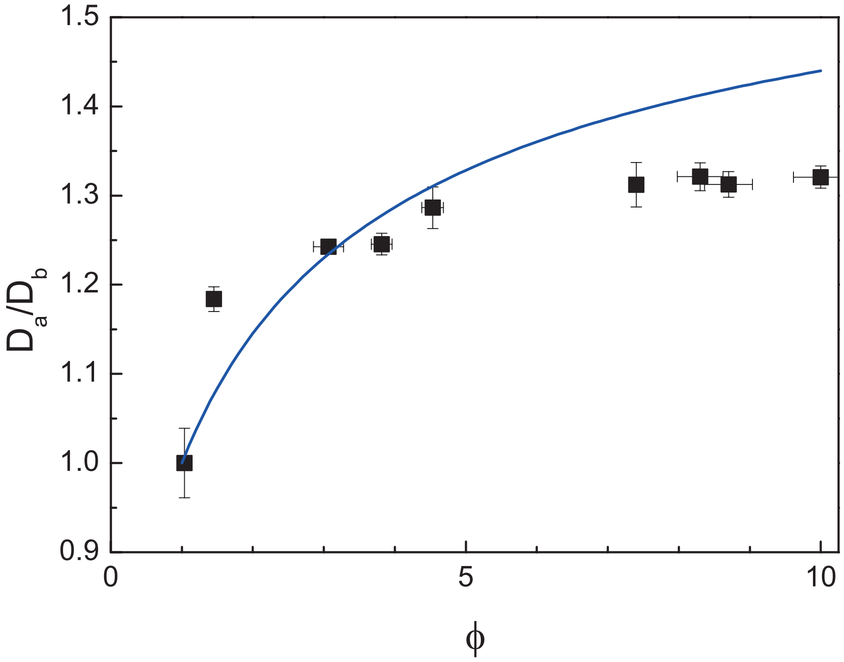

Figure 3.18: Ratio D_a/D_b, showing the anisotropy of the translational diffusion, measured at the interface (points) and predicted in the bulk (continuous line). The values are reported as a function of the aspect ratio ϕ of spheroidal particles. In both the case, $D_a/D_b > 1$, i.e. the dynamics is always faster along the long axis a, and the anisotropy of the motion increases with the anisotropy of the particle. However, such a ratio varies more slowly when the colloid is straddled at the interface.

3.5.5 Rotational diffusion coefficient vs. aspect ratio

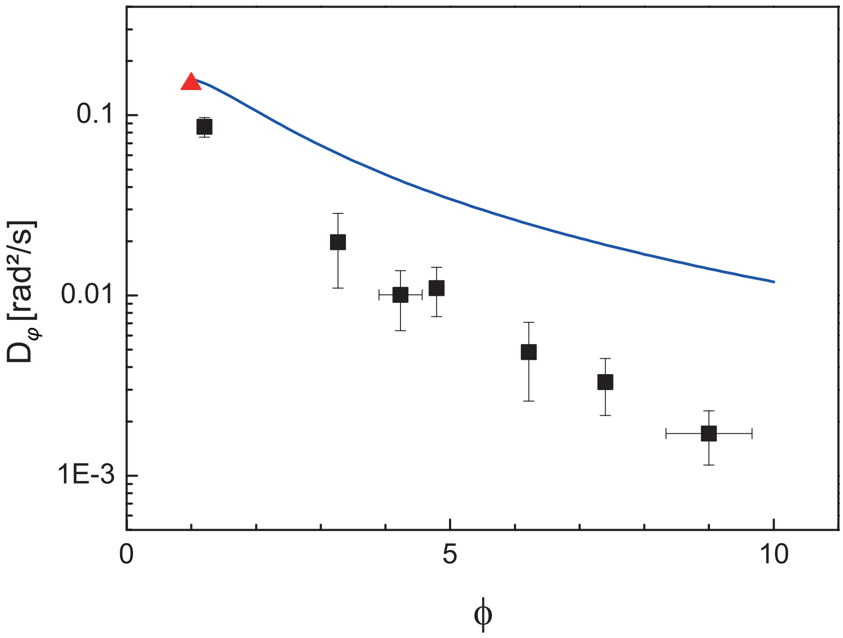

Figure 3.19: Rotational diffusion coefficient D_φ vs. aspect ratio ϕ in semi-log scale. Points are direct measurements of the rotational diffusion coefficient, averaged on the values on 3 to 6 particles. Error bars are the standard deviation of the average. At $\phi \simeq 1$ the trend of the curve recovers the value for the optically anisotropic Janus particle (red point). When the aspect ratio increases, the rotational diffusion coefficient varies over 2 decades. This behavior differs from the one predicted when the particle is immersed in water (solid line).

The measured rotational diffusion at the interface (black points in fig. 3.19) is analyzed with respect to the aspect ratio ϕ. Each point at a given ϕ corresponds to the average on 3 to 6 values. The diffusion coefficient rapidly decreases with the aspect ratio and varies over 2 order of magnitude in the range $\phi = 1 \div 10$. Measurements at $\phi \simeq 1$ have been performed with optically anisotropic spheres (Janus particles), in which the orientation is easily recognized. The obtained diffusion coefficient (red point in fig. 3.19) does not differ significantly from the rotational diffusion in the volume. As in the previous case, the rotational diffusion in the volume is plotted as a reference (solid line in fig. 3.19). Such a value, as a function of ϕ, writes [36]:

$$D_{\varphi,V} = \frac{k_B T}{6\eta_W G_\varphi(\phi) V} \tag{3.19}$$

where $G_\varphi(\phi)$ is the geometric factor and V is the volume of the particle. A decreasing diffusion coefficient, introduced by the geometric factor $G_\varphi(\phi)$, is expected also in the bulk, but it is much weaker than the one we measure at the interface. We recover again the counter–intuitive results of a slower dynamics at the interface, despite the effect of the partial immersion; the diffusion is one order of magnitude slower than the one in the bulk. As previously presented (par. 1.6 and 3.4), the immersion depth of a spheroids changes with the aspect ratio: more elongated particles result more immersed in water. One can ask if such effect will be responsible of the measured increase of the drag. However, the slight variation of the contact angle (less than 15°) and the viscosity ratio of the two fluid phases ($\eta_{water}/\eta_{air} \simeq 50$) are incompatible with the huge difference (around 70 times) between the first and the last points in the accessible range of aspect ratio. A different approach to the problem has to be used.

A theoretical model able to explain these observations is needed and it will be devised in the next chapters.

3.6 Conclusions

The full characterization of the diffusion of spherical particles at an air–water fluid interface, proposed in chapter 2, was here extended to prolate spheroidal colloids. The tunable parameter was not yet the immersion depth in water (that remained almost constant in all the measurements), but the degree of anisotropy, expressed by the aspect ratio ϕ. Translational and rotational diffusion coefficients at the interface were measured in the range $1 \div 10$ of ϕ. Lower diffusion coefficients were found for more elongated particles, in qualitatively agreement with what is expected in the bulk. However, the dynamics is always slower at the interface than in bulk, as in the case of spherical beads. The translational diffusion coefficients at the interface are two times smaller than in the volume, and rotational diffusion coefficient, especially at high aspect ratios, is measured to be one order of magnitude slower than in the bulk. This dynamical slowing–down is reminiscent of the one measured for beads, pointing out that such behaviors would share the same physical mechanism. In order to capture it, we propose in the following chapters a new theoretical approach to the problem.

Il buon senso c'era; ma se ne stava nascosto, per paura del senso comune.

Wisdom was there. But it was hidden, scared by common intuition.

Alessandro Manzoni, Promessi Sposi, cap. XXXII

Chapter 4

Explanation of slowed-down diffusion: fluctuation of the contact line

Introduction

The results reported in the previous chapters show that, for both spherical and prolate spheroidal particles, a pure hydrodynamics approach accounting the effect of partial immersion of a particle in water is not sufficient to catch their dynamics at a fluid interface. All the theories [27, 28, 29] underestimate the measured viscous drag exerted on the particle: both spheres with different immersion depths and spheroids with different aspect ratios diffuse more slowly than existing hydrodynamics theories predict. A new paradigm is thus demanded to explain our experimental observations.

Additional sources of dissipation that have been neglected in the theoretical predictions are first considered in this chapter and their contribution is estimated (par. 4.1). However, all this classical hydrodynamic approaches could not explain our measured results. Therefore, we adopt a different point of view. All the existing models consider the contact line in a sort of mean field way, neglecting the effect of its fluctuations. In fact, it is well–known that the line is driven out of equilibrium by thermally activated fluctuations of the air–water interface. Here we investigate the contribution of such fluctuations and their coupling with the lateral movement of the particle. Random forces produced by such fluctuations add to the ones due to the shocks of surrounding molecules (par. 4.2). Fluctuation-dissipation theorem allows to obtain the friction associated to these additional random forces, as at the thermal equilibrium the particle kinetic energy remains fixed by the equipartition theorem to $k_BT/2$ per degree of freedom (par. 4.3). The corresponding contribution to the particle drag is discussed in two opposite limiting cases: in the case of a moving contact line, where the fluctuations are due to molecular jumps (par. 4.4) and in the regime of a pinned line where fluctuations are associated to capillary waves (par. 4.5). Both mechanisms lead to the right order of magnitude for the viscous drag, reproducing the measured particle diffusion and recovering the increasing viscous drag at large contact angles.

4.1 Possible extra dissipation sources

4.1.1 Deformation of the interface

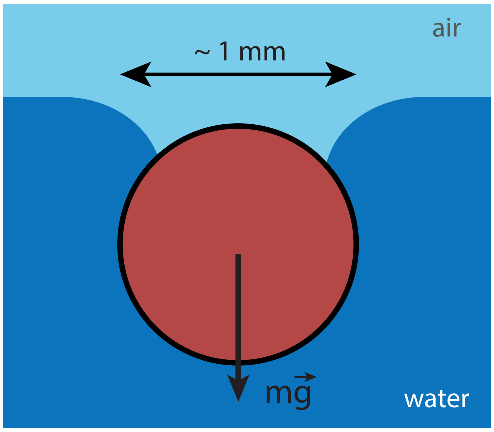

Figure 4.1: Heavy particle (copper bead in the millimetric range) at the air–water interface. Gravity forces, much larger than the interfacial ones, induce a curved meniscus around the particle.

The effect of an interface deformation on the lateral dynamics of a particle at the interface was analyzed by Petkov et al. [30]. In their work they studied the motion of millimetric spherical particles attached to an air–water interface. Their method consisted in the measurement of the particle velocity v under the action of a defined lateral capillary force F. The drag coefficient ζ exerted by the fluid on the particle was then obtained from the ratio $\zeta = F/v$. As we showed in par. 1.4.2, the drag coefficient ζ of glass beads (radius 0.2 mm, density $\rho_g \sim 2.5 \cdot 10^3$ kg/m^3) is in agreement with the numerical predictions. However, when they considered a heavy copper spherical particle (radius 0.52 mm, density $\rho_c = 8.9 \cdot 10^3$ kg/m^3), a strongly slowed–down dynamics was found. At a contact angle $\theta = 78°$, the viscous drag at the interface is 1.75 larger than the one for a particle totally immersed in water. The qualitative solution proposed in [30] considered the role of a large hydrodynamic resistance induced by the curved meniscus around the heavy particle (fig. 4.1a). The curved meniscus has to move together with the particle, leading to the motion of the water in the whole region below the meniscus. The total volume that is displaced during the Brownian motion is thus increased. One can ask if the same effect plays a role in the micrometric particles in our experiments, in order to explain the experimental results in chapters 2 and 3.

Let us start with the case of silica micrometric beads. Our particle are much smaller and lighter (10^3 times smaller in radius, 10^9 times in mass) with respect to the millimetric glass beads used in [30]. Any meniscus–induced additional drag can be definitely discarded.

The case of spheroidal particles is instead different, since the deformation of the interface is induced by the shape of the particle, and not by gravity. A characteristic quadrupolar deformation is observed (see par. 3.3 and fig. 4.2). Note that a typical interfacial profile shows a rise at the center of the particle (yellow zones) and a decrease at the tips (dark blue zones). Such a deformation relaxes at the equilibrium level of water (unperturbed interface far from the colloid) along a distance equal to the radius of curvature of the particle. Due to the anisotropic shape of the spheroid and to the non–constant radius of curvature, the deformation at the middle relaxes at longer distances than the one at the tips. As a result, the whole deformed region can be approximated as an isotropic disk (white dashed line in fig. 4.2). Its radius is on the order of the long axis a, and the height corresponds to the distortion measured via PSI.

If we consider the argument of Petkov, the spheroid has to induce the rotation of the water disk at its same angular velocity. The required additional viscous torque will be proportional to the disk volume, which is rounded up by:

$$V_{disk} \sim \pi a^2 \frac{b}{10} \tag{4.1}$$

In eq. 4.1 we have considered the maximum disk volume, obtained by the spheroid with the highest aspect ratio ($\phi = 10$), in which the maximal distortion is around $0.1b$ (par. 1.6).

With respect to the particle volume, we obtain:

$$\frac{V_{disk}}{V_{spheroid}} \sim \frac{\pi a^2 b/10}{4/3 \pi a b^2} \sim \frac{3}{4}\frac{\phi}{10} \sim \frac{3}{4} \tag{4.2}$$

In the case of maximum deformation of the interface, the proposed overestimation of the displaced volume, in which the presence of air is not taken into account, is comparable with the volume of the particle. A volume more than 10 times larger would be instead required to explain our enhanced rotational drag,

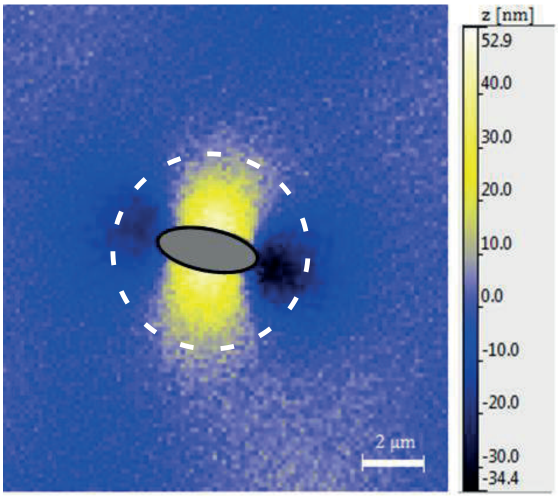

Figure 4.2: False color image of the typical interface deformation around a spheroidal particle. The interface is higher at the center of the spheroid (yellow zone) and lower at the tips (dark blue zone). The deformed region around the particle can be approximated by an isotropic disk (white dashed line).

as found in the experiments (see fig. 3.19). We conclude that particle–induced deformations cannot be used as an argument for the comprehension of the results presented in this thesis.

4.1.2 Wedge flow at the interface

It is easy to see that, when a particle is straddled at the interface, the fluid profile is very close to a wedge. When the particle moves or rotates, such a wedge profile slides on the particle surface. Dussan and Davis [49] probed the motion of the liquid in a region in similar condition (moving fluid on a solid substrate), by marking the upper surface of the wedge with small spots of a dye. They found a very characteristic rolling motion, reminiscent of a caterpillar vehicle, which gives rise to a viscous friction (fig. 4.3).

De Gennes [20] computed the corresponding dissipation per unit length due to such a motion of the contact line. The wedge is treated as a nearly flat film where the velocity v has a Poiseuille profile, given by the boundary conditions: on the solid side ($z = 0$), the velocity vanishes, $v = 0$; on the gas side ($z = \xi(x)$), no tangential stress are present, $\partial v/\partial z = 0$. If we denote with U the average velocity of the wedge, i.e.

$$U = \frac{1}{\xi}\int_0^{\xi} v(z)dz \tag{4.3}$$

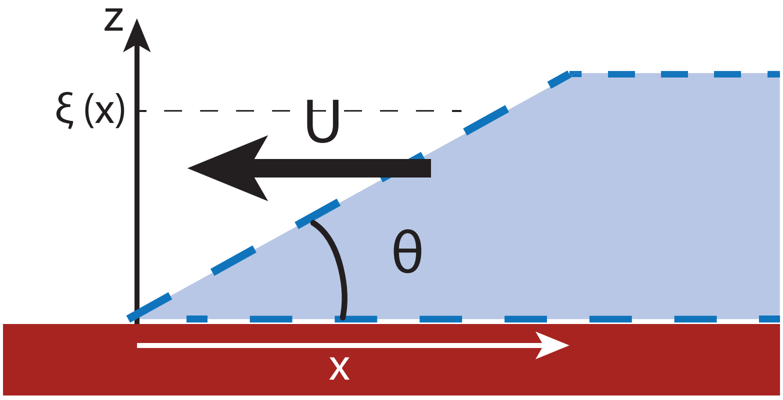

Figure 4.3: Sketch of the motion of a fluid wedge on a solid substrate, according to the picture proposed by Dussan and Davis [49] and by De Gennes [20]. The presence of a contact angle θ between the solid substrate and the fluid gives rise to a fluid wedge. It is moving on the solid substrate at an average velocity U. The wedge shows a characteristic rolling motion, which is responsible of the dissipation.

the velocity profile writes

$$v(z) = \frac{3U}{2\xi^2}\left(-z^2 + 2\xi z\right) \tag{4.4}$$

The total dissipation per unit length of the contact line is recovered by:

$$P_l = \int_{x_{min}}^{x_{max}} \int_0^{\xi(x)} \eta \left(\frac{\partial v}{\partial z}\right)^2 dz dx = \\ \int_{x_{min}}^{x_{max}} \frac{3\eta U^2}{\xi(x)} dx = \frac{3\eta U^2}{\theta} \ln\left|\frac{x_{max}}{x_{min}}\right| \tag{4.5}$$

since $\xi(x) = x\theta$, when θ is sufficiently small; x_{min} and x_{max} are cutoff distances. We will not enter into the details of the discussion, but it is sufficient to note few characteristic dependencies. First of all, the dissipation depends on U^2, and so it is invariant for advancing and receding wedges. Moreover, such a term is directly proportional to the viscosity η of the fluid.

Let move on the case we are interested in: a fluid wedge moving on a spherical bead. The physics is exactly the same as shown for a flat substrate, and so we recover the corresponding dissipation, proportional to the fluid viscosity. For the sake of simplicity, we focus into two cases of hydrophilic and of hydrophobic beads. In the first case (fig. 4.4a), a water wedge is moving on the particle surface. In the second one (fig. 4.4b), at a complementary position of the interface, the dissipation on a hydrophobic bead can be obtained considering an air wedge. A much smaller

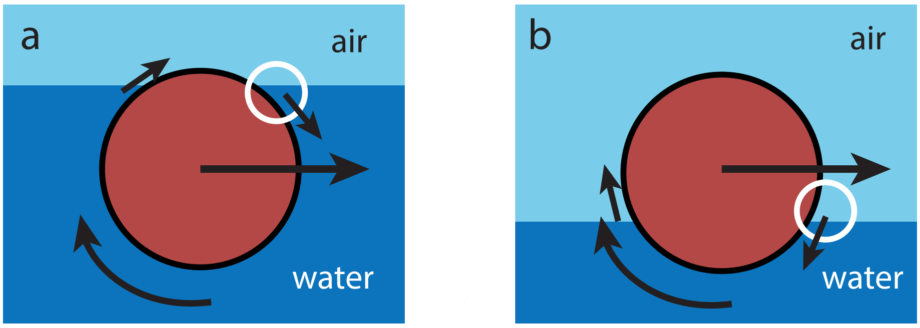

Figure 4.4: A spherical bead at a fluid interface gives rise to a fluid wedge profile at the contact line. For a hydrophilic particle (**a**) a water wedge is obtained. For a hydrophobic bead (**b**) the air-water interface is at the complementary position; an air wedge can be so pictured. Since the wedge dissipation [20] (eq. 4.5) is proportional to the fluid viscosity, a larger effect is attended for hydrophilic bead. This statement is in contradiction with experimental observation.

viscosity ($\eta_{air} \ll \eta_{water}$) is here present, leading to a negligible dissipation. It follows that the dissipation due to the motion of a wedge flow is more relevant for hydrophilic particles, but this result is in contradiction with the experimental data that we want to explain. Consequently, this is not the effect that we are looking for.

Such possible extra dissipation sources fail to reach the measured required additional drag. In the same way, we can show the contact line friction has no role in dynamics (see appendix A.3). The effect of a curved meniscus, accounted for a similar dynamics of heavy millimetric beads, is not suitable for particle in the micrometer range. The wedge hydrodynamic effects fail to reproduce the behavior of the particle diffusion with the immersion depth. The dissipation of a contact line, moving on the solid substrate, does not increase the total drag of the particle. A new theoretical paradigm needs thus to be conceived, as it will be done in the next paragraphs considering the role of fluctuations at the contact line.

4.2 Fluctuating forces at the triple line

Let us consider a top view of a spherical bead; we focus on the contact line and on the interface at its vicinity. A cylindrical coordinate system (r, φ, z) is defined (fig. 4.5). r is the radial distance from the normal z to the interface, centered on the bead. φ is the angular position with respect to an arbitrary axis w over the interface.

A fluctuation i can occur at a random position of the contact line. Let us

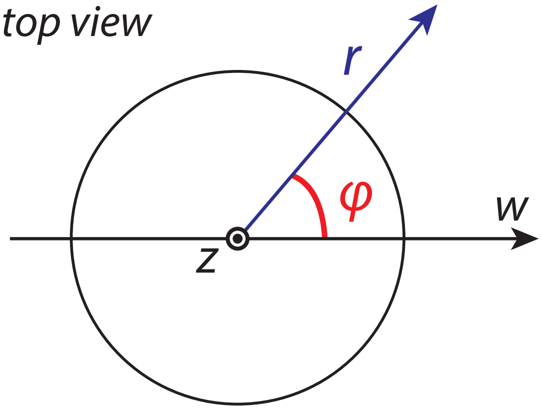

Figure 4.5: Cylindrical coordinate system (r, φ, z), shown in top view of the particle at the interface. The vertical axis z is perpendicular to the interface and centered on the bead. The angle φ is defined with respect to the arbitrary axis w, that lies on the interface. The radial coordinate r is the distance between a generic point and the center of the bead.

consider a line fluctuation having a mean length λ and centered at the angular position φ_i. Two types of fluctuations can be involved:

- in the case of a moving line, a local displacement of the contact line on the particle surface (fig. 4.6a);
- in the case of a pinned line, a local capillary deformation of the interface profile (fig. 4.6b).

Both fluctuations lead to a variation of the slope of the interface at the contact line, and so give rise to an unbalanced lateral force $\sigma_{LV}\lambda(1-\cos\alpha)$. We have denoted with α the average slope of the interface after a fluctuation, defined as the angle between the tangent to the interface at the particle and the horizontal (fig. 4.6) and with σ_{LV} the liquid-vapor surface tension. At nanometric length scales, where hydrodynamics meets molecular approach, it is still physically possible to define such interface slope. With reference to the arbitrary direction w (fig. 4.5) the net force $F_{L,i}$ is written:

$$F_{L,i} = \sigma_{LV}\lambda(1-\cos\alpha)\cos\varphi_i \tag{4.6}$$

In practice, this single line fluctuation translates in an extra random kick to the particle, in addition to the ones provided by molecular collisions. The random force depends on α and λ. They are random variables distributed around an average value. For the sake of simplicity, only the mean value is considered. Let us consider now the effect of a large number of fluctuations on the motion of the bead. Since there are no preferred position along the contact line, the angular position φ_i of a

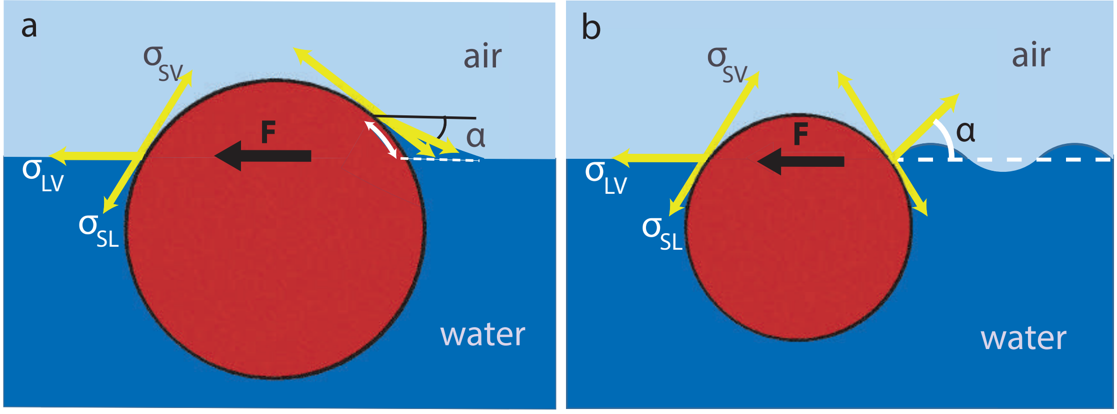

Figure 4.6: Sketch of local fluctuations at the interface: **a.** displacement of a segment of the contact line; **b.** local capillary deformation at a pinned contact line. Both of them lead to a variation of the slope of the interface at the contact line, denoted by the angle α. This effect gives rise to an unbalanced lateral interfacial force F on the bead.

fluctuation is uniformly distributed in the range $[0, 2\pi]$. Considering the length of the contact line $2\pi a_0$, where $a_0 = R \sin\theta$, and λ the average lateral length of each fluctuation, the number of possible fluctuations at a given time is

$$n = 2\pi a_0/\lambda \tag{4.7}$$

Summing over n, we obtain thus the total force:

$$F_L = \sum_{i=0}^{n} F_{L,i} = \sigma_{LV}\lambda(1-\cos\alpha)\sum_{i=0}^{n}\cos\varphi_i \tag{4.8}$$

The random distribution of the fluctuations along the contact line, i.e. of the angular position φ_i of $F_{L,i}$, translates in a null ensemble average $\langle F_L\rangle = 0$ and in

$$\langle F_L^2\rangle = n\langle F_{L,i}^2\rangle = \frac{1}{2}n\left[\sigma_{LV}\lambda(1-\cos\alpha)\right]^2 \tag{4.9}$$

F_L is so a fluctuating force with a null ensemble average and a non-null squared ensemble average. It adds to the other random force usually considered in pure hydrodynamics approaches, due to the collisions between the molecules of the surrounding fluid and the particle itself. To relate this new fluctuating force to the particle viscous dissipation we use the fluctuation-dissipation theorem.

4.3 Particle drag via fluctuation-dissipation theorem

Fluctuation-dissipation theorem allows to associate a general fluctuating force F to a drag ζ [50, 51]:

$$\zeta = \frac{1}{2k_BT}\int_0^{+\infty}\langle F(0)F(t')\rangle dt' \tag{4.10}$$

In practice, the theorem states that if the power injected by the fluctuating force increases, the dissipated power due to friction has also to increase, as the final energy of the particle remains fixed by the equipartition theorem to $k_BT/2$ per degree of freedom. Here we use the expression in eq. 4.10 to recover the total friction exerted on a particle at the interface. In such a case, we have showed that the random force at a given time t comes from two different contributions; it can be so written as:

$$F(t) = F_H(t) + F_L(t) \tag{4.11}$$

where F_H is the hydrodynamic term due to molecular collisions and F_L has been introduced in eq. 4.8 as the random contribution of the contact line.

The term in the integral in eq. 4.10 is so developed:

$$\begin{gathered}\langle F(0)F(t')\rangle = \langle [F_H(0) + F_L(0)]\,[F_H(t') + F_L(t')]\rangle = \\ \langle F_H(0)F_H(t')\rangle + \langle F_H(0)F_L(t')\rangle + \langle F_L(0)F_H(t')\rangle + \langle F_L(0)F_L(t')\rangle\end{gathered} \tag{4.12}$$

Here we assume the uncorrelated nature of the two types of forces, that leads to a null ensemble average for the last two, mixed terms. This hypothesis is corroborated by some considerations. In the case of a moving line, the contact line fluctuations are provided by tangential movements of water molecules, with respect to the particle surface, while F_H comes from normal molecular collisions. In the case of a pinned line, a local capillary deformation of the interface is given by molecules far from the particle, while molecular collisions are at its vicinity.

Substituting the expression 4.12 in eq. 4.10, we note that the two random forces F_H and F_L contributes separately to the total friction ζ. Thus, the friction is expressed in the form:

$$\zeta = \zeta_H + \zeta_L \tag{4.13}$$

where the term ζ_H (ζ_L) depends just on the integral of the force F_H (F_L).

The two terms in eq. 4.13 are now discussed separately.

4.3.1 Calculation of the hydrodynamics drag ζ_H

The first term in eq. 4.13 is defined as

$$\zeta_H = \frac{1}{2k_BT}\int_0^{+\infty}\langle F_H(0)F_H(t')\rangle dt' \tag{4.14}$$

where F_H is the force due to the collision between the molecules of the fluid and the particle. For this reason, F_H has a non-trivial expression and the integral in eq. 4.14 cannot be analytically solved. However, this solution is not necessary since ζ_H has been already calculated otherwise. In fact, from Stokes-Einstein equation (par. 1.2.1) we know that the viscous drag for a particle totally immersed in water is

$$\zeta_V = 6\pi\eta_W R \tag{4.15}$$

where η_W is the viscosity, R is the radius of the particle and the index V stands for the diffusion in volume.

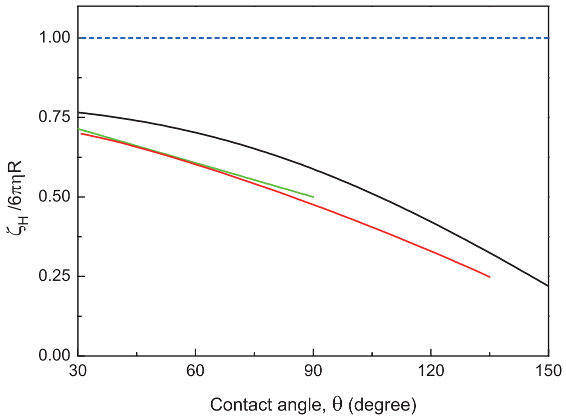

Figure 4.7: Viscous drag ζ_H at the interface, normalized by the corresponding value in the volume ($\zeta_V = 6\pi\eta R$ - dashed line) versus contact angle θ. ζ_H is predicted by existing hydrodynamics theories, under different approximation (see main text for more details): Danov et al. [27] (green line), Pozrikidis [28] (red line), Fischer et al. [29] (black line). They agree from a qualitatively point of view. They follow common intuition: a decreasing drag is expected when the bead is less immersed in water.

At the interface, the effect of a partial immersion is discussed and predicted by hydrodynamic theories using different approximations [27, 28, 29] (see chapter 1, par. 1.4.1). All such theories predict, in agreement with common intuition, a decreasing viscous drag when the particle is less immersed in water (fig. 4.7). Among the available models, we use the one provided by Fischer et al. [29] as it is the only one able to analytically compute the values of ζ_H as a function of the contact angle θ in the whole experimentally accessible range. In [29] ζ_H writes as:

$$\zeta_H = 6\pi\sqrt{\tanh\left[32\left(1+\cos\theta\right)/\left(9\pi^2\right)\right]}\eta R \tag{4.16}$$

4.3.2 Calculation of the contact line contribution ζ_L

The second term in eq. 4.13 is

$$\zeta_L = \frac{1}{2k_B T} \int_0^{+\infty} \langle F_L(0) F_L(t') \rangle dt' \tag{4.17}$$

where F_L is defined in eq. 4.8. Also in this case the random nature of the force makes the analytic solution of eq. 4.17 extremely difficult to obtain. However, the integral can be safely approached by considering the following arguments:

- a new fluctuation at the contact line occurs after an average time τ, characteristic of the considered mechanism;
- each new fluctuation changes the global random force F_L on the particle;
- between two successive fluctuations, i.e. during a time τ, the force F_L remains constant.

In this way, for $t' > \tau$, we can state that the two considered forces at different times $F(0)$ and $F(t')$ are generated by different fluctuations. Since each fluctuation is independent and uncorrelated to the others, this means

$$\langle F(0) F(t') \rangle = 0 \qquad t' > \tau \tag{4.18}$$

A non–null contribution to the integral in 4.17 is provided only when $t' < \tau$, i.e. when $F(0) = F(t')$. Consequently, an approximated form for ζ_L is

$$\zeta_L \simeq \frac{1}{2k_B T} \langle F_L(0)^2 \rangle \tau. \tag{4.19}$$

The term $\langle F_L(0)^2 \rangle$ has been computed in eq. 4.9. Substituting in eq. 4.19, ζ_L is finally written as a function of the parameters α, λ and τ:

$$\zeta_L \simeq \frac{1}{2k_B T} \sigma_{LV}^2 \left(1 - \cos\alpha\right)^2 \lambda \pi R \sin\theta \tau \tag{4.20}$$

This is the expression for the drag contribution due to a generic fluctuation at the interface, characterized by:

- an average slope α of the interface after the fluctuation;
- a typical lateral extension λ of the fluctuation;
- a correlation time τ of the fluctuating force.

No other assumptions are made on these parameters until this point of the discussion. Their physical meaning is here discussed in the two limits: of a moving line using the theoretical background of Molecular Kinetic Theory proposed by Blake [52] (par. 4.4) and of a pinned line taking into account local capillary fluctuations of the interface (par. 4.5). In a general case, both of them do contribute to the additional drag but here, in the interest of clarity, they will be discussed separately.

4.4 Particle drag due to thermal hopping of the contact line

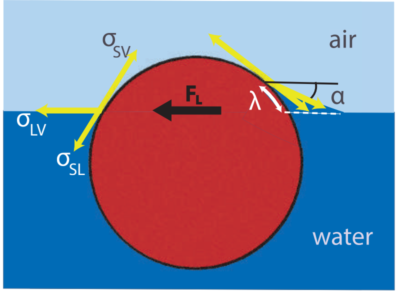

Figure 4.8: Sketch of local fluctuations at the interface in the case of a moving line. The line jumps over a distance λ on the particle substrate, resulting in a variation α of the interface slope at the contact line. Such a deformation gives rise to the random force F_L on the bead.

In Molecular Kinetic Theory (MKT), Blake [52] assumed that the contact line is constantly moving around its equilibrium position because of thermally activated jumps of water molecules between hydrophilic sites of the bead surface. In his work, this hypothesis is then used to derive the displacement of the contact line under the effect of a driving force on the line. On the contrary, in our case no external forces are applied and the contact line stays, in average, at the same position. However, if molecular jumps are present according to MKT, they induce fluctuations of the interface at the vicinity of the triple line, giving rise to the effect described in the previous paragraphs.

4.4.1 Molecular Kinetic Theory

Let us consider now a non-ideal solid substrate, where defects or chemical heterogeneities are present. The contact line can jump between such sites, providing two effects:

- thermal fluctuations of the contact line;
- a solid friction of a moving contact line, due to the pinning energy of the defects.

The first one will be here used in order to describe the dynamics at the interface. A theoretical derivation of such dissipation is here described [23].
The main assumption of Blake model is that the molecules of the fluid phases can jump, because of thermal excitations, between adsorption sites on the solid surface, spaced by a distance λ. In particular, we are interested to the case of adsorbed molecules of a species interchanging with those of the other one, when they are close enough to the contact line. As a consequence, thermally activated fluctuations of the contact line around its equilibrium position appear at a molecular scale (fig. 4.9). The number of molecular jumps, in unit time and in unit length, from water to air can be written as an Arrhenius-like term, by using the absolute reaction rate [53]:

$$\kappa_+ = \frac{k_B T}{h_p} \frac{Z^*}{Z_+} \exp\left(\frac{-\epsilon_+}{k_B T}\right) \tag{4.21}$$

where ϵ_+ is the activation energy for a molecular jump in the considered direction, Z^* and Z_+ are the partition function that take into account the number of the activated and the initial states respectively, h_p is the Planck constant and $k_B T$ the thermal energy. The term $k_B T/h_p$ gives thus the frequency of a thermal photon. In the same way, the jump rate per unit length in the opposite direction (from air to water) is

$$\kappa_- = \frac{k_B T}{h_p} \frac{Z^*}{Z_-} \exp\left(\frac{-\epsilon_-}{k_B T}\right) \tag{4.22}$$

with $\epsilon_+ \neq \epsilon_-$. At the equilibrium, the net jump rate has to be null, so

$$\kappa_+ = \kappa_- = \kappa_0$$

$$\frac{Z_-}{Z_+} = \exp\left(\frac{\epsilon_+ - \epsilon_-}{k_B T}\right) \tag{4.23}$$

The jump rate at the equilibrium κ_0 can be finally expressed in the form:

$$\kappa_0 \simeq \frac{k_B T}{h_p} \exp - \frac{\Delta\epsilon}{k_B T} \tag{4.24}$$

i.e. the frequency of the thermal photon times a Boltzmann factor representing the probability of a molecular jump. ϵ is here used as an effective activation energy.

In presence of an external force (per unit length) f, the jump rate depends on the force orientation. This effect translates in an alteration of the energy barriers,

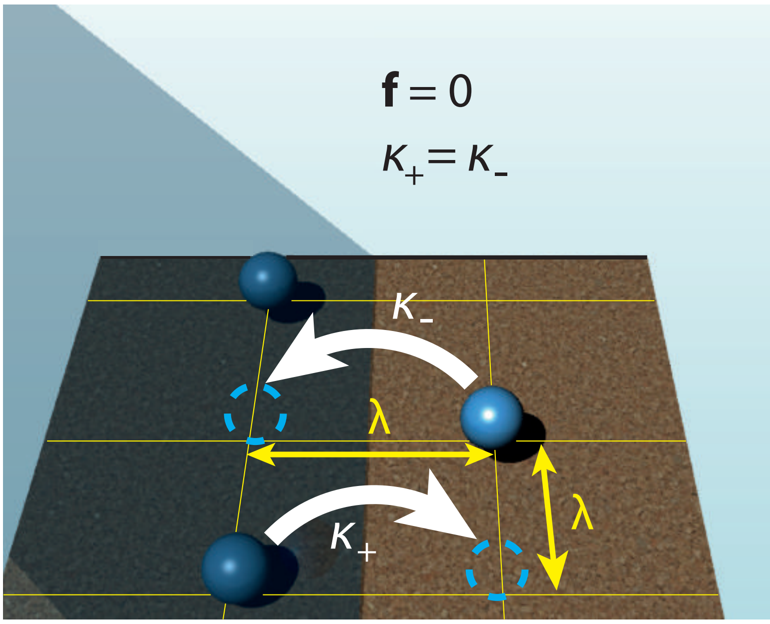

Figure 4.9: Schematic picture of the region around the contact line, in the framework of the Molecular Kinetic Theory. The molecules of the fluid phases (spheres) can jump from one phase to the other, between adsorption sites on the solid substrate. Such sites are spaced by an average distance λ. We denote with κ_+ the number of molecular jump, in unit time and in unit length, from water to air; κ_- is the same term, but in the opposite direction. At the equilibrium, i.e. when no external forces act on the contact line, the net jump rate is null, so $\kappa_+ = \kappa_-$. When the equilibrium is broken, a displacement of the contact line occurs.

lowered in the same orientation of the force and raised in the opposite one. For a single adsorption site of length λ, the work δw done to displace the line to the following site at a distance λ is:

$$\delta w = f\lambda^2 \tag{4.25}$$

The net jump rate is thus

$$\kappa_{net} = \frac{k_B T}{h_p}\left[\frac{Z^*}{Z_+}\exp\left(\frac{\delta w - \epsilon_+}{k_B T}\right) - \frac{Z^*}{Z_-}\exp\left(\frac{-\delta w - \epsilon_-}{k_B T}\right)\right] =$$

$$= \kappa_+ \exp\left(\frac{\delta w}{k_B T}\right) - \kappa_- \exp\left(\frac{-\delta w}{k_B T}\right) \tag{4.26}$$

From eq. 4.23,

$$\kappa_{net} = 2\kappa_0 \sinh\left(\frac{\delta w}{k_B T}\right) \tag{4.27}$$

The velocity of the contact line, given by $v = \lambda\kappa_{net}$, is fully expressed by using eqs. 4.27, 4.25:

$$v = 2\kappa_0\lambda \sinh\left(\frac{f\lambda^2}{k_BT}\right) \tag{4.28}$$

For low values of the argument in the sinh function, the linearization leads to

$$v = \kappa_0\lambda^3\frac{f}{k_BT} \tag{4.29}$$

The velocity v is thus proportional to the applied external force f; a corresponding friction coefficient (per unit length) ζ_0 is so introduced

$$\zeta_0 = \frac{f}{v} = \frac{k_BT}{\kappa_0\lambda^3} \tag{4.30}$$

Such a friction coefficient is a function of the average distance λ between adsorption sites, i.e. it depends on the properties of the solid substrate.
The jump rate κ_0 has been detailed in further developments of theory. Blake [54] proposed to write the activation energy ϵ in eq. 4.24 as the free energy of wetting Δg_W. Δg_W has two contributions, from both surface (Δg_S) and viscous (Δg_V) energy:

$$\Delta g_W = \Delta g_S + \Delta g_V \tag{4.31}$$

According to Eyring theory [55], Δg_V is related to the liquid viscosity η via:

$$\Delta g_V = k_BT \ln\frac{\eta v_m}{h_p} \tag{4.32}$$

v_m is the volume of the unit flow that, in our case, correspond to the molecular volume of the liquid ($v_m = 4 \cdot 10^{-29}$ m^3). Taking $\Delta g_S \sim E_a$, i.e. the energy of adhesion of an element of fluid on the solid substrate (this term will be better defined in a further discussion), the final expression for κ_0 is

$$\kappa_0 \simeq \frac{k_BT}{\eta v_m}\exp -\frac{E_a}{k_BT} \tag{4.33}$$

The characteristic length λ here corresponds to the mean distance between hydrophilic sites on the surface of the particle and it is used as a free parameter. Its value as a function of θ is calculated according to the experimental data. The deformation α imposed to the interface and the correlation time τ of the fluctuations are both dependent on λ and they are discussed in details.

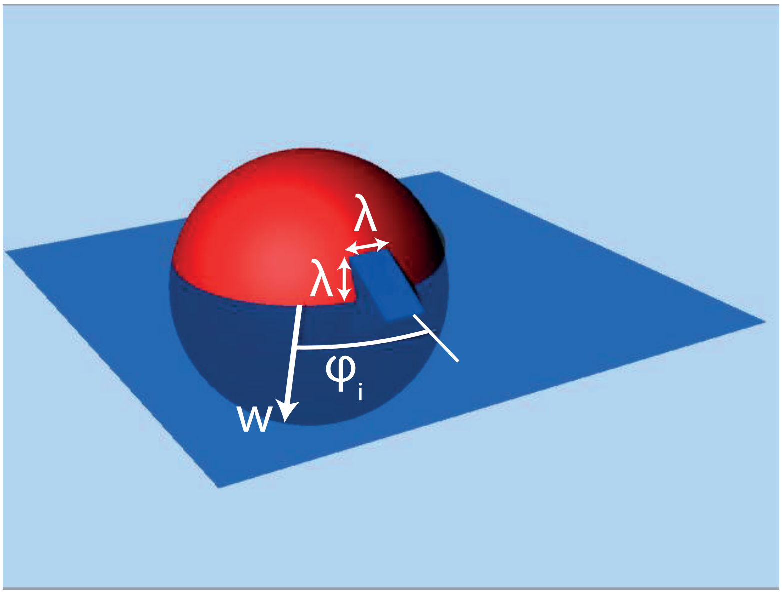

Figure 4.10: Schematic view (not in scale) of the contact line displacement at the interface. A line jump occurs at the angular position φ_i, defined with respect to an arbitrary axis w. For the sake of simplicity, a stepwise fluctuation of the contact line is considered. A segment of length λ is displaced over a length λ on the surface. The jump results in the deformation of the interface at the contact line in the position φ_i.

4.4.2 Interface slope α at the particle

For the sake of simplicity, we assume a stepwise jump (fig. 4.10) of the contact line on the particle with respect to the equilibrium height $z = 0$. In cylindrical coordinates $z = z(r, \varphi)$, the line is displaced along an arc of length λ centered at the arbitrary position φ_i over a distance λ on the particle surface. This displacement on the particle surface induces a deformation of the air-water interface which, in the limit of small deformation of the considered thermal process, obeys the Laplace equation:

$$\frac{\partial^2 z}{\partial r^2} + \frac{1}{r}\frac{\partial z}{\partial r} + \frac{1}{r^2}\frac{\partial^2 z}{\partial \varphi^2} = 0 \tag{4.34}$$

The stepwise deformation of the contact line is developed in eigen–modes and used as a boundary condition for the solution [48] of eq. 4.34:

$$z(r, \varphi) = \frac{u\lambda}{2\pi a_0} \ln\left(\frac{r}{a_0}\right) + \sum_{n=1}^{+\infty} \frac{u}{\pi n} \sin\left(\frac{\lambda n}{2a_0}\right) \cos(n\varphi) \left(\frac{a_0}{r}\right)^n \tag{4.35}$$

where a_0 is the radius of the contact line and $u = \lambda \sin\theta$ is the projection of the displacement on the z-axis. The slope α (see fig. 4.6a) of the interface at the contact line ($r = a_0$) and in the point where the jump occurs (due to the arbitrariness of the choice, we take $\varphi = 0$) is recovered from:

$$\tan\alpha = -\frac{\partial z}{\partial r}\bigg|_{r=a_0,\varphi=0} = -\frac{u\lambda}{2\pi a_0^2} + \frac{u}{\pi a_0}\sum_{n=1}^{+\infty}\sin\left(\frac{\lambda n}{2a_0}\right) = -\frac{\lambda^2\sin\theta}{2\pi a_0^2} + \frac{4\sin\theta}{\pi} \tag{4.36}$$

In the assumption that the displacement λ is much smaller than the size of the contact line, i.e. $\lambda \ll a_0$, eq. 4.36 is simplified

$$\tan\alpha \simeq \frac{4\sin\theta}{\pi} \tag{4.37}$$

This means that $\alpha \sim 0.6 - 0.9$ rad for any contact angle θ in the experimental accessible range $[30°, 140°]$.

The line jump on the bead changes also the projection on the plane $z = 0$ of the other two interfacial forces (per unit length), σ_{SL} and σ_{SV} (fig. 4.11), since they are always tangent at the particle surface. If we denote with the angle β the angular jump with respect to the bead center (fig. 4.11), we have

$$\beta = \frac{\lambda}{R} \ll 1 \tag{4.38}$$

much smaller than α. This variation is negligible and it is not considered in our model.

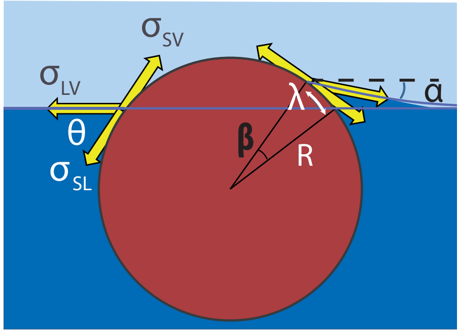

Figure 4.11: Schematic picture (not in scale) of the change of the projection of the two interfacial forces (per unit length) σ_{SL} and σ_{SV} on the equilibrium interface plane. When the line jumps over a distance λ on the bead surface, it describes an angle $\beta = \lambda/R$ with respect to the bead center.

4.4.3 Line hopping characteristic time τ

Since the line jump is a thermally activated mechanism, an Arrhenius-like [56] jump rate κ_0 can be introduced:

$$\kappa_0 \propto \exp -\frac{E_a}{k_B T} \tag{4.39}$$

where E_a is the activation energy necessary to allow the line jump. In a simple picture, Blake suggested modeling E_a as the work needed to detach an area of water from the particle surface at the vicinity of the contact line [57]. The size of such an area is fixed by the characteristics of the substrate. Since λ is the characteristic length in both direction, the area is λ^2. The activation energy writes (fig. 4.12):

$$E_a = E_2 - E_1 = \lambda^2 \left[(\sigma_{LV} + \sigma_{SV}) - \sigma_{SL}\right] = \lambda^2 \sigma_{LV}(1 + \cos\theta) \tag{4.40}$$

where the latter term is obtained by using the equilibrium contact angle θ from Young's law.

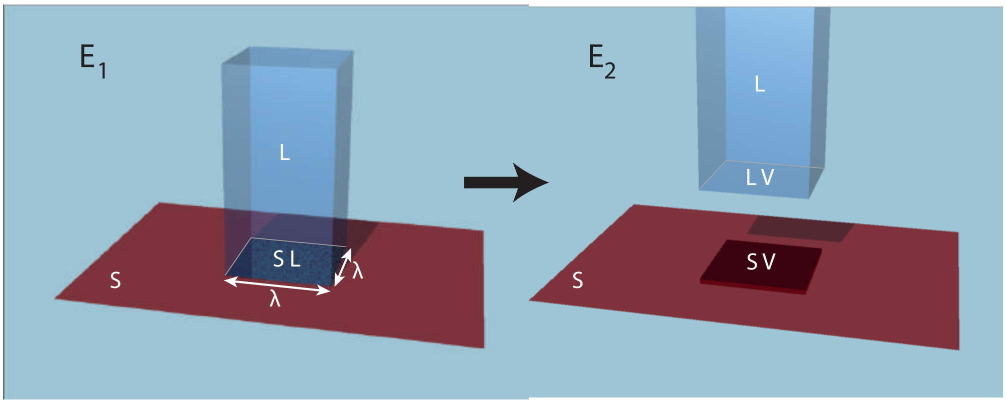

Figure 4.12: Schematic view of the work involved in the detachment of an area $\lambda \times \lambda$ from the solid substrate. λ is here considered as a characteristic length in both the directions. In the initial state (E_1), the water wets the solid substrate, and a liquid-solid interface is considered. When the area $\lambda \times \lambda$ is detached (E_2), the previous interface is suppressed and two new interfaces are created: liquid-vapor and solid-vapor. Each interface has its own surface tension. The activation energy is thus the difference of the two configurations, i.e. $E_a = E_2 - E_1 = \lambda^2 \left[(\sigma_{LV} + \sigma_{SV}) - \sigma_{SL}\right]$. Such an energy corresponds to the adhesion work for the area λ^2.

Note that E_a does not correspond to the energy gap ΔE between the final and the initial configuration of the triple line, i.e. the energy needed to wet an area λ^2 (fig. 4.13). Thermal agitation is involved in the detachment of the contact line and needs to overcome the barrier potential E_a.

The coefficient of proportionality in eq. 4.39 has been deduced from experimental observations [54] and a final expression for the jump rate κ_0 is:

$$\kappa_0 = \frac{k_B T}{\eta \upsilon_m} \exp - \frac{\lambda^2 \sigma_{LV}(1 + \cos\theta)}{k_B T} \tag{4.41}$$

where $\upsilon_m = 4 \cdot 10^{-29}$ m^3 denotes the molecular volume of water. It simply follows that the characteristic time of the fluctuations is $\tau = 1/\kappa_0$, i.e.:

$$\tau = \frac{\eta \upsilon_m}{k_B T} \exp \frac{\lambda^2 \sigma_{LV}(1 + \cos\theta)}{k_B T} \tag{4.42}$$

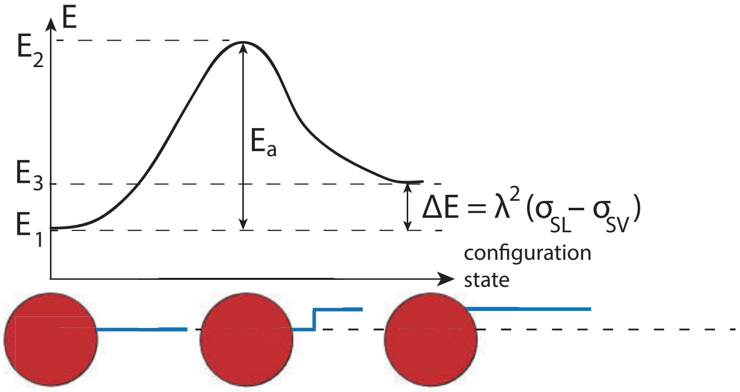

Figure 4.13: Behavior of the free surface energy as a function of the different configurations of the contact line (qualitative picture). At the initial configuration (E_1), corresponding to a straight contact line and a flat interface, the line stays at its equilibrium position. When an area λ^2 is detached (E_2), an additional work $E_a = E_2 - E_1$, corresponding to the adhesion energy, is needed (see fig. 4.12). Finally, the line lays on the particle surface, but at a non-equilibrium position (E_3). The energy gap between the final and the initial configuration $\Delta E = E_3 - E_1$ is the energy needed to wet an area λ^2. This behavior shows that E_a has the role of a barrier potential in a line displacement process.

For nanometric length scales, as found in our experiments (see par. 4.4.4), typical $\tau \sim 10^{-11} - 10^{-10}$ s. Such times are comparable with the mean time between molecular collisions [58]. Moreover, $\tau \ll \tau_b$, where τ_b is the ballistic time: such condition allows considering interfacial deformations as a random contribution in particle dynamics, as the one due to molecular collision.

4.4.4 Fitting of the friction term ζ_L due to thermal hopping

The contribution ζ_L of the triple line can be extract from the experimental data shown in chapter 2 (fig. 2.12). Starting from the ratio $r = D_S/D_V$ we write:

$$r = \frac{k_B T}{\zeta_S}\frac{\zeta_V}{k_B T} = \frac{6\pi\eta R}{\zeta_H + \zeta_L(\lambda)} \tag{4.43}$$

Hence,

$$\zeta_L(\lambda, \theta) = \frac{1}{r(\theta)} 6\pi\eta R - \zeta_H(\theta) \tag{4.44}$$

The resulting ζ_L versus θ is plotted in fig. 4.14 (points). ζ_H is also reported for comparison (solid line in fig. 4.14). At small contact angles (30° − 60°) the line contribution to particle drag is negligible with respect to the viscous drag. In fact, in this range, hydrodynamic theories are able to describe the colloidal dynamics [6]. Then, ζ_L increases with the contact angle and its effect becomes

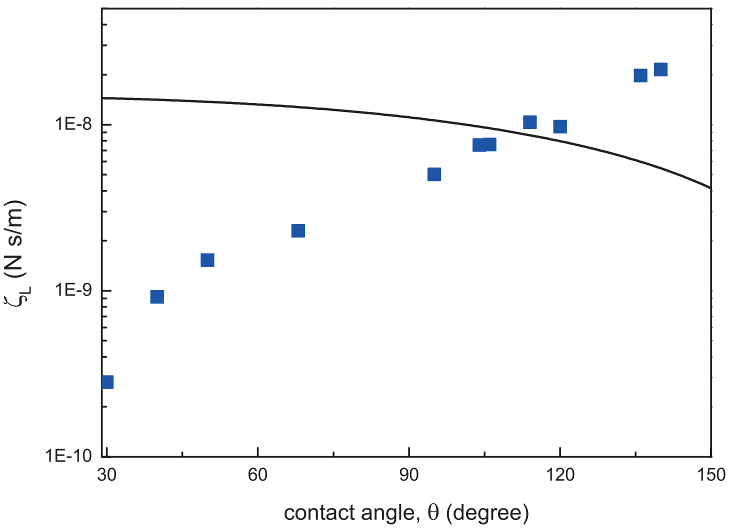

Figure 4.14: Points: additional drag ζ_L versus contact angle θ, in a semi-log scale. The values are recovered from experimental measurements (fig. 2.12), according to eq. 4.44. Solid line: hydrodynamics drag at the interface ζ_H versus θ, computed from the model provided by Fischer et al. [29]. ζ_L is negligible for small contact angles ($30° - 60°$), but it is comparable to, and also overcomes, the hydrodynamics drag for $\theta > 90°$.

more important: at $\theta = 95°$, ζ_L is just 2 times smaller than ζ_H. Finally, for hydrophobic beads, ζ_L is comparable to, and even overcomes at larger contact angles, ζ_H and its contribution to the drag becomes dominant. We can use the discussion in previous paragraphs to catch the behavior of such points. α in eq. 4.37 and τ in eq. 4.42 are replaced in eq. 4.20, leaving λ as the only free parameter:

$$\zeta_L = \frac{(1-\cos\alpha)^2}{2}\left(\frac{\sigma_{LV}}{k_B T}\right)^2 \lambda\pi R \sin\theta\eta\upsilon_m \exp\frac{\lambda^2\sigma_{LV}(1+\cos\theta)}{k_B T} \tag{4.45}$$

A constant λ cannot fit the data. Thus, we assume a dependence λ vs. θ. It is deduced combining the values in fig. 4.14 with eq. 4.45 and plotted in fig. 4.15a.

λ is in the nanometric range, as expected for a heterogeneous surface. The point at $\theta = 30°$, corresponding to bare silica surface, gives $\lambda = 0.48$ nm, in agreement with the measured spacing between hydrophilic SiOH groups [59]. After hydrophobic surface treatments, silane chains are added on the silica substrate, resulting in a decreasing of the number of free OH groups per area, i.e. an increase of the mean distance between them. Such an expected trend [59] is recovered (see fig. 4.15a). However, this behavior, and also the corresponding values for the jump rate κ_0, are different from the one calculated by Petrov et al. [60]. This discrepancy can be justified by the different nature of the considered substrate and by the small range of contact angles accessible in their experiments.

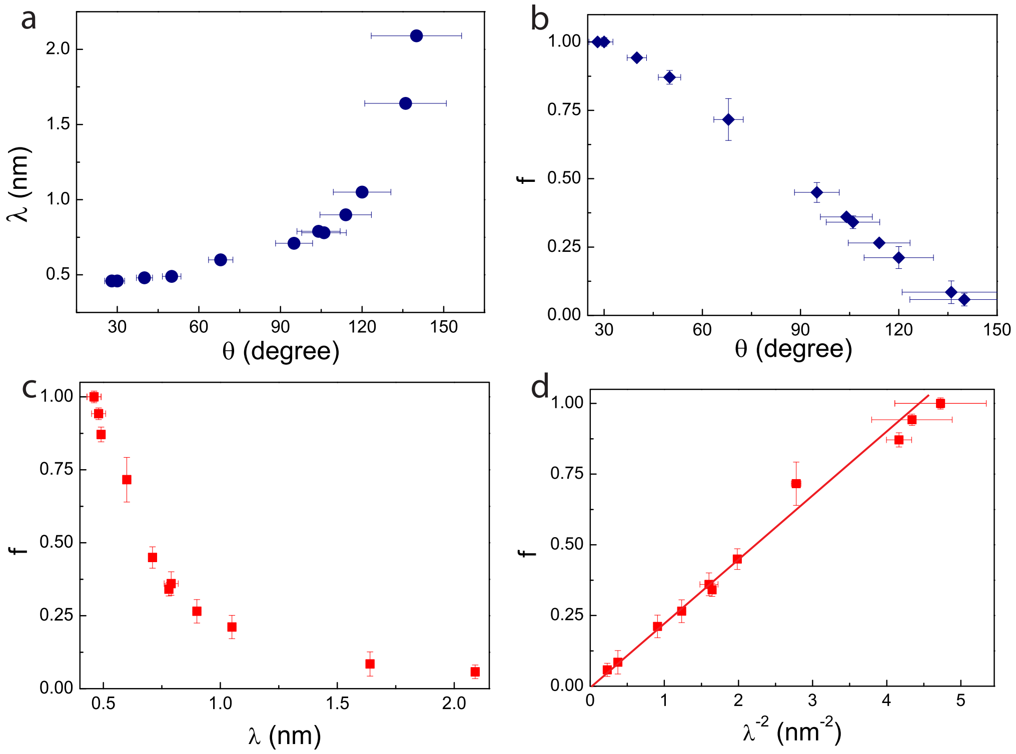

Figure 4.15: **a.** Average size of line jumps λ versus the contact angle θ. Points are obtained from the measured ratio r (fig. 2.12) via the proposed model (eq. 4.20). **b.** Fractional area f of free silica substrate in the Cassie–Baxter model versus contact angle θ, recovered from eq. 4.46. $f = 1$ is a bare silica substrate ($\theta = 30°$). f decreases when hydrophobic silane agents are added on the surface. **c.** Fractional area f versus the corresponding jump length λ. On a bare silica substrate ($f = 1$) $\lambda = 0.48$ nm, corresponding to the mean distance between OH groups. **d.** Red points: fractional silica area f versus λ^{-2}. λ^{-2} corresponds to the number of free OH groups per unit area. Solid line: best fit of the plotted values, showing the linear behavior of f vs. λ^{-2}. The fractional area follows a dilution law $f = (\lambda_0/\lambda)^2$.

The dependence λ versus θ in fig. 4.15a can be tentatively explained in the framework of the Cassie–Baxter model for heterogeneous surfaces. In our case we assume that, after adding silane, the particle surface is made of two sorts of regions: a hydrophilic region 1 and a hydrophobic region 2. The macroscopic contact angle of such substrate is given by the average of the contact angles of the two regions, weighted by the fractional area $f_1 = f$ and $f_2 = 1 - f$ occupied by each one:

$$\cos\theta = f\cos\theta_1 + (1 - f)\cos\theta_2 \tag{4.46}$$

In our case, $\theta_1 = 30°$ corresponds to the contact angle of bare silica beads (first point in fig. 4.15a), where no surface treatment was performed. $\theta_2 = 155°$

is slightly larger than the one usually found for silane treated surfaces. It can be considered as an effective value due to the presence of air bubbles between silane chains and water [61]. Using eq. 4.46, we recover f versus θ (fig. 4.15b). It simply follows from its definition that $f = 1$ at $\theta = 30°$ (bare silica substrate) and then it decreases when hydrophobic silane agents are added on the surface. The measured dependence of λ versus θ (fig. 4.15a) leads to a relation between the fractional silica area f and the jump length λ (fig. 4.15c). An increasing of the distance between hydrophilic sites translates in a more hydrophobic substrate, i.e. a decreasing f. To better analyze this dependence, let us plot the previous graph in a different scale, f versus λ^{-2} (fig. 4.15d). Note that λ^{-2} has the meaning of number of free OH groups per unit area. The linear behavior observed in fig. 4.15d allows writing the dependence

$$f = \left(\frac{\lambda_0}{\lambda}\right)^2 \tag{4.47}$$

where the constant $\lambda_0 = 0.48$ nm is the value of the jump length when $f = 1$.

Let us discuss a possible physical picture elucidating such dependence. In the case of the most hydrophilic beads ($\theta = 30°$), no silane is added and a bare silica substrate is considered (fig. 4.16a). The contact line can jump between OH groups, $\lambda_0 = 0.48$ nm apart, in agreement with the value provided in literature [59]. The addition of silane progressively covers such hydrophilic sites, since OH groups are substituted by a silane chains (fig. 4.16b). Here, the average distance between OH groups, and the corresponding line jump, corresponds to a new value $\lambda^* > \lambda_0$. This means that the average jump length λ increases with the number of covered sites. Over a surface, this mechanism have to follow a dilution law of hydrophilic regions in $(\lambda_0/\lambda)^2$, as experimentally found.

4.5 Particle drag due to capillary waves

We assume now a strongly pinned contact line, that it is not able to fluctuate anymore. However, the interface at its vicinity can fluctuate, because of thermal excitation. Such a deformation can be discussed in term of thermal capillary waves, as done by Smoluchowski [62]. The capillary fluctuations modify the interface slope (fig. 4.17) and give rise to random forces, as depicted in par. 4.2.

The line contribution ζ_L to the particle drag is still written as in eq. 4.20:

$$\zeta_L \simeq \frac{1}{2k_B T}\sigma_{LV}^2 \left(1 - \cos\alpha\right)^2 \lambda\pi R \sin\theta\tau$$

With respect to the previous case, just the physical meaning of the parameters α, τ and λ is changed.

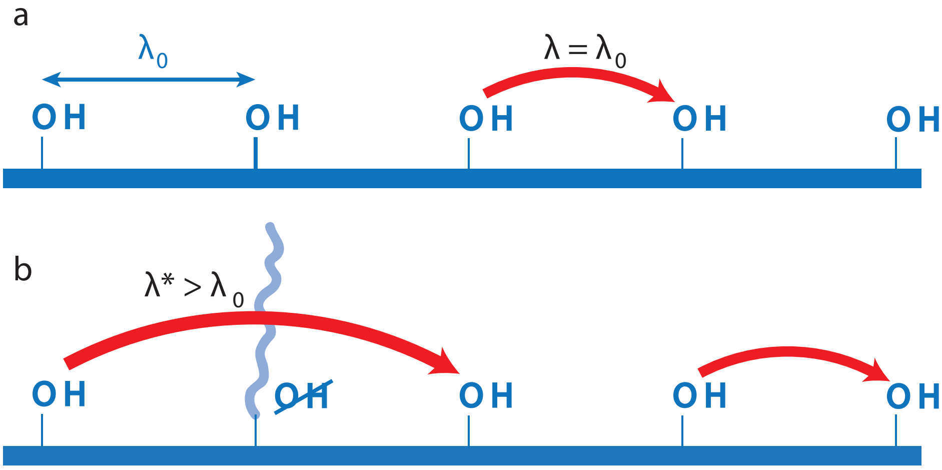

Figure 4.16: 1D Microscopic picture of line jumps and their dependence on the surface topography and hydrophobicity. **a,** At $\theta = 30°$, the displacement of the contact line is given by a characteristic size λ_0, i.e. the distance of OH groups on the bare silica substrate. **b,** Increasing hydrophobicity, added silane chains can randomly cover hydrophilic sites, which become unable to pin the line. Here, the new jump length is $\lambda^* > \lambda_0$. Elsewhere, this distance remains the same. Consequently, the average distance between pinning sites, and the mean jumps λ with it, increases with the hydrophobicity.

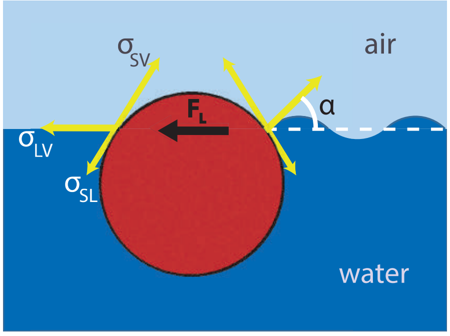

Figure 4.17: Sketch of local fluctuations at the interface in the case of a pinned line. A local capillary deformation of the interface is induced by thermal energy. The interface slope at the contact line is so changed of an average angle α, that gives rise to the random force F_L on the bead.

The distance λ denotes the *size* of the local capillary deformation and corresponds to the correlation length of a capillary wave [63], $\lambda = 1/k_{max}$, where $k_{max} = 2\pi/\ell$ is the largest wave-vector of capillary waves and ℓ is a molecular distance. A more detailed discussion is needed for an estimation of the slope of the interface and of the life–time of the fluctuation.

4.5.1 Interface slope α at the particle

The profile of the fluctuating interface depends on two energy contributions:

- the gravitational energy ΔE_g due to the displacement of matter along the vertical axis;
- the surface energy ΔE_c, related to the extra interface area generated by the waves.

Let us denote the local interface position with the coordinate $\mathbf{r} = (x, y, h(x, y))$, where $h = 0$ is the mean position of the interface. In order to displace water over a distance h along $\mathbf{g}$, in an infinitesimal area $dxdy$, gravity contributes

$$\delta E_g = \int_0^h h' g(\rho - \rho') dxdydh' = \frac{1}{2} g(\rho - \rho') h^2 dxdy \tag{4.48}$$

where g is gravity acceleration and $\rho > \rho'$ are the densities of the two fluid phases.

The contribution of the interfacial tension, due to the extra area in the same infinitesimal region, is

$$\delta E_c = \sigma_{LV} \delta A = \sigma_{LV} dxdy \left(\sqrt{1 + h_x^2 + h_y^2} - 1\right) \simeq \frac{1}{2} \sigma_{LV} dxdy \left(h_x^2 + h_y^2\right) \tag{4.49}$$

where $h_i = \partial h / \partial i$ $(i = x, y)$, with the hypothesis that $h_x^2 \ll 1$, $h_y^2 \ll 1$.

In an arbitrary region $L \times L$, the energy contributions ΔE_g, ΔE_c are obtained from integration of eqs. 4.48, 4.49.
By expanding in a Fourier series:

$$h = \sum_{\mathbf{k}} h_{\mathbf{k}} e^{i(k_x x + k_y y)} \tag{4.50}$$

and using the Parseval's identity

$$\frac{1}{L^2} \int_{L^2} h^2 dxdy = \sum_{\mathbf{k}} |h_{\mathbf{k}}|^2$$

we obtain

$$\Delta E = \Delta E_g + \Delta E_c = \frac{1}{2} L^2 \sum_{\mathbf{k}} |h_{\mathbf{k}}|^2 \left[g(\rho - \rho') + \sigma_{LV} k^2\right] \tag{4.51}$$

According to equipartition theorem, the work necessary to create one mode is $k_B T/2$ [64]; from eq. 4.51 we thus recover the thermal average of the square of each Fourier component [65]:

$$\langle |h_{\mathbf{k}}|^2 \rangle = \frac{k_B T}{L^2 \sigma_{LV}} \frac{1}{k^2 + \ell_c^{-2}} \tag{4.52}$$

where ℓ_c is the capillary length: $\ell_c = \sqrt{\sigma_{LV}/[g(\rho - \rho')]}$.

Using again the Parseval's identity, eq. 4.52 is related to the mean square interfacial roughness after a capillary deformation:

$$\sum_{\mathbf{k}} \langle |h_{\mathbf{k}}|^2 \rangle = \frac{1}{L^2} \int_{L^2} h^2 dxdy = \langle h^2 \rangle \tag{4.53}$$

The summation in eq. 4.53 is approximated by the integral

$$\sum_{\mathbf{k}} \langle |h_{\mathbf{k}}|^2 \rangle \simeq \frac{L^2}{4\pi^2} \int_{k_{min}}^{k_{max}} |h_{\mathbf{k}}|^2 \, dk^2 \tag{4.54}$$

Combining eqs. 4.52, 4.53, 4.54

$$\langle h^2 \rangle = \frac{k_B T}{4\pi^2 \sigma_{LV}} \ln \left[\frac{k_{max}^2 + \ell_c^{-2}}{k_{min}^2 + \ell_c^{-2}} \right] \tag{4.55}$$

k_{max} and k_{min} are cut–off values for the wavevector. We have $k_{max} = 2\pi/\ell$, where ℓ is a molecular length, and $k_{min} = 2\pi/L$, with L a typical system size, as introduced above.

These results are used to find the slope of a thermally deformed interface at the contact line [63]. For the sake of simplicity, the dissertation is reduced to a 1D system and the interface is considered pinned at the particle surface: $h = 0$ at $x = a_0$ (fig. 4.18).

Eq. 4.50 is so expressed in a simplified form:

$$h = \sum_k h_k \sin\left(k(x - a_0)\right) \tag{4.56}$$

and the slope of the interface at the contact line ($x = a_0$) is thus:

$$\tan\alpha = \left.\frac{\partial h}{\partial x}\right|_{x=a_0} = \sum_k h_k k \tag{4.57}$$

A strong approximation is here required, since the amplitude of each mode is unknown. Hence, we roughly assume $\langle h_k \rangle \sim \sqrt{\langle h_k^2 \rangle}$ and eq. 4.57 becomes

$$\tan\alpha \sim \sum_k \sqrt{\langle h_k^2 \rangle} k \sim \sum_k \sqrt{\frac{k_B T}{\sigma_{LV}}} \frac{1}{L} \sim n \sqrt{\frac{k_B T}{\sigma_{LV}}} \frac{1}{L} \tag{4.58}$$

i.e. the sum of a constant term over the n modes of the capillary wave.

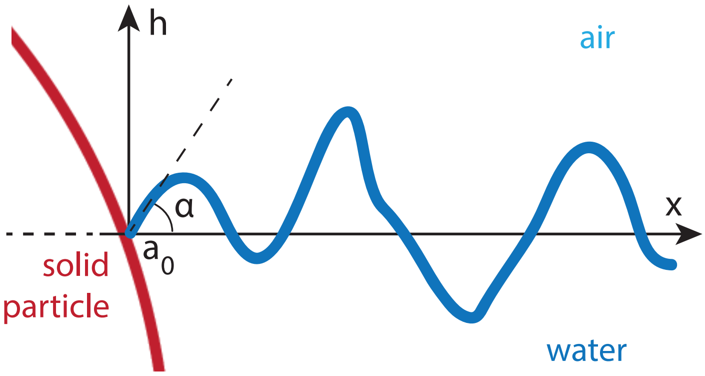

Figure 4.18: 1-D schematic view of a capillary deformation of an air-water interface. The new interface profile is denoted by $h(x)$. The interface fluctuates around the mean position $h = 0$ and it is pinned at the contact line $h(x = a_0) = 0$. We are interested in the slope of the air-water interface at the particle surface: the corresponding average angle α is estimated in the text.

If $n = k_{max}/k_{min} = L/\ell$, according to previous definitions, we finally have an estimation of the magnitude of the interface slope:

$$\tan\alpha \sim \sqrt{\frac{k_B T}{\sigma_{LV}}\frac{1}{\ell}} \tag{4.59}$$

The corresponding mean value at room temperature ($T = 25$°C) at the air–water interface ($\sigma_{LV} = 0.072$ N/m), for a nanometric λ, is $\alpha \sim 0.5 - 1$ rad. Such a value for the slope of the interface is comparable to the one provided in the case of a moving line. This means that also capillary waves deform significantly the interface and their effect in particle dynamics, via contact line fluctuations, has to be considered.

4.5.2 Characteristic time τ of capillary fluctuations

In order to find the life–time of fluctuations, one need to calculate the fluctuation correlation time. We assume a non-Markovian process (the interface height at a time t depends on the random forces $F_{\mathbf{k}}(s)$ at all the previous times $s < t$) and, according to Langevin theory, an alternative form for h is written [66]:

$$h_{\mathbf{k}}(t) = \int_{-\infty}^{t} ds \chi_{\mathbf{k}}(t-s) F_{\mathbf{k}}(s) \tag{4.60}$$

where $\chi_{\mathbf{k}}$ is the response function. In the Fourier space, this term is given by [67, 68]:

$$\chi_{\mathbf{k}}(\omega) = \frac{1}{-i\omega\gamma_{\mathbf{k}}(\omega) + \sigma_{LV}k^2} \tag{4.61}$$

and

$$\gamma_{\mathbf{k}}(\omega) = \frac{2\omega\rho}{k\left[i + \left(\frac{i\omega}{\nu k^2} - 1\right)^{-1/2}\right]} \tag{4.62}$$

with ν the kinematic viscosity of the liquid.

The thermal, random force $F_{\mathbf{k}}$ is provided taking into account fluctuation-dissipation relation and equipartition theorem:

$$\langle F_{\mathbf{k}}(t)F^*_{\mathbf{k}}(0)\rangle = k_B T\gamma_{\mathbf{k}}(t) \tag{4.63}$$

In the strong damping limit ($\nu k^2 \gg 1$), eqs. 4.61, 4.62, 4.63 are simplified:

$$\gamma_{\mathbf{k}}(\omega) = 4\rho\nu k - \frac{3\rho i\omega}{k} + \frac{\rho\omega^2}{4k^3\nu} + O(\nu^{-2}) \simeq 4\rho\nu k \tag{4.64}$$

$$\chi_{\mathbf{k}}(\omega) \simeq \frac{1}{-i4\omega\rho\nu k + \sigma_{LV}k^2} \tag{4.65}$$

and

$$\langle F_{\mathbf{k}}(\omega)F^*_{\mathbf{k}}(0)\rangle \simeq 4\rho\nu k\omega k_B T \tag{4.66}$$

The inverse Fourier transform allows to return in time domain; eq. 4.65 becomes

$$\chi_{\mathbf{k}}(t) \simeq \frac{1}{4\eta k}\exp\left(-\frac{\sigma_{LV}k}{4\eta}t\right)\Theta(t) \tag{4.67}$$

where $\Theta(t)$ is the Heaviside function, and

$$\langle F_{\mathbf{k}}(t)F^*_{\mathbf{k}}(0)\rangle \simeq 4\rho\nu k k_B T\delta(t) \tag{4.68}$$

with $\delta(t)$ Dirac delta function.

Using eq. 4.60, the height-correlation function results as

$$\langle|h_{\mathbf{k}}(t)|^2\rangle = \frac{k_B T}{\sigma_{LV}k^2}\left[1 - \exp\left(-\frac{\sigma_{LV}k}{2\eta}t\right)\right] \tag{4.69}$$

At long time scales, we recover the expression found in eq. 4.52; the life–time for each mode of the capillary wave is thus

$$\tau_{\mathbf{k}} = \frac{2\rho\nu}{\sigma_{LV}k} = \frac{2\eta}{\sigma_{LV}k} \tag{4.70}$$

In a rough approximation we state that, when the *fastest* mode vanishes, a different capillary deformation, not yet correlated with the previous one, is occurring. The resulting correlation time τ is written:

$$\tau = \tau_{k,min} = \frac{2\eta}{\sigma_{LV}k_{max}} \tag{4.71}$$

As in the previous case, typical values of τ ($\tau \sim 10^{-11} - 10^{-10}$ s $\ll \tau_b$) justify to treat the capillary waves contribution as a random force on the particle.

4.5.3 Fitting of the friction term ζ_L provided by capillary waves

The discussion in the previous sections allows to express eq. 4.20 in the form:

$$\zeta_L = \frac{(1-\cos\alpha)^2}{2k_BT}\eta\sigma_{LV}\pi a_0\lambda^2 \tag{4.72}$$

Two different approaches are used in order to obtain an estimation of λ. In the first one (fig. 4.19), λ is considered independent of the surface properties of the particle. Constant values of λ (0.5 nm, 1 nm, 2 nm), in agreement with the molecular scale, provide the right order of magnitude for ζ_L ($\sim 10^{-9} - 10^{-8}$N s/m), but they are not able to catch the dependence on the contact angle θ.

In the second one (points in fig. 4.20), a variable λ is used to get the measured additional friction drag, according to eq. 4.72.

Also in this case, λ is found in the nanometric range. A curve $\lambda = A/(1+\cos\theta)$ fits reasonably the experimental data (solid line in fig. 4.20). The $\frac{1}{1+\cos\theta}$ dependence is found from few considerations. In the present model, we consider the effect of interface fluctuations around a pinned contact line. For large fluctuations, the line can eventually de–pin and move on the particle surface with a negligible dissipation. It follows that fluctuations that induce the detachment of the contact line do not contribute to ζ_L. The condition under which this effect occurs is here discussed in terms of a cut–off wavevector. The notion of contact angle hysteresis does not apply to such a nanometric scale [21], so the detachment of the line needs to be treated with a different approach.

A thermal capillary force F_{th} acting on the contact line is considered. The line stays pinned when F_{th} do not overcome the adhesion force F_a on a segment $\ell_n = 1/k_n$, i.e. the lateral extension of the capillary deformation [63] at the selected wavevector k_n. According to eq. 4.40, proposed in the regime of a moving line, the adhesion force F_a is calculated from:

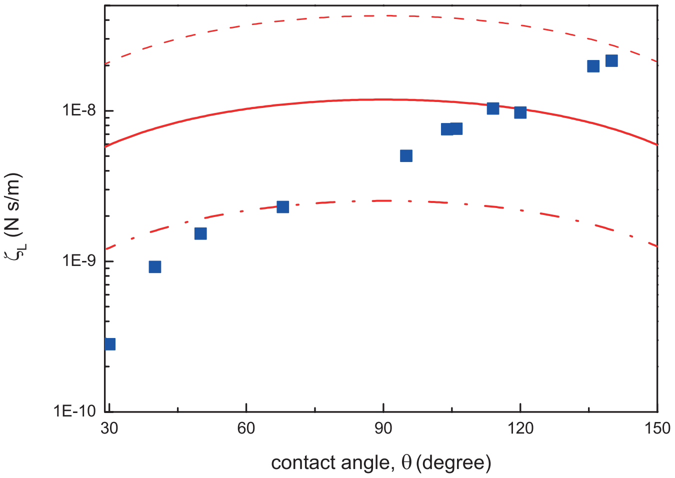

Figure 4.19: Points: additional drag ζ_L versus contact angle θ, computed from eq. 4.72. Lines: the parameter λ is here considered constant to the reasonable values of $\lambda = 0.5$ nm (dash–dotted line), 1 nm (solid line), 2 nm (dashed line), in agreement with molecular distances. All of them provide the right order of magnitude for ζ_L ($\sim 10^{-9}$ N s/m), but they are not able to catch the dependence on θ.

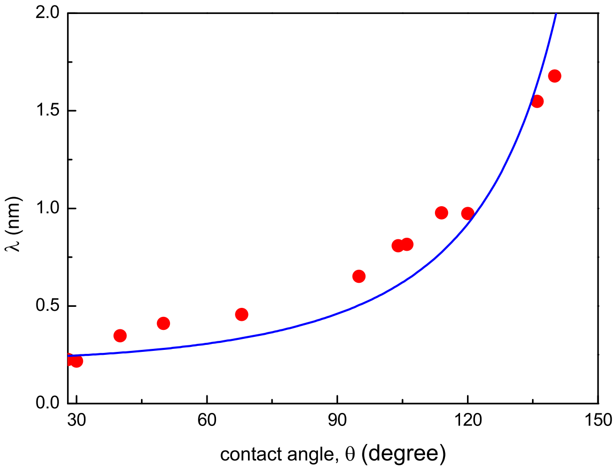

Figure 4.20: Points: lateral correlation length λ of the capillary waves, here used as free parameter, as a function of the contact angle θ. Values of λ are computed according to eq. 4.72 in order to recover the measured additional drag (see fig. 4.19). Solid line: the behavior $\lambda \sim 1/(1+\cos\theta)$ is proposed to fit the experimental data (eq. 4.75).

$$\ell_n F_a = E_a = \ell_n^2 \sigma_{LV} (1 + \cos\theta) \tag{4.73}$$

The condition $F_a \geq F_{th}$ becomes:

$$\ell_n = \frac{1}{k_n} \geq \frac{F_{th}}{\sigma_{LV}} \frac{1}{1 + \cos\theta} \tag{4.74}$$

The term in the right hand side corresponds thus to a threshold value $1/k_{max}$. Since the correlation length of the capillary fluctuation was defined as $\lambda = 1/k_{max}$, as stated at the beginning of this section, the behavior plotted in fig. 4.20 (solid line) is recovered:

$$\lambda = \frac{F_{th}}{\sigma_{LV}} \frac{1}{1 + \cos\theta} \tag{4.75}$$

This argument could be a starting point for future deeper analyses.

4.6 Conclusion

In this chapter, a theoretical discussion of the diffusion of spherical beads at the air–water interface was proposed. The purpose was to find an explanation for intriguing behavior observed in our experiments: an increasing viscous drag when the particles are less immersed in water. Here we explored the role of random forces on the bead due to thermally activated fluctuations of the interface at the contact angle, that add to the usual ones due to the molecular shocks. Such fluctuations were associated to molecular jumps in the case of a moving contact line and to capillary waves in the regime of a pinned line. Using the fluctuation-dissipation theorem and the equipartition theorem we introduced an additional drag able to catch the colloidal dynamics at the interface. This term is written as a function of the characteristic size of the fluctuation, which is left as the only free parameter. In order to recover the measured additional drag, such a length needs to be in the nanometric range, in agreement with the molecular origin of the phenomenon. Moreover, in both the regimes we are also able to associate the enhancement of the drag for hydrophobic beads to an increase of the correlation length, considering the non–ideal properties of the solid substrate.

Quando così il mio dramma si complicò, cominciarono le mie incredibili pazzie.

When the drama became complicated, my incredible acts of madness began.

Luigi Pirandello

Chapter 5

Fluctuation of the contact line in spheroidal colloids

Introduction

In the present chapter, we generalize the model of drag enhancement due to interface fluctuations at the contact line to the more complex morphology of prolate spheroidal colloids. The drag coefficient ζ is computed as the sum of the two contributions, ζ_H and ζ_L, as we have done for spherical beads. We consider their dependence on the aspect ratio ϕ for both rotational (par. 5.1) and translational (par. 5.2) dynamics. Since the contact line length varies with the aspect ratio, we can expect an enhancement of the drag for more elongated colloids.

5.1 Rotational diffusion at the interface

We consider the rotational motion of a spheroidal particle around a vertical z–axis, with respect to the azimuthal angle φ. The corresponding rotational diffusion coefficient is known when the colloid is totally immersed in the fluid [36] (see par. 1.5.1):

$$\zeta_{\varphi,V} = 6\eta V G_{\varphi} \tag{5.1}$$

η is the viscosity of the fluid, V denotes the volume of the particle and the geometric factor G_{φ} depends on the aspect ratio ϕ.

Very few works considered the rotational motion at the interface [69, 70], but a qualitative argument can be used. Given the partial immersion in water, we expect a reduced hydrodynamic drag $\zeta_{\varphi,H}$ at the interface with respect to the value in the volume $\zeta_{\varphi,V}$. However, the measured drag at the interface is much larger (from

5 to 10 times, going from 3 to 10 in aspect ratio) than the one in volume (fig. 3.19 in chapter 3, or see fig. 5.4 par. 5.1.2). In such a range of aspect ratio, the hydrodynamic drag can be safely neglected. In the following, we will compute the drag $\zeta_{\varphi,L}$ from interfacial deformations, as dominant term in the rotational dynamics.

5.1.1 Calculation of the contact line contribution $\zeta_{\varphi,L}$ to rotational drag

For the sake of simplicity, we compute the effect of interfacial fluctuations in the case of a flat contact line. This is a first–order approximation, since a constant macroscopic contact angle at a non–spherical particle induces a deformation of the contact line [40] and, consequently, of the air-water interface at its vicinity (see par. 1.6). PSI measurements of the interface height around a spheroidal particle (par. 3.3) confirm this theoretical prediction and quantify the gap Δz between the lowest and the highest points of the interface (fig. 5.1a). As an example, at $\phi = 2.7$ we measure $\Delta z = 80$ nm. Such a deformation amplitude is negligible with respect to the particle extension $2b = 1.38\mu$m on the vertical axis (fig. 5.1b). The same behavior has been measured by Loudet et al. [40] in the whole range of experimentally accessible aspect ratios. For this reason, our approximation is valid for a first estimation of the rotational drag. A second order correction due to a non-planar line could be then considered, but it is not subject of the present study.

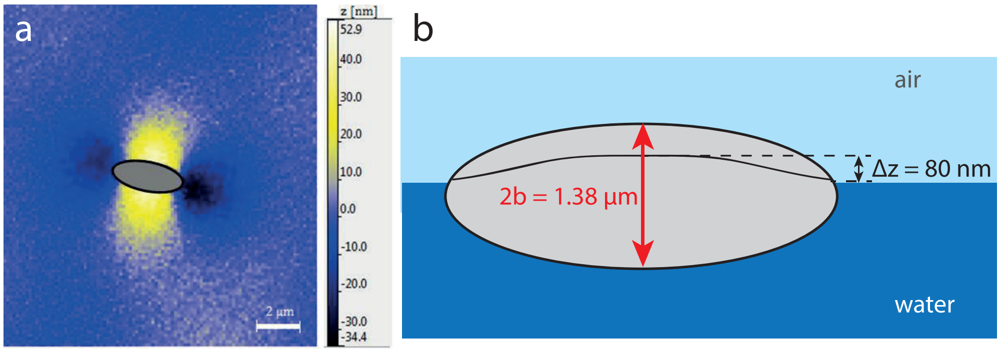

Figure 5.1: **a.** False color image of the interface around a spheroidal particle with aspect ratio $\phi = 2.7$. To achieve a constant contact angle at a particle with a non-constant curvature radius, the interface needs to be higher at the center of the spheroid (yellow zone) and lower at the tips (dark blue zone). **b.** Sketch (not in scale) of the front view of a spheroidal particle at the interface. The distance between the highest and lowest points of the interface is $\Delta z = 80$nm, recovered from PSI measurement. The vertical size of the particle is $2b = 1.38\mu$m, so $\Delta z \ll 2b$.

In such hypothesis, a net horizontal component of a force applied at the contact line exerts a torque that makes the spheroid rotate on the interfacial plane. In the case of a random force $\mathbf{F}_{L,i}$ due to a generic line fluctuation i, the corresponding torque is

$$\mathbf{\Gamma}_{L,i} = \mathbf{r}_i \times \mathbf{F}_{L,i} \tag{5.2}$$

$\mathbf{r}_i$ is the distance between the site i on the contact line and the center of the particle (fig. 5.2) and it is a function of the angular position φ_i. The symbol × stands for cross product.

Such a random torque Γ_L along the vertical axis, due to interface fluctuations, is associated to the particle rotational drag $\zeta_{\varphi,L}$, via Langevin equation and fluctuation-dissipation theorem:

$$\zeta_{\varphi,L} \simeq \frac{1}{2k_BT}\langle\Gamma_L(0)^2\rangle\tau \tag{5.3}$$

The term $\langle\Gamma_L(0)^2\rangle$ is thus estimated.

The magnitude of the torque is written in the form:

$$\Gamma_{L,i} = F_L r_i(\varphi_i)\sin\nu_i(\varphi_i) \tag{5.4}$$

where ν_i is the angle between the random force and the vector r_i, as depicted in fig. 5.2; both of them are a function of φ_i. The magnitude F_L of the random force is instead not dependent on the angular position, since it rises from a local fluctuation. We recall the expression provided in the previous chapter, as a function of the parameters λ (mean length of a fluctuation) and α (average slope of the deformation):

$$F_L = \sigma_{LV}\lambda\left(1-\cos\alpha\right) \tag{5.5}$$

where σ_{LV} is the air-water surface tension.

The quantities r_i and ν_i are calculated as a function of the parameter φ and of the aspect ratio ϕ. First of all, we parameterize the contact line as an ellipse in a Cartesian coordinate system (x, y), with axes $\tilde{a} = a\sin\theta$ and $\tilde{b} = b\sin\theta$. θ is the contact angle and a, b the axes of the spheroid. The relation with the angular coordinate φ is given by

$$x = \tilde{a}\cos\varphi \qquad y = \tilde{b}\sin\varphi \tag{5.6}$$

The distance $\mathbf{r}$ of a generic point of the contact line from the center (fig. 5.2) has a modulus:

$$r^2 = x^2 + y^2 = \tilde{a}^2\cos^2\varphi + \tilde{b}^2\sin^2\varphi = \tilde{b}^2\left(\phi^2\cos^2\varphi + \sin^2\varphi\right) \tag{5.7}$$

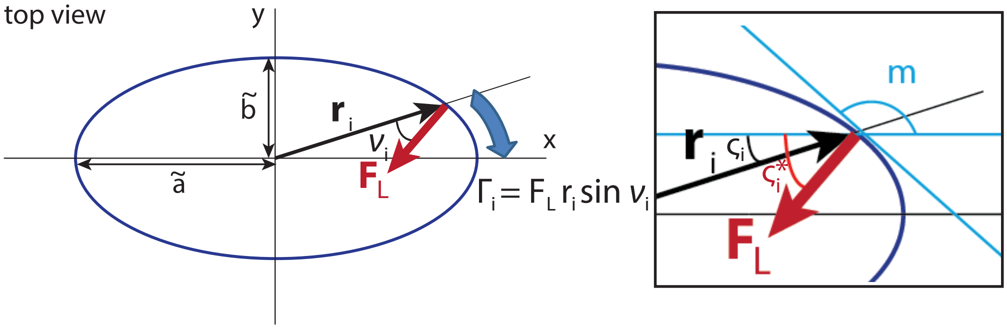

Figure 5.2: Top view of the contact line of a spheroidal particle. The contact line is an ellipse of axes $(\tilde{a}, \tilde{b})$ in a Cartesian coordinate system (x, y). A random force $\mathbf{F}_L$ acts on a generic point of the contact line, at a distance $\mathbf{r}_i$ from the center of the particle. We have so a resulting torque, whose magnitude is $\Gamma_i = F_L r_i \sin \nu_i$, where ν_i is the angle between the vectors $\mathbf{F}_L$ and $\mathbf{r}_i$, for a given fluctuation i. *Inset*: detail of the line force on the contact line. ς_i is the orientation of the distance $\mathbf{r}_i$, with respect to the horizontal axis. In the same way, ς_i^* gives the orientation of the line force. The angle ν_i is finally recovered as $\varsigma_i^* - \varsigma_i$.

The orientation of the vector $\mathbf{r}$, with respect to the horizontal axis x, is provided by the angle ς:

$$\tan \varsigma = \frac{y}{x} = \frac{1}{\phi} \tan \varphi \tag{5.8}$$

To obtain the orientation ς^* of the line force $\mathbf{F}_L$, we consider that $\mathbf{F}_L$ is normal at the contact line in the considered point. If we call m the angular coefficient of the tangent of the ellipse, we have:

$$\tan \varsigma^* = -\frac{1}{m} = \frac{\tilde{a}^2 y}{\tilde{b}^2 x} = \frac{\tilde{a} \sin \varphi}{\tilde{b} \cos \varphi} = \phi \tan \varphi \tag{5.9}$$

The angle ν between the two vectors is thus

$$\nu = \varsigma^* - \varsigma \tag{5.10}$$

Now that all the physical quantities are defined, we can consider the total random torque, given by all the possible fluctuations at a fixed time:

$$\boldsymbol{\Gamma}_L = \sum_i \boldsymbol{\Gamma}_{L,i} \tag{5.11}$$

The random origin of the fluctuations translates in a null ensemble average

$$\langle \boldsymbol{\Gamma}_L \rangle = 0 \tag{5.12}$$

but in a non–null squared ensemble average

$$\langle \Gamma_L^2 \rangle = \sum_{i,j} \langle F_i F_j r_i r_j \sin\nu_i \sin\nu_j \rangle = \langle F_i^2 \rangle \sum_{i=0}^{n} r_i^2 \sin^2 \nu_i \tag{5.13}$$

with n number of possible fluctuations.

The summation in eq. 5.13 can be written as an integral along the contact line, since the mean length λ of a fluctuation is much smaller than the contact line perimeter ($\lambda \simeq d\ell$).

$$\sum_{i=0}^{n} r_i^2 \sin^2 \nu_i = \frac{1}{\lambda} \oint r_i^2 \sin^2 \nu_i d\ell \tag{5.14}$$

where the infinitesimal arc length on the ellipse perimeter is known

$$d\ell = \tilde{b}\sqrt{\phi^2 \sin^2 \varphi + \cos^2 \varphi} d\varphi \tag{5.15}$$

Substituting in eq. 5.14 and using previous definitions (eqs. 5.7, 5.8, 5.9), we obtain

$$\sum_{i=0}^{n} r_i^2 \sin^2 \nu_i = \frac{\tilde{b}}{\lambda} \int_0^{2\pi} r_i^2 \sin^2 \nu_i \sqrt{\phi^2 \sin^2 \varphi + \cos^2 \varphi} d\varphi =$$

$$\frac{\tilde{b}^3}{\lambda} \int_0^{2\pi} \left(\phi^2 \cos^2 \varphi + \sin^2 \varphi\right) \sin^2 \left(\varsigma^* - \varsigma\right) \sqrt{\phi^2 \sin^2 \varphi + \cos^2 \varphi} d\varphi \tag{5.16}$$

We denote with $I(\phi)$ the integral:

$$I(\phi) = \int_0^{2\pi} \left(\phi^2 \cos^2 \varphi + \sin^2 \varphi\right) \sin^2 \left(\varsigma^* - \varsigma\right) \sqrt{\phi^2 \sin^2 \varphi + \cos^2 \varphi} d\varphi \tag{5.17}$$

which is numerically solved taking into account the extended expressions for r^2 (eq. 5.7) and ν (eq. 5.10).

We can now express $\zeta_{\varphi,L}$ as:

$$\zeta_{\varphi,L} = f_l \frac{I(\phi)}{\phi} \tag{5.18}$$

where f_l contains all the local terms and constants related to the fluctuations. According to the previous discussion, f_l writes:

$$f_l = \frac{1}{2k_B T} \sigma_{LV}^2 \left(1 - \cos\alpha\right)^2 r_0^3 \sin^3 \theta \left[\lambda \tau(\lambda)\right] \tag{5.19}$$

since $\tilde{b}^3 = \frac{r_0^3}{\phi} \sin^3 \theta$, where r_0 is the radius of the spherical bead before the stretching process.

The dependence on the aspect ratio, provided by $I(\phi)/\phi$, is plotted in fig. 5.3.

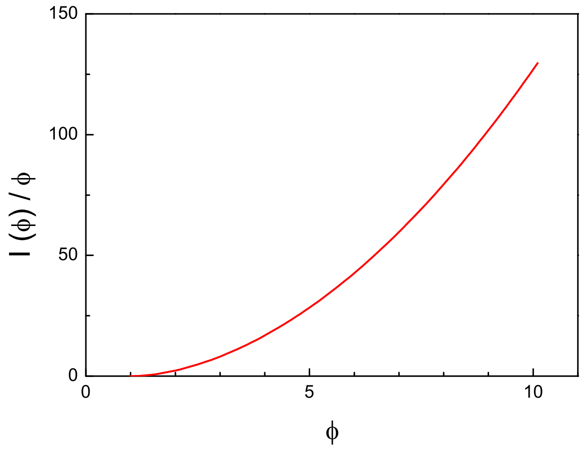

Figure 5.3: Numerical solution of the integral $I(\phi)$ (eq. 5.16), divided by ϕ, as a function of the aspect ratio. This term provides the dependence $\zeta_{\varphi,L}$ vs. ϕ. $I(\phi = 1) = 0$ (no contribution at spherical beads), then the integral increases over 2 orders of magnitude in the accessible range of aspect ratio.

At $\phi = 1$, i.e. for spherical beads, the term is null. A radial random force $\mathbf{F}_L$ is parallel to the radius $\mathbf{r}$. Thus, the cross product $\boldsymbol{\Gamma} = \mathbf{r} \times \mathbf{F}_L$ is identically null. It follows that fluctuations of the interface at the contact line do not affect the rotation of a sphere around a vertical z–axis. Their contribution is instead rapidly increasing with the aspect ratio, and $I(\phi)/\phi$ varies over 2 orders of magnitude in the experimentally accessible range $1 - 10$ of aspect ratio.

5.1.2 Experimental versus calculated rotational diffusion coefficient

The rotational diffusion coefficient D_φ for a spheroidal colloid at the interface is expressed, according to previous sections, as:

$$D_\varphi \simeq \frac{k_B T}{\zeta_{\varphi,L}} = \frac{k_B T}{f_l} \frac{\phi}{I(\phi)} \tag{5.20}$$

since $\zeta_{\varphi,V}$ is negligible with respect to the other terms, except for small aspect ratios ($\phi \simeq 1$) (fig. 5.4a). The dependence on the aspect ratio ϕ is provided only by the term $I(\phi)/\phi$, that is able to catch the qualitatively behavior of the measured diffusion coefficient D_φ (fig. 5.4b). Note that no free parameters are contained in $I(\phi)/\phi$ and that it has been computed without any assumptions on the nature of the fluctuations. These considerations give robustness to the proposed idea of an interfacial dynamics driven by the triple line. The term $k_B T/f_l$ is instead constant

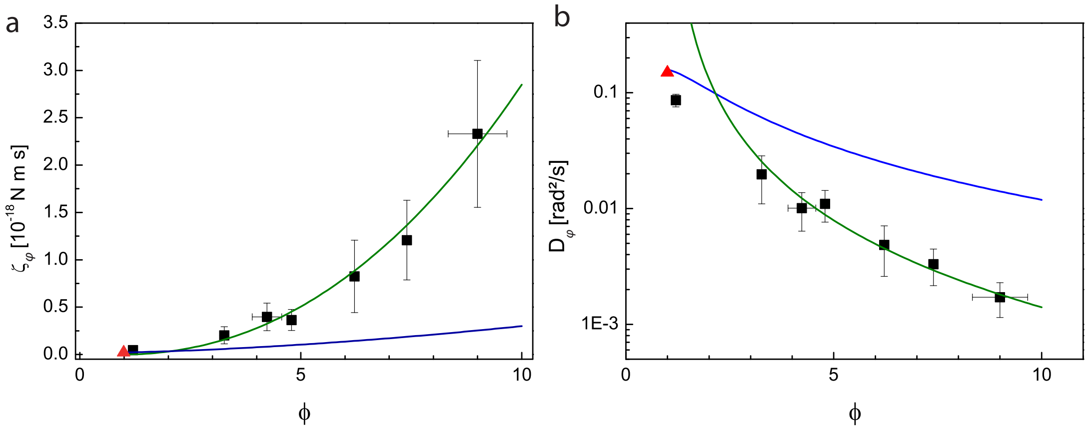

Figure 5.4: **a.** Rotational drag ζ_φ on the spheroidal colloid, as a function of the aspect ratio ϕ. Points: direct measurement of the drag, obtained from the experimental diffusion coefficients (see chapter 3). Blue line: rotational drag coefficient $\zeta_{\varphi,V}$ for a spheroid totally immersed in water. Such a term is negligible with respect to the measured values. Green line: fluctuation line contribution $\zeta_{\varphi,L} = f_l I(\phi)/\phi$. f_l is here a best fit parameter. **b.** Rotational diffusion coefficient D_φ vs. the aspect ratio ϕ in semi-log scale, for a spheroidal particle at the air–water interface. Black points are the average values on 3 to 6 direct measurements of the rotational diffusion coefficient, as already reported in chapter 3, fig. 3.19. The error bars correspond to the standard deviation of the averaged values. The red point is a measure of the rotational diffusion coefficient for a Janus sphere ($\phi = 1$). Solid blue line is the diffusion coefficient $D_{\varphi,V}$ for particles totally immersed in water, and it is here used just for comparison. Solid green line is the estimation recovered by the proposed model for the rotational diffusion at the interface:$k_B T/\zeta_{\varphi,L}$.

with respect to ϕ and depends on all the parameters λ, τ and α characteristic of the fluctuations (see eq. 5.19). For a particle at the air–water interface ($\sigma_{LV} = 0.072$ N/m), with an initial radius $r_0 = 0.98\mu$m and a contact angle $\theta \simeq 50°$, and considering that $\alpha \sim 0.5$ rad, only the quantity $\lambda\tau(\lambda)$ is unknown. Such a term is used as a free parameter to fit the experimental D_φ (points in fig. 5.4b), except the first one. In fact, at low aspect ratios, the hydrodynamics drag $\zeta_{\varphi,H}$ is not negligible with respect to $\zeta_{\varphi,L}$ and the present model does not apply. The best fit (green lines in fig. 5.4) leads to

$$\lambda\tau(\lambda) = (3.59 \pm 0.13)\, 10^{-20}\text{m} \cdot \text{s} \tag{5.21}$$

Such a value is discussed in the two regimes of a moving and of a pinned line, as done for spherical beads in the previous chapter.

In the framework of Molecular Kinetic Theory [52], where the contact line is moving around its equilibrium position because of thermally activated jumps, the correlation time τ is the inverse of an Arrhenius-like jump rate. The characteristic length λ is instead left as the only free parameter.

In order to fit the experimental data (eq. 5.21), we need an average jump size $\lambda = 0.52 \pm 0.01$ nm. This value is in agreement with the ones usually proposed in literature [52] for a mean molecular jump.

For fluctuations induced by capillary wave, τ is the damping time of the fastest mode. We recover, from the fit in eq. 5.21, $\lambda = 1.13 \pm 0.02$ nm. This value is again in agreement with the proposed molecular scale of the capillary deformation.

5.2 Translational diffusion at the interface

5.2.1 Estimation of the translational hydrodynamic drag

Differently from the case of spheres, no complete theories have been developed for the case of spheroidal particles at the interface. For this reason we propose here a qualitative method to estimate the translational hydrodynamic drag coefficient $\zeta_{T,H}$ at an air–water interface. In the case of spherical particles, all the theories state that the interfacial drag is proportional to the Stokes-Einstein friction in the volume:

$$\zeta_{V,sphere} = 6\pi\eta R \tag{5.22}$$

reduced by the dimensionless drag coefficient β ($\beta < 1$), function of the immersion depth in the more viscous medium:

$$\zeta_{H,sphere} = \beta\zeta_{V,sphere} \tag{5.23}$$

In the hydrodynamic view provided by Fischer [29] and used in the previous chapter, β is a function of the contact angle θ:

$$\beta = \sqrt{\tanh[32(1+\cos\theta)/(9\pi^2)]} \tag{5.24}$$

The expression of β is not known for spheroidal particles. For the sake of simplicity, we assume that the dimensionless drag only depends on the immersion depth of the particle, and not on the particle shape:

$$\beta(\theta, \phi) \simeq \beta(\theta, \phi = 1) \tag{5.25}$$

Substituting eq. 5.24 in eq. 5.23 and using the drag coefficient for a fully immersed spheroid (par. 1.5.1), an estimation for the hydrodynamic term $\zeta_{T,H}$ in translational dynamics, along the long and the short axes, is obtained:

$$\zeta_{T,H} = 6\pi\sqrt{\tanh[32(1+\cos\theta)/(9\pi^2)]}\eta b G_{a,b} \tag{5.26}$$

5.2.2 Calculation of the contact line contribution in translational drag

As reported in the discussion of rotational dynamics, a local fluctuation gives rise to an average random force $\mathbf{F}_{L,i}$, independent on its angular position φ_i and on the shape of the particle:

$$\mathbf{F}_{L,i} = \sigma_{LV}\lambda(1-\cos\alpha)\hat{\mathbf{u}}_i \tag{5.27}$$

where $\hat{\mathbf{u}}_i$ is the unit vector normal to the contact line (fig. 5.5). As usual, σ_{LV} is the air-water surface tension, λ is the mean length of a line fluctuation and α is the average slope of the interface after a fluctuation. The random force is associated to a translational drag via Langevin equation and fluctuation-dissipation theorem, as proposed in the previous chapter and in [71] for spherical beads (eq. 4.19):

$$\zeta_{T,L} \simeq \frac{1}{2k_BT}\langle F_L(0)^2\rangle\tau \tag{5.28}$$

where the index T denotes translational dynamics and τ is the correlation time of the fluctuation.

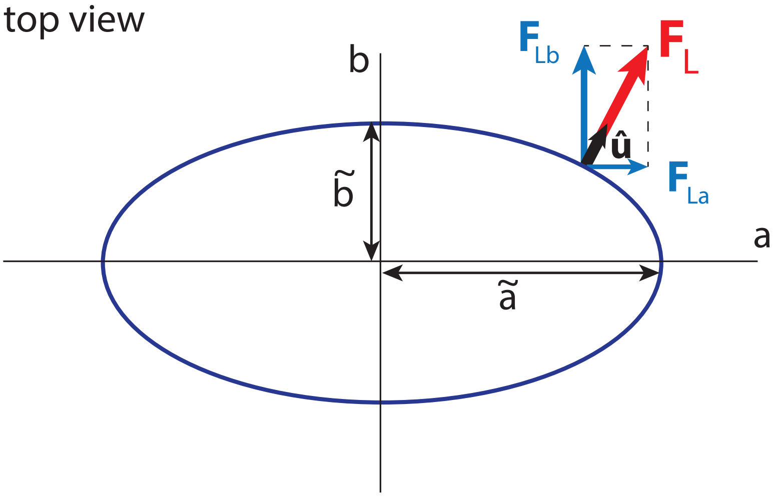

Figure 5.5: Top view of the contact line of a spheroidal particle. The contact line is an ellipse of axes $(\tilde{a},\tilde{b})$. A random force $\mathbf{F}_L$ acts on a generic point of the contact line. Its direction is defined by the unit vector $\hat{\mathbf{u}}$, normal to the contact line. For our purpose, we consider the components of the random force parallel to the main axes: F_{La} and F_{Lb}.

The components along the main axes a and b write

$$\begin{aligned} F_{La,i} &= \sigma_{LV}\lambda(1-\cos\alpha)\cos\varphi_i \\ F_{Lb,i} &= \sigma_{LV}\lambda(1-\cos\alpha)\sin\varphi_i \end{aligned} \tag{5.29}$$

Let now consider the effect of a large number of fluctuations on the motion of the bead:

$$F_{La} = \sum_i F_{La,i} \qquad F_{Lb} = \sum_i F_{Lb,i} \tag{5.30}$$

Contrary to the case of random torques in the previous section, here we can easily manage the summatories. We consider the number n of possible fluctuations at a given time as

$$n = p/\lambda \tag{5.31}$$

where the perimeter p of the contact line is divided by the average lateral length of each fluctuation λ. Note that the contact line length, that is the circumference of an ellipse of axes $(\tilde{a}, \tilde{b})$, is a function of the aspect ratio ϕ. To compute such a length, we need to solve the complete elliptic integral of the second kind. However, a good approximation was provided by Ramanujan [72]:

$$p = \pi \left[3\left(\tilde{a} + \tilde{b}\right) - \sqrt{\left(3\tilde{a} + \tilde{b}\right)\left(\tilde{a} + 3\tilde{b}\right)} \right] \tag{5.32}$$

Taking into account that the aspect ratio $\phi = a/b$ and the volume of the initial bead of radius r_0 is conserved during the stretching process, i.e. $r_0^3 = ab^2$, eq. 5.32 is re-written as a function of the aspect ratio:

$$p(\phi) = \frac{\pi r_0 \sin\theta}{\sqrt[3]{\phi}} \left[3\left(\phi + 1\right) - \sqrt{\left(3\phi + 1\right)\left(\phi + 3\right)} \right] \tag{5.33}$$

where r_0 is constant in our experiments. The contact line length as a function of ϕ, for particles with the same volume, is plotted is fig. 5.6. The contact line length is increasing with the aspect ratio, when we consider spheroids with the same volume. For the highest experimentally achievable aspect ratio, $\phi = 10$, the contact line is 3 times longer with respect to the unstretched spherical bead. In the same way, also the number of possible fluctuations $n = p/\lambda$ occurring at the same time, is increasing with ϕ. This result suggests that the contact line contributes more in translational dynamics when the particle is more elongated and an enhancement of the corresponding drag is attended.

To quantify this effect, we compute the total random force by summing over the $n(\phi)$ possible fluctuations. Their random nature translates in null ensemble averages:

$$\begin{aligned} F_{La} &= \sum_{i=0}^{n} F_{La,i} = \sigma_{LV}\lambda(1-\cos\alpha)\sum_{i=0}^{n(\phi)}\cos\varphi_i = 0 \\ F_{Lb} &= \sum_{i=0}^{n} F_{Lb,i} = \sigma_{LV}\lambda(1-\cos\alpha)\sum_{i=0}^{n(\phi)}\sin\varphi_i = 0 \end{aligned} \tag{5.34}$$

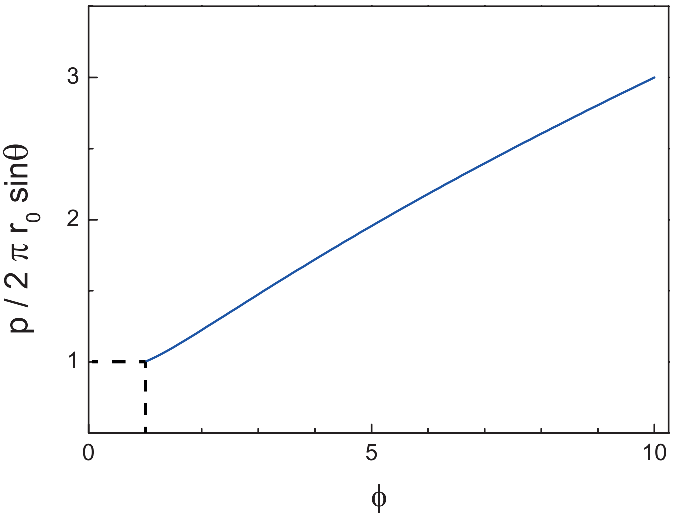

Figure 5.6: Normalized contact line length, calculated as the perimeter of the ellipse of axes $(\tilde{a}, \tilde{b})$, as a function of the aspect ratio ϕ. At $\phi = 1$, we recover the circumference of a circle: $p/2\pi r_0 \sin\theta = 1$, where r_0 is the radius of the bead and θ its contact angle. Spheroidal particles with the same volume, but increasing aspect ratios, have longer contact lines: for rod-like particles, with $\phi = 10$, the contact line is 3 times longer with respect to a sphere and more fluctuations at the triple line are possible.

The squared ensemble averages are instead non-null:

$$\langle F_{La}^2 \rangle = n(\phi)\langle F_{La,i}^2 \rangle = \frac{1}{2} n(\phi) \left[\sigma_{LV}\lambda(1-\cos\alpha)\right]^2$$

$$\langle F_{Lb}^2 \rangle = n(\phi)\langle F_{Lb,i}^2 \rangle = \frac{1}{2} n(\phi) \left[\sigma_{LV}\lambda(1-\cos\alpha)\right]^2 \tag{5.35}$$

and they are used in the expression for the contact line contribution $\zeta_{T,L}$ to the particle drag

$$\zeta_{La} \simeq \frac{1}{2k_BT} \langle {F_{La}}^2 \rangle \tau$$

$$\zeta_{Lb} \simeq \frac{1}{2k_BT} \langle {F_{Lb}}^2 \rangle \tau \tag{5.36}$$

5.2.3 Experimental versus calculated translational diffusion coefficients

The translational diffusion coefficients D_a and D_b for a spheroid at the interface are then calculated as a function of the aspect ratio ϕ:

$$D_{a,b} = \frac{k_BT}{\zeta_{T,H} + \zeta_{T,L}} \tag{5.37}$$

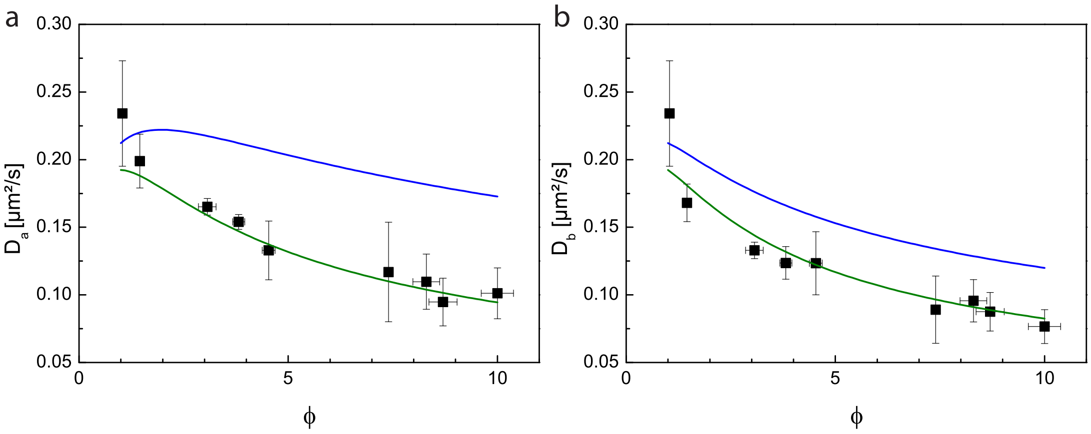

Figure 5.7: Translational diffusion coefficients D_a along the long axis (**a**) and D_b along the short axis (**b**), vs. the aspect ratio ϕ, for a spheroidal particle at the air–water interface. Black points are direct measurements of the D_a and D_b, as already reported in chapter 3 (figs. 3.16, 3.17). Solid blue lines are the diffusion coefficient D_V for particles totally immersed in water, used here just for comparison. Solid green lines are the estimation recovered by the proposed model for the translational diffusion at the interface. We considered both the effect of a partial immersion in hydrodynamics drag ($\zeta_{T,H}$) and the additional dissipation due to the contact line ($\zeta_{T,L}$).

where $\zeta_{T,H}$ and $\zeta_{T,L}$ have the form discussed in the previous sections. The latter depends on the product $\lambda\tau(\lambda)$. We use the same value obtained from the best fit of the rotational diffusion coefficient D_φ (eq. 5.21). No free parameters are used in this discussion. The theoretical predictions are compared with the experimental values, already shown in chapter 3, and plotted in fig. 5.7.

The contribution of the fluctuations at the contact line provides the additional drag that was needed to explain the initially unexpected slowed-down diffusion. The model curves well agree, in both the case, with the measured values and they are able to catch the slower dynamics when the aspect ratio is increasing. Note that no free parameters are used: λ is here fixed by the value obtained by the best fit for rotational diffusion. This crucial feature adds consistency to the proposed approach.

5.3 Conclusion

Starting from the experimental data shown in chapter 3 we conceived a model to predict the slowed–down diffusion coefficients of spheroidal particles at the air–water interface. We followed the same arguments that drive the model for spherical beads (see chapter 4): fluctuations of the interface at the contact line gives rise to random forces and torques that affect particle motion and are responsible of an additional dissipation. For what concerns the rotational dynamics, the random torque due to line fluctuation strongly depends on the considered geometry, and varies over 3 orders of magnitude in the experimentally accessible range $1 \div 10$ of aspect ratio. In this way, we were able to catch the measured, extremely slowed–down rotational diffusion coefficient D_φ, without assuming any hypothesis about the nature of the fluctuation. The characteristic size of the fluctuation was left as the only free parameter, and discussed in the two regimes of a moving and of a pinned contact line. From the best fit of the data we obtained such a length in the nanometric range in both cases, in agreement with the molecular origin of the phenomenon. The same fit value was used in the model for the translational dynamics, obtaining a good agreement between the model and the data of the diffusion coefficients D_a and D_b.

Forsan et haec olim meminisse iuvabit. - Forse un giorno ci allieterà ricordare tutto questo.

Probably, in the future, it will be pleasing to remember these things.

Virgilio, Eneide I

Conclusion and outlook

In this thesis, the Brownian motion of colloidal particles at an air–water interface was deeply investigated. Two kinds of system were considered. In the first experiences, performed before the beginning of this thesis, the translational diffusion coefficient of spherical beads was measured as a function of the immersion depth, tuned by silanization treatments of the particle surface. Thereafter, in this PhD work, the diffusion at the interface was extended to anisotropic polystyrene spheroids. Different aspect ratios were obtained, ranging from spherical–like to rod–like particles, by stretching spherical beads in a homemade apparatus. This morphology allowed to analyze the translational diffusion coefficients along the particle main axes, and the rotational diffusion coefficient on the interfacial plane. The immersion depth and the eventual deformation of the interface around the particle were measured by interferometry. The dynamics was followed by particle tracking techniques using a bright field optical microscope equipped with a CCD camera.

The experimental results were surprising and thought–provoking, since they are contrary to common intuition and established models: the diffusion at the interface was found slower than expected. Spherical particles with their larger part in air exhibited a diffusion coefficient even lower than the one expected for a sphere totally immersed in water. Theories that take into account the partial immersion in water, but neglect the role of the contact line, overestimated the diffusion coefficient.
A huge slowed diffusion was measured for spheroidal colloids, especially in the rotational degree of freedom. At large aspect ratios, the rotational dynamics is one order of magnitude slower than predicted for a particle totally immersed in the bulk. The translational diffusion is founded two times lower than the one in the volume.

These considerations demanded a different theoretical paradigm able to capture these unexpected dynamics. Additional sources of dissipation, as wedge flow and curved meniscus were taken into account, but their values fail to reproduce the measured ones.

Fluctuations of the contact line were then considered. Two kinds of fluctuations are possible: a fluctuating contact line on the particle surface, due to molecular jumps between surface adsorption sites, and capillary fluctuations of the interface in the case of a pinned contact line. Both of them locally change the orientation of the interfacial forces at the particle, resulting in a random force that affects the particle dynamics. Langevin equation and fluctuation–dissipation theorem relate such a fluctuating contribution to an additional drag, able to catch the experimental results. This term is written as a function of only one free parameter, a characteristic correlation length λ of the fluctuation. We recovered the measured additional drag, by using a λ in the nanometer range, in agreement with the molecular origin of the phenomenon.

For prolate spheroidal particles, the extremely slowed–down rotational dynamics as a function of the aspect ratio were well reproduced just using geometrical considerations, without any assumption about the nature of the fluctuation. A quantitative agreement with the experimental data is achieved using the correlation length λ as a fit parameter: a reasonable nanometric length is obtained. The same value is able to fit also the translation diffusion along both the long and the short axis.

These considerations show that line fluctuations are an important and general mechanism that strongly affect the dynamics of partially wetted colloid at the interface.

This work opens highways of research in the field of interfacial particle dynamics. First of all, we plan to extend our investigations to the case of super–hydrophobic beads, in order to explore very large contact angles ($\theta > 150°$), where the beads are almost completely in air. A fresh collaboration started with the group of H.–J. Butt in Max Planck Institute of Mainz (Germany), that made super–hydrophobic raspberries colloids with, in principle, very high contact angles.

The size effect will be also addressed. In fact, in our model we considered a sort of mean field of a large number of fluctuations. For particle sizes of the order of surface heterogeneities ($\sim$ 1 nm) we expect that the mean field approach breaks down and an enhanced contribution of line fluctuations to particle dynamics occurs.

In the case of spheroidal particles, future studies will consider the effect of the interface curvature on the lateral forces and on the Brownian dynamics of the colloid. We plan to measure the morphologic torque induced by the interface deformation, produced by the spheroid, and the imposed interface curvature. Such a torque will be also measured in the case of new fabricated anisotropic particles, made by a cylinder with two hemispherical heads, presenting a constant curvature and thus not deforming the interface. This new system will allow also to address the role of interface deformation in Brownian motion.

Appendix

A.1: Particle tracking

As described in chapters 2 and 3, the dynamics of a single particle is observed by bright field microscopy and a digital video is recorded by a CCD camera at 30 frame/s. Particle tracking methods [46] are implemented in an IDL software. For the sake of simplicity, we report just the main steps of the analysis. The first one is the determination of the position (x, y) of the intensity center of mass of the bead in each frame.

```
sXi = 0.0
sYi = 0.0
Int = 0.0
sI = 0.0

for j = IObj(i-1)+1, IObj(i) do begin
    Int = 1.0*Img(IObj(j))
    x = IObj(j) mod npx
    y = (IObj(j)-x)/npx

    sI = sI + 1*Int
    sXi = sXi + x*Int
    sYi = sYi + y*Int
endfor

XObj = 1.0*sXi/sI
YObj = 1.0*sYi/sI
```

The terms $XObj$ and $YObj$ in the software correspond to the position (x, y) of the center of the particle. The process is repeated in the whole stack to recover the particle trajectory. In the same way, the orientation of a spheroidal particle is obtained at a given frame. See chapter 3, par. 3.5 and fig. 3.9 for more details.

A preliminary analysis counts the number of non-null pixels in the first ($x - XObj > 0$, $y - YObj > 0$) and in the second quadrant ($x - XObj < 0$, $y - YObj > 0$). The range of values for the orientational angle φ is so reduced: $[0, \pi/2]$ if most of the points are in the first quadrant, $[\pi/2, \pi]$ otherwise. In any case, such a range is written in the form $[f1, f2]$.

```
sX = 0.0
for j = IObj(i-1)+1, IObj(i) do begin
    Int = 1.0*Img(IObj(j))
    x = IObj(j) mod npx
    y = (IObj(j)-x)/npx
    if y gt YObj then sX = sX + (x - XObj)
endfor

if sX gt 0 then begin
   f1 = 0
   f2 = !pi/2
endif else begin
   f1 = !pi/2
   f2 = !pi
endelse
```

The sum $N1$ and $N2$ of the distances of each point j of the projected ellipse in the image, with respect to the axis $f1$ and $f2$ respectively, are calculated.

```
N1 = 0.0
N2 = 0.0
for j = IObj(i-1)+1, IObj(i) do begin
    Int = 1.0*Img(IObj(j))
    x = IObj(j) mod npx
    y = (IObj(j)-x)/npx
    y1 = -(x-XObj)*sin(f1) + (y-YObj)*cos(f1)
    N1 = N1 + y1^2
    y1 = -(x-XObj)*sin(f2) + (y-YObj)*cos(f2)
    N2 = N2 + y1^2
endfor
```

$N1$ and $N2$ are compared and the farthest extreme is replaced by the midpoint value $(f1 + f2)/2$. The same procedure is so repeated in a smaller, halved range.

```
for o = 1, 40 do begin
    if N2 lt N1 then begin
```

```
        f3 = (f1 + f2)/2
        f1 = f2
        f2 = f3
        N1 = N2
      endif else  f2 = (f1 + f2)/2

     N2 = 0.0
     for j = IObj(i-1)+1, IObj(i) do begin
         Int = 1.0*Img(IObj(j))
         x = IObj(j) mod npx
         y = (IObj(j)-x)/npx
         y1 = -(x-XObj)*sin(f2) + (y-YObj)*cos(f2)
         N2 = N2 + y1^2
     endfor
 endfor
```

A.2: Angular confinement of a spheroidal colloid

In the first measurements we take the same container used with spherical beads and described in par. 2.1.2. It is a cylindrical container fixed on a microscope glass slide. The diameter is 10 mm and it is partially filled up to 0.8 mm in height with deionized water. During particle tracking measurements (par. 3.5), the top of the cylinder is covered by a thin flat piece of borosilicate glass, in order to avoid contamination of the interface or evaporation of the water. Particles are sprayed on the interface by an airbrush and at very dilute surface concentrations (less than 0.01% s/s). We focus our attention in a tiny central area, far from the meniscus on the container walls. However, if the container radius is of the order of $2\ell_c$ (where $\ell_c \simeq 2.7$mm is the capillary length), as in this case, a slight slope due to the meniscus is still present. This slope has a negligible effect on the translational motion, as confirmed by measurements with both spherical and spheroidal colloids. Aberrations can appear instead when we analyze rotational dynamics. In this case, a coupling between the curvature of the interface and the orientation of the particle, leading to an orientational confinement, is expected [43] and measured in our experiment. We analyze the behavior of $\Delta\varphi$ measured in the small cuvette. The typical curve for the MSD $\langle\Delta\varphi^2\rangle$ vs. time lag τ in this case is reported in fig. A.1 (red points).

For small time lag $\tau < \tau_1$, a linear behavior, characteristic of Brownian motion, is measured. For larger time lag, the MSD flattens and reaches a plateau, indicating an angular confinement of the particle. This orientational confinement is probably due to the coupling between the curvature of the interface and the orientation

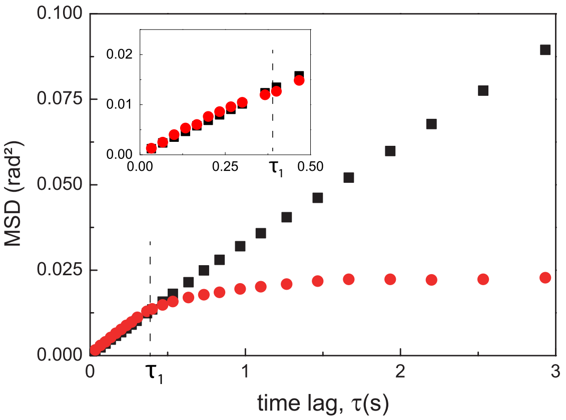

Figure A.1: Rotational MSD vs. time lag τ for spheroidal particles with aspect ratio $\phi = 3$. Red points: particle in a small container of 10 mm in diameter. The linear behavior, denoting Brownian diffusion, is observed at small time lag, $\tau < \tau_1$. At a larger time, $\tau > \tau_1$, the curve flattens until reaching a plateau, corresponding to an angle of $\sqrt{\langle \varphi^2 \rangle} \simeq 0.14$ rad ($\simeq 9°$). Black points: particle in the large container of 6 cm in diameter (fig. 3.2, chapter 3). The angular confinement is ruled out. *Inset*: detail of MSD at small time lags, where the linear behavior is measured for both the samples.

of the particle [43], since it is not observed in larger containers (black points in fig. A.1). Further works will verify this hypothesis and we will use this effect for quantitative measurements of such a curvature induced torque on the spheroids.

This effect motivates the upgrade of the experimental set-up shown in chapter 3 (fig. 3.2), in order to explore the rotational dynamics in the case of spheroids.

A.3: Possible contribution at the viscous drag of a moving contact line

We consider the role of the line friction as an additional source of dissipation in the particle Brownian dynamics. Such a dynamics is composed by a sequence of linear ballistic trajectories, characterized by an instantaneous velocity [6]

$$v = \sqrt{\frac{2k_BT}{m}} \simeq 1\text{mm/s}$$

and a ballistic time

$$\tau_p = \frac{m}{\zeta} \simeq 0.1\mu s$$

where m is the particle mass and ζ is the total friction felt by the bead. This means that, over a time τ_p, the particle is moving on a straight line at a constant velocity v; after τ_p, the direction of the motion is changed due to molecular collision. There are two possible ways in which such a motion can interfere with the contact line:

- the motion of the bead induces a pressure field that deforms the interface. The unbalanced interfacial forces are so acting on the contact line;
- a rotational motion couples with the translation of the particle. Since the interface stays flat, the contact line needs to move with respect to the surface of the particle.

In both cases, a relative velocity v_L between the contact line and the solid substrate is deduced; the corresponding power dissipation P is computed by integration on the whole perimeter:

$$P = \oint f v_L d\ell = \oint \frac{1}{2}\zeta_0 v_L^2 d\ell$$

For the sake of simplicity, the two dissipations are here discussed only for a contact angle $\theta = 90°$.

A.3.1: Effect of the pressure field

Let us consider a rectilinear and uniform motion of the bead immersed in an incompressible fluid. The small Reynolds number

$$Re = \frac{\rho v R}{\eta} \sim \frac{10^3 \cdot 10^{-3} \cdot 10^{-6}}{10^{-3}} \sim 10^{-3} \ll 1$$

with ρ and η density and viscosity of the fluid respectively, v velocity of the particle and R radius of the bead, allows to simplify the Navier-Stokes equation [73]:

$$\eta \nabla^2 \mathbf{v} - \mathbf{grad} p = 0$$

where p denotes the pressure.

Landau [16] provided a solution of the Navier–Stokes equation in order to get the 3-D pressure field induced by the moving particle:

$$p = p_0 - \frac{3}{2}\eta \frac{\mathbf{v} \cdot \mathbf{n}}{\mathbf{r}^2} R$$

p_0 is the fluid pressure at infinity, $\mathbf{r}$ is the distance from the center of the particle (fig. A.2a) and $\mathbf{n}$ is the unit vector parallel to $\mathbf{r}$.

When the particle is at the interface, such a profile is modified by boundary conditions and a general solution is not available. The only case that we can easily treat is at $\theta = 90°$ where, due to the symmetry of the problem, both the pressure and the shear stress fields are unperturbed (fig. A.2b).

In such a case, the 2-D pressure field on the plane of the interface can be obtained and expressed in polar coordinates (r, φ) (fig. A.2a):

$$p = p_0 - \frac{3}{2}\eta\frac{vR}{r^2}\cos\varphi$$

The pressure deforms the profile z of the interface, according to Young-Laplace equation:

$$\sigma_{LV}\nabla^2 z = (p - p_0) + \rho g z$$

that, in polar coordinates and taking the 2-D equation of the pressure field, is:

$$\frac{\partial^2 z}{\partial r^2} + \frac{1}{r}\frac{\partial z}{\partial r} + \frac{1}{r^2}\frac{\partial^2 z}{\partial \varphi^2} = -\frac{\beta\cos\varphi}{r^2} + \frac{z}{\ell_c^2}$$

where $\ell_c = \sqrt{\sigma_{LV}/(\rho g)}$ is the capillary length and $\beta = \frac{3}{2}\eta v R/\sigma_{LV}$.

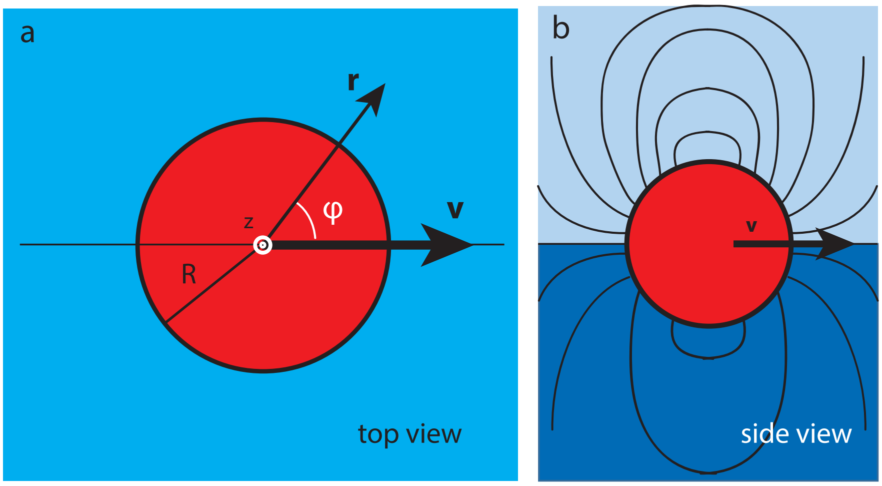

Figure A.2: **a.** Top view of a moving spherical bead of radius R at the air–water interface. The polar coordinates system (r, φ) is reported. The polar angle φ is defined with respect to the direction of the velocity $\mathbf{v}$. The vertical axis z is perpendicular to the figure. **b.** Schematic view of the shear stress around a spherical bead, moving at a velocity $\mathbf{v}$ (side view). In the volume, both the pressure and the shear stress fields induced by the motion are symmetric with respect to $\theta = 90°$. If an interface at $\theta = 90°$ is considered, the pressure and shear stress fields in each fluid are the same as the ones in the corresponding volume.

With the ansatz $z(r, \varphi) = \tilde{z}(r)\cos\varphi$, the angular part is easily solved. We obtain the equation for the radial part $\tilde{z}(r)$:

$$\tilde{z}'' + \frac{1}{r}\tilde{z}' - \left(\frac{1}{r^2} + \frac{1}{\ell_c^2}\right)\tilde{z} = -\frac{\beta}{r^2}$$

that can be solved in the two extreme cases:

- $r \gg \ell_c$
$$\tilde{z}'' - \frac{1}{\ell_c^2}\tilde{z} = 0 \qquad\qquad \tilde{z}(r) = k_1 e^{\frac{r}{\ell_c}} + k_2 e^{-\frac{r}{\ell_c}}$$

- $r \ll \ell_c$
$$\tilde{z}'' + \frac{1}{r}\tilde{z}' - \frac{1}{r^2}\tilde{z} = -\frac{\beta}{r^2} \qquad\qquad \tilde{z}(r) = \frac{c_1}{r} + c_2 r + \beta$$

The constants k_1, k_2, c_1, c_2 are recovered from boundary conditions:

1. at $r \to \infty$, $\tilde{z}(r) = 0$
2. at $r = R\cos\alpha$, $\tilde{z}(r) = R\sin\alpha$, where α is the angular position of the contact line (see fig. A.3a)
3. $\tilde{z}_1(\ell_c) = \tilde{z}_2(\ell_c)$, where $\tilde{z}_1$, $\tilde{z}_2$ are the solutions of the Young–Laplace equations in the two extreme cases
4. $\tilde{z}_1'(\ell_c) = \tilde{z}_2'(\ell_c)$

The first condition stands for an unperturbed interface at long distance from the particle; condition 2 states that the contact line has to lie on the particle surface at the angular position α (see fig. A.3a). This angle changes in time, because of the motion of the contact line, according to the equation

$$v_L = R\frac{d\alpha}{dt}$$

Finally, conditions 3 and 4 impose the continuity of the solutions in the two regimes.

An approximated solution for profile $z(r, \varphi)$, in the limit $R \ll \ell_c, \alpha \ll 1$, is:

$$z(r,\varphi) = \begin{cases} \left[\frac{3}{2}\frac{\eta v R}{\sigma_{LV}}\left(1 - \frac{R}{r}\right) + \frac{R^2\alpha}{r}\right]\cos\varphi & r \ll \ell_c \\ \frac{3}{4}\frac{\eta v R}{\sigma_{LV}} e^{1-\frac{r}{\ell_c}}\cos\varphi & r \gg \ell_c \end{cases}$$

We are interested in the deformation of the surface around the particle, at the contact line ($r = R\cos\alpha \simeq R$). The variation of contact angle $\Delta\theta$ (fig. A.3a) will be

$$\Delta\theta \simeq \left.\frac{\partial z}{\partial r}\right|_{r=R} = \left(\frac{3}{2}\frac{\eta v}{\sigma_{LV}} - \alpha\right)\cos\varphi$$

For thermal velocities $v \simeq 1$ mm/s, typical values for $\Delta\theta$ are around $2 \cdot 10^{-5}$ rad.

Thus, according to Young's equation, we calculate the force per unit length f acting on the contact line (fig. A.3b,c):

$$f(\varphi) = \sigma_{LV} \left[\cos\left(\theta + \Delta\theta\right) - \cos\theta\right] \simeq \sigma_{LV} \Delta\theta$$

since $\theta = 90°$ and $\Delta\theta \ll 1$. Using the expression for $\Delta\theta$ we write:

$$f(\varphi, \alpha) = \sigma_{LV} \left(\frac{3}{2}\frac{\eta v}{\sigma_{LV}} - 2\alpha\right) \cos\varphi$$

Since $v_L = f/\zeta_0$ and taking into account the expression of v_L as a function of α, we recover the evolution in time of the position of the contact line:

$$\frac{3}{4}\frac{\eta v}{\sigma_{LV}} \left(1 - \exp(-t/\tau)\right)$$

where $\tau = R\zeta_0/2\sigma_{LV}$ denotes the characteristic time for the motion of the line. The dissipation per unit length of the contact line at a given time t is

$$dP = v_L(\alpha) f(\alpha) d\ell$$

We need to average in time over a period τ_p and to integrate along the contact line perimeter to find the total dissipation. The average dissipation per unit line is then:

$$\langle P_{line} \rangle = \frac{1}{\tau_p} \int_0^{\tau_p} dP = \frac{1}{\tau_p} \int_{\alpha(0)}^{\alpha(\tau_p)} v_L f \frac{R}{v_L} d\alpha$$

i.e.,

$$\langle P_{line} \rangle = \frac{9}{16} \frac{\eta^2 R v^2}{\tau_p \sigma_{LV}} \left(1 - \exp(-2\tau_p/\tau)\right) \cos^2\varphi$$

Finally, the total dissipation is

$$\langle P_{tot} \rangle = R \int_0^{2\pi} \langle P_{line} \rangle d\varphi = \frac{9}{16} \pi \frac{\eta^2 R^2 v^2}{\tau_p \sigma_{LV}} \left(1 - \exp(-2\tau_p/\tau)\right)$$

In the considered case, a bead with radius $R \sim 1\mu$m is moving at the air–water interface ($\sigma_{LV} = 0.072$ N/m, $\eta = 1.001 \cdot 10^{-3}$ Pa·s). In the ballistic regime, we have a thermal velocity $v \sim 1$mm/s with a characteristic time $\tau_p = 0.1\mu$s. In these conditions the dissipation is at least 50 times lower than the one that it is needed to explain the observed dynamics. The role of solid dissipation induced by the rotation of the beads is not sufficient to explain the measured drag coefficient. Such a dissipation is much smaller (at least 50 times smaller) than the hydrodynamic contribution usually considered. The variation of the pressure field induced by the motion of the bead is thus not able to significantly modify the particle dynamics.

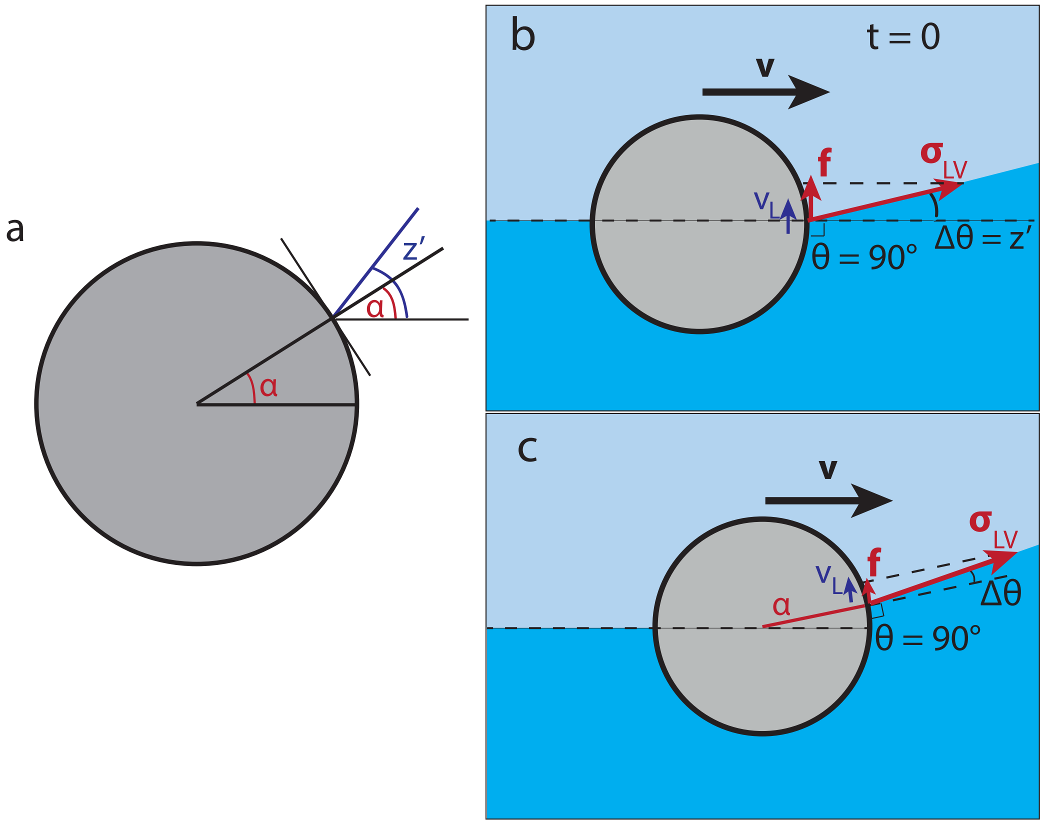

Figure A.3: **a.** Angular position α of the contact on the particle surface. The equilibrium position corresponds to the value $\alpha = 0$. The slope of the interface at the contact line is provided by z', i.e. the derivative of the interface profile. The difference between the two angles, $\arctan z' - \alpha$ corresponds to the variation $\Delta\theta$ of contact angle. **b.** Schematic picture (not in scale) of the deformation of the interface profile, induce by the pressure field of the particle moving at velocity $\mathbf{v}$, at the initial time $t = 0$. The contact line lays on its equilibrium position $\alpha = 0$ and the variation of the contact angle is $\Delta\theta = \arctan z'$. The interfacial force (per unit length) σ_{LV} has a component f parallel to the particle surface. Such a force makes the contact line move at a velocity v_L. **c.** At a generic time, the contact line is in a new angular position α, due to the action of the line force f. The slope of the interface is reduced, but the force f is still present and pushes the contact line.

A.3.2: Contact line friction coupled with particle rotation

A linear motion of a bead in a viscous fluid induces also a variation of the stress field around the bead itself. Landau [16] found the components of the stress tensor at the surface of the particle as a solution of Navier-Stokes equation:

$$\sigma'_{rr} = 0, \qquad \sigma'_{r\vartheta} = -\frac{3\eta}{2R} v \sin\vartheta$$

where v is the velocity of the particle and the coordinates are shown in fig.

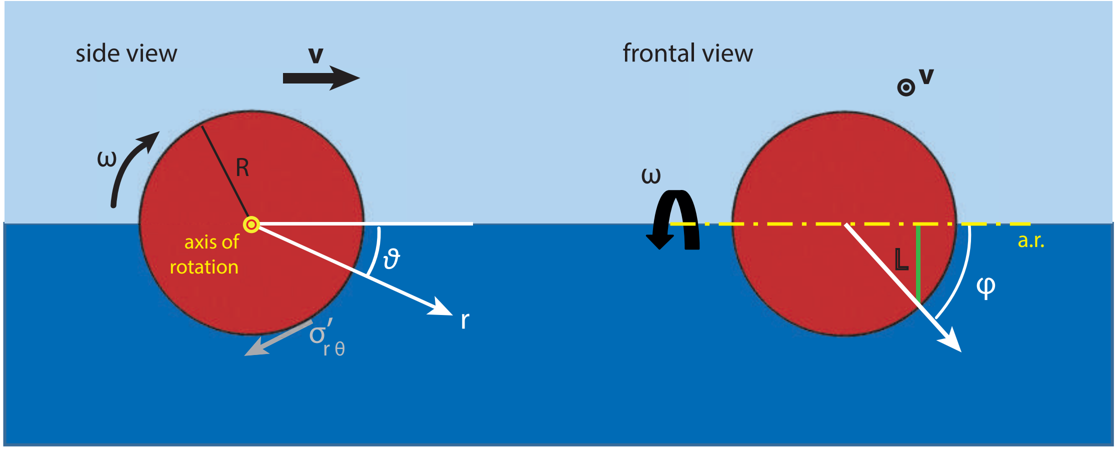

Figure A.4: Spherical coordinates system (r, ϑ, φ) for a particle of radius R at the air-water interface. For the sake of simplicity, we consider a contact angle $\theta = 90°$. The bead is moving at a velocity v on the interfacial plane: such a motion induces a stress $\sigma'_{r\vartheta}$ on the particle surface, according to [16]. The result is the rotation of the sphere around an horizontal axis (yellow dashed line in frontal view) at an angular velocity ω. $L = R\sin\varphi$ gives the distance between a generic point on the particle surface and the axis of rotation.

A.4.

The action of the stress $\sigma'_{r\vartheta}$ on the particle surface results in the rotation around an horizontal axis (fig. A.4). If we consider an infinitesimal element dA of the particle surface, the corresponding torque is

$$d\Gamma = \sigma'_{r\vartheta} L dA$$

where $L = R\sin\varphi$ is the distance between dA and the axis of rotation (fig. A.4).

Since $dA = R^2 \sin\vartheta d\vartheta d\varphi$, the total torque exerted on the lower hemisphere (the part of the bead that is immersed in water) is obtained by integration of $d\Gamma$:

$$\Gamma = \int_{hemisph} \sigma'_{r\vartheta} L dA = \int_0^\pi \int_0^\pi -\frac{3\eta}{2R} v \sin\vartheta R \sin\varphi R^2 \sin\vartheta d\vartheta d\varphi$$

$$= -\frac{3}{2}\eta R^2 v \int_0^\pi \sin^2\vartheta d\vartheta \int_0^\pi \sin\varphi d\varphi = -\frac{3}{2}\pi\eta R^2 v$$

Hence, the final expression for the torque Γ exerted by the fluid on the moving bead is

$$\Gamma = -\frac{3}{2}\pi\eta R^2 v$$

The viscous drag of the water makes the bead rotate as a sort of wheel, leading to a steady angular velocity ω, recovered by the condition:

$$\frac{3}{2}\pi\eta R^2 v = 4\pi\eta R^3 \omega$$

i.e. the equilibrium between the viscous drag of the water and the torque due to the motion of the particle. The right hand side of the equation is a rough approximation for the viscous drag: the term $4\pi\eta R^3$ is the half of the rotational drag coefficient for a sphere, since $\theta = 90°$.

The resulting angular velocity ω (fig. A.4) around an horizontal axis is:

$$\omega = \frac{3}{8}\frac{v}{R}$$

Now, we assume that the interface remains flat. The contact line lays at its equilibrium position and slides on the rotating particle. The relative velocity v_L between the triple line and the solid substrate is so written as:

$$v_L = R\omega\cos\varphi = \frac{3}{8}v\cos\varphi$$

related to a dissipation power of

$$P = \oint \frac{1}{2}\zeta_0 v_L^2 d\ell$$

where ζ_0 is the friction coefficient per unit length introduced in Blake's theory [23, 52].

Using the expression for v_L, it finally results in

$$P = \frac{1}{2}\pi R\frac{k_B T}{\kappa_0\lambda^3}\frac{9}{64}v^2$$

For a micrometric bead ($R \sim 1\mu$m) moving at a thermal velocity ($v \sim 1$mm/s), with λ in a nanometric range, the dissipation is too small (at least 50 times) compared to the one that it is needed to explain the observed dynamics. The role of solid dissipation induced by the rotation of the beads is not sufficient to explain the measured drag coefficient.

Bibliography

[1] A. Einstein. Über die von der molekularkinetischen theorie der wrme geforderte bewegung von in ruhenden flssigkeiten suspendierten teilchen. *Annalen der Physik*, 322(8):549–560, 1905.

[2] J. Perrin. Mouvement brownien et réalité moléculaire. *Annales de Chimie et de Physique*, 18:5–104, 1909.

[3] Y. Han, A.M. Alsayed, M. Nobili, J. Zhang, T.C. Lubensky, and A.G. Yodh. Brownian motion of an ellipsoid. *Science*, 314(5799):626–630, 2006.

[4] Y. Han, A. Alsayed, M. Nobili, and A.G. Yodh. Quasi-two-dimensional diffusion of single ellipsoids: Aspect ratio and confinement effects. *Physical Review E*, 80(1):011403, 2009.

[5] D. Mukhija and M.J. Solomon. Translational and rotational dynamics of colloidal rods by direct visualization with confocal microscopy. *J. Colloid Interface Sci.*, 314(1):98–106, 2007.

[6] T. Li, S. Kheifets, D. Medellin, and M.G. Raizen. Measurement of the instantaneous velocity of a brownian particle. *Science*, 328(5986):1673–1675, 2010.

[7] R. Huang et al. Direct observation of the full transition from ballistic to diffusive brownian motion in a liquid. *Nature Physics*, 7(7):576–580, 2011.

[8] D. Wang et al. Probing diffusion of single nanoparticles at water–oil interfaces. *Small*, 7(24):3502–3507, 2011.

[9] N.N. Poddar and J.G. Amar. Adsorption and diffusion of colloidal au nanoparticles at a liquid-vapor interface. *The Journal of Chemical Physics*, 140(24), 2014.

[10] H. Zheng, S.A. Claridge, A.M. Minor, A.P. Alivisatos, and U. Dahmen. Nanocrystal diffusion in a liquid thin film observed by in situ transmission electron microscopy. *Nano Letters*, 9(6):2460–2465, 2009.

[11] K. Du, J.A. Liddle, and A.J. Berglund. Three-dimensional real-time tracking of nanoparticles at an oilwater interface. *Langmuir*, 28(25):9181–9188, 2012.

[12] K. Stratford, R. Adhikari, I. Pagonabarraga, J.C. Desplat, and M.E. Cates. Colloidal jamming at interfaces: a route to fluid-bicontinuous gels. *Science*, 309(5744):2198–2201, 2005.

[13] M. Gibiansky et al. Bacteria use type iv pili to walk upright and detach from surfaces. *Science*, 330(6001):197–197, 2010.

[14] B.N. Kholodenko. Cell-signalling dynamics in time and space. *Nat. Rev. Mol. Cell. Bio.*, 7(3):165–176, 2006.

[15] D.M. Kaz, R. McGorty, M. Mani, M.P. Brenner, and V.N. Manoharan. Physical ageing of the contact line on colloidal particles at liquid interfaces. *Nature materials*, 11(2):138–142, 2012.

[16] L.D. Landau and E.M. Lifshitz. *Fluid Mechanics: Landau and Lifshitz: Course of Theoretical Physics*, volume 6. Elsevier, 2013.

[17] P. Pieranski. Two-dimensional interfacial colloidal crystals. *Phys. Rev. Lett.*, 45:569–572, 1980.

[18] T. Young. An essay on the cohesion of fluids. *Philosophical Transactions of the Royal Society of London*, pages 65–87, 1805.

[19] A.B.D. Cassie and S. Baxter. Wettability of porous surfaces. *Trans. Faraday Soc.*, 40(2):546–551, 1944.

[20] P.G. De Gennes. Wetting: statics and dynamics. *Reviews of modern physics*, 57(3):827, 1985.

[21] D. Bonn, J. Eggers, J. Indekeu, J. Meunier, and E. Rolley. Wetting and spreading. *Reviews of modern physics*, 81(2):739, 2009.

[22] M. Chaplin. Theory vs experiment: what is the surface charge of water. *Water*, 1:1–28, 2009.

[23] T.D. Blake and J.M. Haynes. Kinetics of liquid-liquid displacement. *J. Colloid Interface Sci.*, 30(3):421–423, 1969.

[24] P.G. de Gennes. Wetting: statics and dynamics. *Rev. Mod. Phys.*, 57:827–863, 1985.

[25] H.B. Eral, D.J.C.M. 't Mannetje, and J.M. Oh. Contact angle hysteresis: a review of fundamentals and applications. *Colloid and Polymer Science*, 291(2):247–260, 2013.

[26] C.W. Extrand and Y. Kumagai. An experimental study of contact angle hysteresis. *J. Colloid Interface Sci.*, 191(2):378–383, 1997.

[27] K.D. Danov, R. Aust, F. Durst, and U. Lange. Influence of the surface viscosity on the hydrodynamic resistance and surface diffusivity of a large brownian particle. *J. Colloid Interface Sci.*, 175(1):36–45, 1995.

[28] C. Pozrikidis. Particle motion near and inside an interface. *J. Fluid Mech.*, 575(1):333–357, 2007.

[29] Th.M. Fischer, P. Dhar, and P. Heinig. The viscous drag of spheres and filaments moving in membranes or monolayers. *J. Fluid. Mech.*, 558(1):451–475, 2006.

[30] J.T. Petkov et al. Measurement of the drag coefficient of spherical particles attached to fluid interfaces. *J. Colloid Interface Sci.*, 172(1):147–154, 1995.

[31] B. Radoev, M. Nedyalkov, and V. Dyakovich. Brownian motion at liquid-gas interfaces. 1. diffusion coefficients of macroparticles at pure interfaces. *Langmuir*, 8(12):2962–2965, 1992.

[32] M. Sickert and F. Rondelez. Shear viscosity of langmuir monolayers in the low-density limit. *Physical review letters*, 90(12):126104, 2003.

[33] M. Sickert, F. Rondelez, and H.A. Stone. Single-particle brownian dynamics for characterizing the rheology of fluid langmuir monolayers. *EPL (Europhysics Letters)*, 79(6):66005, 2007.

[34] W. Chen and P. Tong. Short-time self-diffusion of weakly charged silica spheres at aqueous interfaces. *EPL (Europhysics Letters)*, 84(2):28003, 2008.

[35] Y. Peng, W. Chen, Th.M. Fischer, D.A. Weitz, and P. Tong. Short-time self-diffusion of nearly hard spheres at an oil–water interface. *J. Fluid Mech.*, 618:243–261, 2009.

[36] F. Perrin. Mouvement brownien d'un ellipsoide (i). dispersion diélectrique pour des molécules ellipsoidales. *J. Phys. Radium*, 5(10):497–511, 1934.

[37] F. Perrin. Mouvement brownien d'un ellipsoide (ii). rotation libre et dépolarisation des fluorescences. translation et diffusion de molécules ellipsoidales. *J. Phys. Radium*, 7(1):1–11, 1936.

[38] J. Happel, H. Brenner, and R.J. Moreau. Low reynolds number hydrodynamics: with special applications to particulate media (mechanics of fluids and transport processes). *Kluwer Academic Publishers Group, Distribution Center, PO Box*, 322:3300, 1983.

[39] S.H. Koenig. Brownian motion of an ellipsoid. a correction to perrin's results. *Biopolymers*, 14(11):2421–2423, 1975.

[40] J.C. Loudet, A.G. Yodh, and B. Pouligny. Wetting and contact lines of micrometer-sized ellipsoids. *Phys. Rev. Lett.*, 97(1):018304, 2006.

[41] J.C. Loudet and B. Pouligny. How do mosquito eggs self-assemble on the water surface? *The European Physical Journal E: Soft Matter and Biological Physics*, 34(8):1–17, 2011.

[42] J.C. Loudet, A.M. Alsayed, J. Zhang, and A.G. Yodh. Capillary interactions between anisotropic colloidal particles. *Phys. Rev. Lett.*, 94:018301, 2005.

[43] M. Cavallaro, L. Botto, E.P. Lewandowski, M. Wang, and K.J. Stebe. Curvature-driven capillary migration and assembly of rod-like particles. *Proc. Nat. Acad. Sci.*, 108(52):20923–20928, 2011.

[44] V.N. Paunov. Novel method for determining the three-phase contact angle of colloid particles adsorbed at airwater and oilwater interfaces. *Langmuir*, 19(19):7970–7976, 2003.

[45] C. Blanc et al. Capillary force on a micrometric sphere trapped at a fluid interface exhibiting arbitrary curvature gradients. *Phys. Rev. Lett.*, 111(5):058302, 2013.

[46] J.C. Crocker and D.G. Grier. Methods of digital video microscopy for colloidal studies. *J. Colloid Interface Sci.*, 179(1):298–310, 1996.

[47] C.C. Ho, A. Keller, J.A. Odell, and R.H. Ottewill. Preparation of monodisperse ellipsoidal polystyrene particles. *Colloid and Polymer Science*, 271(5):469–479, 1993.

[48] H. Lehle, E. Noruzifar, and M. Oettel. Ellipsoidal particles at fluid interfaces. *Eur. Phys. J. E*, 26(1-2):151–160, 2008.

[49] E.B. Dussan V. and S.H. Davis. On the motion of a fluid-fluid interface along a solid surface. *Journal of Fluid Mechanics*, 65(01):71–95, 1974.

[50] P. Langevin. Sur la théorie du mouvement brownien. *CR Acad. Sci. Paris*, 146(530-533), 1908.

[51] L.D. Landau and E.M. Lifshitz. Cours de physique théorique: Physique statistique (mir, 1967) ch. 5; kubo r. *Rep. Progr. Phys*, 29:255, 1966.

[52] T.D. Blake. The physics of moving wetting lines. *J. Colloid Interface Sci.*, 299(1):1–13, 2006.

[53] S. Glasstone, K.J. Laidler, and H. Eyring. *The theory of rate processes: the kinetics of chemical reactions, viscosity, diffusion and electrochemical phenomena.* McGraw-Hill Book Company, Incorporated, 1941.

[54] J.C. Berg. *Wettability.* CRC Press, 1 edition, 1993.

[55] R.E. Powell, W.E. Roseveare, and H. Eyring. Diffusion, thermal conductivity, and viscous flow of liquids. *Industrial & Engineering Chemistry*, 33(4):430–435, 1941.

[56] S. Arrhenius. Über die reaktionsgeschwindigkeit bei der inversion von rohrzucker durch säuren. *Zeitschrift für physikalische Chemie*, 4:226–248, 1889.

[57] T.D. Blake and J. De Coninck. The influence of solid-liquid interactions on dynamic wetting. *Adv. Colloid Interface Sci.*, 96(1):21–36, 2002.

[58] A.P. Philipse. *Notes on Brownian motion.* 2011.

[59] R.K. Iler. *The chemistry of silica: solubility, polymerization, colloid and surface properties, and biochemistry.* Wiley, 1979.

[60] J.G. Petrov, J. Ralston, and R.A. Hayes. Dewetting dynamics on heterogeneous surfaces. a molecular-kinetic treatment. *Langmuir*, 15(9):3365–3373, 1999.

[61] S.A. Kulkarni, S.B. Ogale, and K.P. Vijayamohanan. Tuning the hydrophobic properties of silica particles by surface silanization using mixed self-assembled monolayers. *J. Colloid Interface Sci.*, 318(2):372–379, 2008.

[62] M.V. Smoluchowski. Molekular-kinetische theorie der opaleszenz von gasen im kritischen zustande, sowie einiger verwandter erscheinungen. *Annalen der Physik*, 330:205–226, 1908.

[63] K. Mecke and S. Dietrich. Local orientations of fluctuating fluid interfaces. *J. Chem. Phys.*, 123(20):204723, 2005.

[64] L. Mandelstam. Über die rauhigkeit freier flüssigkeitsoberflächen. *Annalen der Physik*, 346(8):609–624, 1913.

[65] D.G.A.L. Aarts, M. Schmidt, and H.N.W. Lekkerkerker. Direct visual observation of thermal capillary waves. *Science*, 304(5672):847–850, 2004.

[66] M. Gross and F. Varnik. Interfacial roughening in non–ideal fluids: Dynamic scaling in the weak-and strong-damping regime. *Phys. Rev. E*, 87(2):022407, 2013.

[67] M. Grant and R.C. Desai. Fluctuating hydrodynamics and capillary waves. *Phys. Rev. A*, 27:2577–2584, 1983.

[68] E.G. Flekkøy and D.H. Rothman. Fluctuating hydrodynamic interfaces: Theory and simulation. *Phys. Rev. E*, 53:1622–1643, 1996.

[69] M.E. ONeill, K.B. Ranger, and H. Brenner. Slip at the surface of a translating–rotating sphere bisected by a free surface bounding a semi-infinite viscous fluid: Removal of the contact-line singularity. *Physics of Fluids (1958-1988)*, 29(4):913–924, 1986.

[70] M.S. Faltas and E.I. Saad. Three-dimensional stokes flow caused by a translating–rotating sphere bisected by a free surface bounding a semi-infinite micropolar fluid. *Mathematical Methods in the Applied Sciences*, 31(10):1233–1256, 2008.

[71] G. Boniello et al. Brownian diffusion of a partially wetted colloid. *Submitted*, 2014.

[72] S. Ramanujan. Ramanujans collected works. *Chelsea, New York*, 52, 1962.

[73] G.G. Stokes. *On the effect of the internal friction of fluids on the motion of pendulums*, volume 9. Pitt Press, 1851.